

# Integration of the CBM MVD Pre-Series Module

Masterarbeit  
zur Erlangung des akademischen Grades eines  
**Master of Science**

vorgelegt beim Fachbereich Physik  
der Johann Wolfgang Goethe-Universität  
in Frankfurt am Main

von  
**Franz Alexej Matejcek**  
aus Großkarlbach

Frankfurt 2024

Erstgutachter: Prof. Dr. Joachim Stroth  
Zweitgutachter: Dr. Christian Müntz



# Abstract

The Compressed Baryonic Matter Experiment (CBM) will operate at the future SIS 100 accelerator to study the properties of strongly interacting matter in the region of moderate temperature and high baryochemical potential. It is a fixed target experiment currently under construction at the Facility for Antiproton and Ion Research (FAIR) in Darmstadt, Germany.

The Micro Vertex Detector (MVD) is the first downstream detector. It extends the acceptance to low momenta and enables high-precision tracking in direct proximity of the target. Its four planar detector stations will operate between 8 and 20 cm downstream of the target in the moderate vacuum of the target chamber ( $p \sim 10^{-4}$  mbar) which is placed in the center of the CBM dipole magnet (field integral  $\sim 1$  Tm). The harsh radiation environment of up to  $7 \cdot 10^{13}$   $n_{eq}/\text{cm}^2$  and 5 Mrad per CBM running year poses challenging constraints on the whole MVD and in particular on the dedicated CMOS MAPS (MIMOSIS). The sensor technology requests stable sub-0 °C operation during runtime to maintain high detection efficiency and low fake rate. Each detector plane will feature a material budget  $x/x_0$  ranging between 0.3 and 0.5%.

The baseline integration concept has been documented in the MVD Technical Design Report (TDR, [1]). To reach the material budget limits, it relies on conductive cooling inside, and active cooling outside the geometric acceptance. The large-area ( $31.15 \times 17.25 \text{ mm}^2$ ) thinned ( $50 \mu\text{m}$ ) sensors will be glued onto planar carriers of Thermal Pyrolytic Graphite (TPG,  $380 \mu\text{m}$  thick) that provide mechanical stiffness and a high thermal conductivity in the geometrical acceptance. The sensor will then be wire-bonded to dedicated FPCs connecting the front-end electronics which will be mounted on an actively cooled aluminum heat sink (Novec 649 as coolant) sitting outside the acceptance. Up to 28 sensors per module have to be glued and bonded on both sides of the carrier to achieve a 100% fill factor inside the acceptance.

The thesis summarizes the efforts in the optimization of the preparation of components and their handling, developed QA procedures, and integration techniques in preparation of a pre-series module for one of the largest station. This results in the development of a integration flow for MVD half-stations which has been optimized for a fine-meshed QA, producibility, reworkability, and flexibility in pre-conditioning the detector to allow for a high-yield integration. The yield of the mechanical integration of sensors in modules is challenged by the large number of sensors that have to be integrated vacuum-compatibly on a soft carrier with sizeable surface roughness.

Needle probe testing as QA for the MIMOSIS sensors is in preparation for mass-testing at a manual prober bench. The adhesive selection, the form factors of the carriers, and the integration technique have been further improved from the TDR. The engineering design of the heat sinks has been finalized. Parylene-C coating of the carriers, together with a consecutive plasma activation to improve the gluability on the hydrophobic coating, has been identified and tested as a way to reduce the abrasion and the surface electrical conductivity of TPG. An industrial laser depaneling device has been identified as the proper tool for precision cutting and surface ablation ('hatching') of TPG. An improved integration technique based on dedicated hatches in the carrier has been developed, allowing for a low-risk and reliable assembly technique with consistent sensor-to-sensor distance of the thinned sensors with very high precision and excellent alignment of front- and back-side by laser-cut fiducial marks. The feasibility of this technique has been validated by the mechanical integration of a demonstrator for a double-sided, vacuum-compatible  $\mu$ -tracker with minimal material budget inside the acceptance. Laser hatching has been identified as a reworking technique for single sensors on modules to significantly improve the integration yield.

A pre-series module of the MVD can be mechanically integrated based on the achievements of this thesis to demonstrate the yield and efficiency of the QA measures and integration techniques.



# Contents

<b>Acronyms and Abbreviations</b>	<b>V</b>
<b>1 Introduction</b>	<b>1</b>
1.1 Introduction to CBM . . . . .	1
1.2 Introduction to the MVD . . . . .	2
1.2.1 Physics Motivation . . . . .	2
1.2.2 Running Environment . . . . .	4
1.2.3 Technical Design of the MVD . . . . .	4
1.2.4 Introduction to this Thesis . . . . .	5
<b>2 Sensor Integration</b>	<b>7</b>
2.1 The Sensors . . . . .	7
2.1.1 Proposed QA Procedure . . . . .	11
2.1.2 Open Questions . . . . .	12
2.2 The Carriers . . . . .	14
2.2.1 Proposed QA Procedure . . . . .	15
2.2.2 Open Questions . . . . .	15
2.3 The Adhesives . . . . .	16
2.3.1 Proposed QA Procedure . . . . .	21
2.3.2 Open Questions . . . . .	21
2.4 The Flexible Printed Circuits . . . . .	22
2.4.1 Proposed QA Procedure . . . . .	25
2.4.2 Open Questions . . . . .	25
2.5 The Front-End Electronics . . . . .	26
2.6 The Heat Sinks . . . . .	27
2.6.1 Proposed QA Procedure . . . . .	29
<b>3 Detector Integration</b>	<b>30</b>
3.1 The Top Plates . . . . .	30
3.1.1 Proposed QA Procedure . . . . .	31
3.1.2 Open Questions . . . . .	31
3.2 The Coolant Manifolds . . . . .	32
3.2.1 Proposed QA Procedure . . . . .	33
3.2.2 Open Questions . . . . .	33
3.3 Detector Mounting . . . . .	34
3.3.1 Proposed QA Procedure . . . . .	36
3.3.2 Open Questions . . . . .	36
3.4 Detector Control System . . . . .	36
3.5 The MVD Cooling System . . . . .	37
3.5.1 Design Considerations . . . . .	37
3.5.2 Choice of Coolant . . . . .	37
3.5.3 Recommendation . . . . .	39

<b>4</b>	<b>Selected Integration Techniques</b>	<b>42</b>
4.1	TPG Laser Processing . . . . .	42
4.1.1	Cutting . . . . .	42
4.1.2	Hatching . . . . .	44
4.1.3	Outlook: $\mu$ -Tracker With Minimum Material Budget . . . . .	47
4.2	Reworking Strategies . . . . .	50
4.3	Sensor Integration Flow . . . . .	53
4.3.1	Open Questions . . . . .	57
4.4	Detector Integration Flow . . . . .	57
<b>5</b>	<b>Summary and Outlook</b>	<b>60</b>
5.1	Sensor Integration . . . . .	60
5.2	Detector Integration . . . . .	61
5.3	Selected Integration Techniques . . . . .	61
5.4	Outlook . . . . .	62
<b>A</b>	<b>Appendix</b>	<b>63</b>
A.1	Ionizing Radiation Doses of the MVD . . . . .	63
A.2	The Updated MVD CAD Model . . . . .	64
A.2.1	MVD Geometric Acceptance . . . . .	65
A.3	Integration Support Jig . . . . .	65
A.4	Optimization of the Gluing Pattern of the Sensors . . . . .	66
A.5	Thermal Simulations of the Proposed $\mu$ -Tracker Design . . . . .	71
A.6	Radiolysis Effects on the Coolant . . . . .	73
	<b>Bibliography</b>	<b>81</b>

# Acronyms and Abbreviations

<b>ADC</b>	Analog to Digital Converter
<b>ASIC</b>	Application-Specific Integrated Circuit
<b>CAD</b>	Computer Aided Design
<b>CBM</b>	Compressed Baryonic Matter Experiment
<b>CIS</b>	CMOS Image Sensors
<b>CMOS</b>	Complementary Metal - Oxide - Semiconductor
<b>CNC</b>	Computerized Numerical Control
<b>CTE</b>	Coefficient of Thermal Expansion
<b>CVD</b>	Chemical Vapour Deposition
<b>DAC</b>	Digital to Analog Converter
<b>DAQ</b>	Data Acquisition
<b>DCS</b>	Detector Control System
<b>DL</b>	GSI Detector Laboratory
<b>EOL</b>	End - of - Lifetime
<b>EPICS</b>	Experimental Physics and Industrial Control System
<b>ESD</b>	Electrostatic Discharge
<b>FAIR</b>	Facility for Antiproton and Ion Research
<b>FEA</b>	Finite Element Analysis
<b>FEAST</b>	Radiation Tolerant DC/DC Converter
<b>FEB</b>	Front-End Board
<b>FPC</b>	Flexible Printed Circuit
<b>GBTx</b>	Gigabit Transceiver ASIC
<b>GEANT</b>	Geometry and Tracking
<b>GSI</b>	GSI Helmholtzzentrum für Schwerionenforschung
<b>GWP</b>	Global Warming Potential
<b>HADES</b>	High Acceptance Di-Electron Spectrometer

**IKF** Institut für Kernphysik Frankfurt

**LET** Linear Energy Transfer

**MAPS** Monolithic Active Pixel Sensor

**MIMOSA** Minimum Ionizing Particle MOS Active Pixel Sensor

**MIMOSIS** The CMOS Pixel Sensor Developed for the CBM Micro Vertex Detector Installed at Schwer - Ionen - Synchrotron (SIS)

**MVD** Micro Vertex Detector

**NPT** National Pipe Taper

**PCB** Printed Circuit Board

**PFAS** Per- and Polyfluoroalkyl Substance

**PGS** Pyrolytic Graphite Sheet

**PRESTO** Precursor of the Second Station of the CBM - MVD

**QA** Quality Assessment / Assurance

**ROB** Readout Board

**SCA** Slow Control Adapter

**SEE** Single Event Effect

**SIS** Schwerionensynchrotron

**SMD** Surface-mounted Device

**STS** Silicon Tracking System

**TDR** Technical Design Report

**TPG** Thermal Pyrolytic Graphite

**TR** Tracking Geometry

**TRB** TDC Readout Board

**VX** Vertexing Geometry

**ZIF** Zero Insertion Force

# 1 Introduction

## 1.1 Introduction to CBM

The Compressed Baryonic Matter Experiment (CBM) is a fixed target experiment currently under construction at the Facility for Antiproton and Ion Research (FAIR, see figure 1.1) in Darmstadt, Germany. The goal is to study the properties of strongly interacting matter in the region of moderate temperature and high baryochemical potential. For this, CBM will perform high-precision integral and multi-differential measurements with unprecedented statistics of almost all emitted particles at collision energies of  $\sqrt{s} = 2.7 - 4.9 A \text{ GeV}$  and interaction rates of up to  $10^7 \text{ Hz}$ . The SIS 100 accelerator of FAIR will provide CBM with protons (up to 29 GeV) and heavy ions (nuclei with  $Z/A = 0.5$  up to  $14 A \text{ GeV}$ , Au ions up to  $11 A \text{ GeV}$ ) at high beam intensities (up to  $10^9$  Au ions per second) [1].

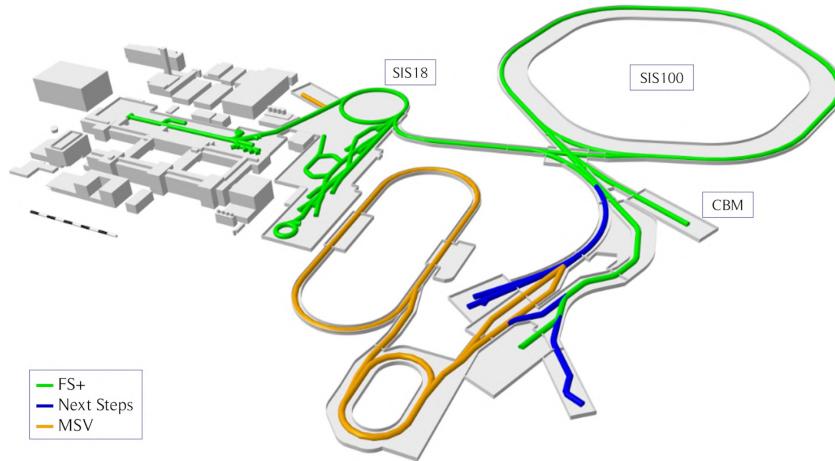


Figure 1.1: Layout of FAIR with the two ring accelerators SIS 18 and SIS 100, and CBM indicated. The sub-objectives of the staged completion are color-coded [2].

The physics program of CBM focuses on the fundamental properties of strongly interacting matter:

- The phase structure at large baryochemical potential, including possible phase transitions to quarkyonic or partonic matter.
- The restoration of chiral symmetry in dense baryonic matter.
- The equation of state of baryonic matter at neutron star core densities.
- The production mechanisms and properties of single- and double-strange hypernuclei.
- The production mechanisms and in-medium properties of charmed particles in dense baryonic matter.

A detailed discussion of the CBM physics goals, experimental observables, and the projected physics performance is far beyond the scope of this thesis. Instead, the interested reader is here referred to the wide variety of literature, *e. g.* the CBM Physics Book [3].

CBM is a multi-purpose detector employing several detector sub-systems that provide high-precision tracking and particle identification with self-triggered readout electronics in a free-streaming data acquisition (DAQ). A recent CAD view of the detector setup is shown in figure 1.2. The high-speed data processing and online event selection will happen on-site at the GSI Green IT Cube. All sub-systems are on the verge of the pre- or even series production and the global commissioning of the experiment with beam is supposed to be completed by 2028 [4].

In preparation of CBM at SIS 100, the so-called mini CBM (mCBM) setup is operating pre-series and prototype detector modules at high intensity beams from SIS 18. It is designed to test and optimize the performance of the detector sub-systems, the free-streaming DAQ, and the online data analysis and event selection under realistic experiment conditions. The mMVD, the contribution of the MVD team to mCBM, is currently in preparation to be implemented by March 2025 for a benchmark run with Ag beam.

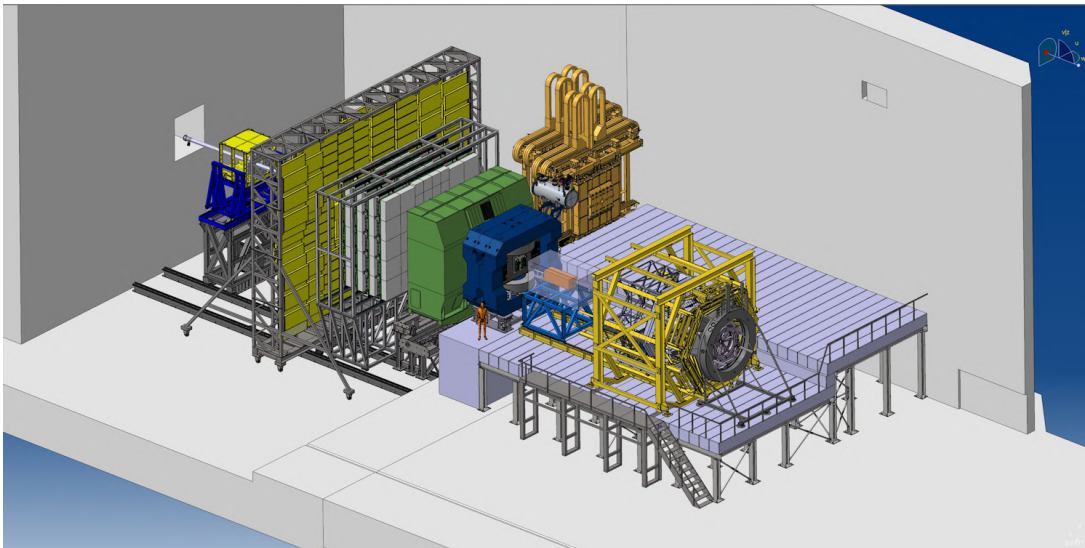


Figure 1.2: CAD view of the projected day one experimental setup of the CBM detector in the so-called electron setup for SIS 100, including also the HADES detector upstream [5].

## 1.2 Introduction to the MVD

### 1.2.1 Physics Motivation

This thesis focuses on the first detector sub-system downstream of the target, the Micro Vertex Detector (MVD). It will serve as a high-precision tracking device in closest proximity to the target. This will allow for low-momentum tracking down to about  $300 \text{ MeV}/c$ , primary and secondary vertexing with a precision of below  $70 \mu\text{m}$  along the beam axis, background suppression in dielectron spectroscopy, and, together with the main tracker of CBM, the Silicon Tracking System (STS), the identification of hyperons by decay topology [1].

A detailed discussion of the use case of the MVD and the projected physics performance is beyond the scope of this thesis. The technical design which is discussed in chapter 1.2.3 is motivated here only exemplarily, demonstrating the necessity of low-mass tracking stations additionally to the STS in closest proximity to the target and motivating the harsh material budget requirements.

The direct experimental observables are the yields and kinematic properties of the particles produced in the nuclear reactions. At SIS 100 energies, many bulk particles are emitted at low momenta below  $\sim 1 \text{ GeV}/c$ . A high low-momentum tracking efficiency is hence important. Figure 1.3 shows the improvement of the low-momentum track reconstruction efficiency (exemplarily

for  $\pi^+$ ) by the MVD when supplementing the STS. The necessity of an additional tracking device sandwiched between the target and the STS has also been demonstrated in simulations of the reconstruction of dielectrons produced in the decay of vector mesons inside the fireball. With the MVD, the combinatorial background of dielectrons produced in  $\gamma$ -conversions and  $\pi^0$ -decays can be significantly reduced, allowing access to these rare probes [6].

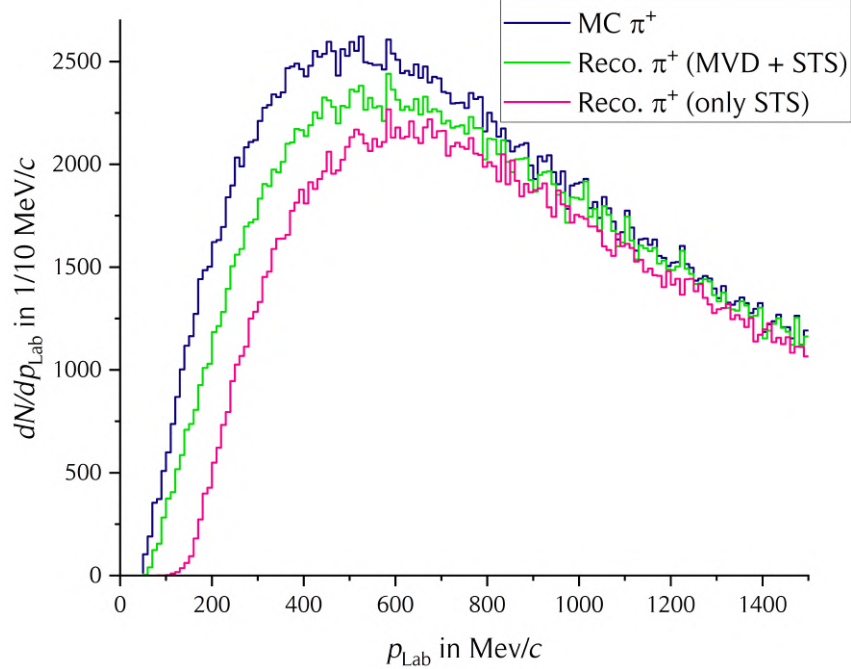


Figure 1.3: Total number of reconstructable Monte Carlo  $\pi^+$  produced in 10 000 central Au+Au collisions at 4.9 A GeV (minimum 3 hits in the CBM silicon layers), reconstructable  $\pi^+$  using the MVD and STS, and reconstructable  $\pi^+$  using only the STS, as a function of the laboratory momentum [7].

The MVD is a highly granular detector in close proximity to the primary vertex, enhancing the low-momentum track reconstruction efficiency of CBM. The overall pointing precision of the detector is given by the finite resolution due to the geometry of the detector and multiple scattering in the tracking stations. The geometric contribution is determined by the spatial distribution of the tracking stations and their intrinsic spatial resolution which is directly proportional to the pixel pitch<sup>1</sup>. Multiple scattering is mainly determined by a  $1/p_{\text{Lab}}$ -dependence on the momentum of the tracked particle in the laboratory frame and a  $\sqrt{x/X_0}$ -dependence on the material budget. Indeed, multiple scattering is a large contribution to the pointing precision at SIS 100 energies due to the small laboratory momenta [8]. The influence of multiple scattering can be mitigated by minimizing the material budget inside the acceptance. For CBM, this means moving the vacuum window of the target chamber downstream of the MVD and designing a low-material budget vacuum-compatible tracker.

The only comparable vacuum-compatible tracking device currently operating, the LHCb VELO, relies on active cooling inside the acceptance using Si microchannels. The average momenta of the particles in LHCb are, however, large compared to CBM, alleviating the constraints of the material budget  $x/X_0$  to  $\mathcal{O}(1\%)$  per station [9]. The small average laboratory momenta of CBM call for a cutting-edge material budget for vacuum-compatible Si pixel detectors to achieve a high low-momentum track reconstruction efficiency. Also, the MVD has to cover a significantly larger geometric acceptance than the LHCb VELO. These are the driving forces for the technical design of the detector. The harsh requirements on the material budget  $x/X_0$  of the MVD of  $\mathcal{O}(0.3\%)$  per

<sup>1</sup>The spatial resolution for fully depleted sensors is  $\text{pitch}/\sqrt{12}$ .

station can only be reached by moving the active cooling to the periphery, and the use of thermal and mechanical high-performance materials.

### 1.2.2 Running Environment

Minimizing the material budget  $x/x_0$  to 0.3–0.5% per station inside the acceptance is of primary interest. To save also on the material budget of the vacuum window, the detector is placed inside the target chamber in a moderate vacuum ( $\approx 10^{-4}$  mbar). The MVD is placed in the center of the CBM dipole magnet with an integrated magnetic flux density of  $\mathcal{O}(1\text{ Tm})$ . It has to cope with very high track densities in both space and time due to the fixed target geometry of CBM, the very close proximity to the target, and the high interaction rate the experiment aims for. As a result, the detector will accumulate an integral radiation dose of up to 5 Mrad (ionizing) and  $7 \times 10^{13}$   $n_{\text{eq}}/\text{cm}^2$  (non-ionizing) per CBM running year, *i. e.* 2 months of beamtime<sup>2</sup>. This harsh radiation environment poses challenging constraints not only on the dedicated CMOS pixel sensors called MIMOSIS, but also on the choice of all other materials. The sensor technology requires stable sub-0 °C operation during runtime to maintain a high detection efficiency and low fake rate<sup>3</sup>. The ionizing radiation dose on the MVD is shown in figure A.1.

### 1.2.3 Technical Design of the MVD

The technical design is motivated by cutting-edge material budget in the acceptance, vacuum-compatibility, sufficient cooling and mechanical stability. The detector is cooled passively by conduction in the acceptance with active cooling placed in the periphery [1].

The four planar detector stations of the MVD will operate between 8 and 20 cm downstream of the target, equidistantly spaced. This is the day one setup of the MVD, called TR geometry. There is an alternative, second setup with a modified first station, called VX geometry, with four equidistantly spaced stations operating between 5 and 20 cm downstream of the target. The first station in VX geometry has a much disparate occupancy and radiation profile, and uses different supporting materials than the other stations. The setup in VX geometry is currently not followed up in parallel, in particular not in this thesis, as it is not envisioned for day one and features substantial offset costs and resources.

CBM is designed to cover polar angles between 2.5° and 25° in the full azimuth. The geometric acceptance of the MVD matches this to a large extent, with a lack of coverage at small polar angles. This is the result of a quadratic clearance in the center of all stations. This is necessary to allow the beam particles that did not interact with the target to pass without hitting the sensors. Moving the sensors closer to the beam to improve the acceptance towards small polar angles is excluded to minimize the amount of single event effects (SEEs) in the sensors. The geometric acceptance of the MVD exceeds the 25° mark, allowing for tracking of low-momentum tracks that are quickly bent out of the acceptance by the magnetic dipole field before reaching the STS. The geometric acceptance of the MVD is shown in figure A.3.

The baseline detector concept relies on integrating a total of 288 large-area ( $31.15 \times 17.25 \text{ mm}^2$ ), thinned (50  $\mu\text{m}$ ) CMOS monolithic active silicon pixel sensors (MAPS) on both sides of highly heat-conductive carrier sheets of Thermal Pyrolytic Graphite (TPG, 380  $\mu\text{m}$  thick,  $\lambda > 1500 \text{ W/m}\cdot\text{K}$ ). The double-sided integration provides the maximum fill factor over the geometric acceptance. The carriers provide the necessary mechanical stiffness and efficiently conduct the dissipated power to outside of the acceptance. PCVD diamond (synthetic, poly-crystalline, 150  $\mu\text{m}$  thick,  $\lambda > 2000 \text{ W/m}\cdot\text{K}$ ) might serve as carrier material for the first station in VX geometry to minimize the material budget even further for enhanced secondary vertex reconstruction

<sup>2</sup>Part of this dose is accumulated from fragments of the target and ions in beam halo hitting the MVD. This is crucial for a stable sensor operation as they can induce radiation damage due to their high LET, causing SEEs in the electronics. For the passive components, only the absolute absorbed dose is of interest.

<sup>3</sup>Recent studies with the precursing sensors have relaxed the temperature requirement to room temperature [10].

precision<sup>4</sup>. Actively cooled heat sinks located outside of the acceptance evacuate the heat from the sensors and front-end electronics. They also serve as the mechanical frame for the carriers and host the first stage of readout electronics, which is connected via thin flexible printed circuits (FPCs) to the sensors. The cooling channel is optimized for mono-phase, low-viscosity liquid cooling with Novec 649 as the baseline coolant<sup>5</sup>.

Each of the four detector stations comprises four mostly independent sub-modules, called quadrants (sensors-TPG carrier-heat sink-readout). Two different quadrant form factors exist, called geometry *b* and *c*. The two first and two last stations are identical, respectively, providing a high modularity despite the tight space constraints. Table 1.1 summarizes the number of sensors per quadrant for the different MVD stations that are placed on the front- and back-side of the carriers.

Table 1.1: Number of sensors per quadrant for the different MVD stations [1].

Station	Geometry	Number of sensors	
0 and 1	<i>b</i>	Front-side	4
		Back-side	4
2 and 3	<i>c</i>	Front-side	16
		Back-side	12

The detector has an exact fourfold symmetry inside the acceptance. The services of the detector, *i. e.* the cooling pipes and electrical connections, reduce this symmetry to an exact twofold symmetry of the half-detectors. Four half-stations are mounted together to form two independent half-detectors. The half detectors are mounted onto a baseplate that allows for lateral movement of the half-detectors by 50 mm away from the beam<sup>6</sup>. The baseplate is mounted to a quadratic vacuum flange, the front flange. It features all necessary feedthroughs for cooling, powering, data transmission, and vacuum pumping. Both the STS in its box, and the MVD in the target box are placed in the aperture of the dipole magnet. The STS box surrounds the target box on five sides. Therefore, all the services of both sub-systems have to be routed upstream. Figure 1.4 shows a CAD view of the MVD.

#### 1.2.4 Introduction to this Thesis

This thesis focuses on the mechanical integration of quadrants. The integration is challenging as up to 28 thinned sensors and 7 thin FPCs have to be glued and wire-bonded on two sides of one carrier while ensuring a low material budget and vacuum-compatibility.

This thesis will present all the necessities for the mechanical integration of a pre-series module of one of the largest quadrants of the MVD (geometry *c*), finalizing the engineering designs of the components, and elaborating on the selection of materials, the quality assessment and assurance (QA), and the assembly procedures. For the latest prototype PRESTO, MIMOSA-26 sensors were integrated onto a sheet of 500  $\mu\text{m}$  thick TPG for a quadrant of geometry *b* [11, 12]. The techniques developed for the integration of PRESTO have been adapted to the larger form factor of MIMOSIS sensors, integration on thinner (380  $\mu\text{m}$  thick) sheets of TPG, and to the larger form factor of geometry *c*. Based on the experience obtained with PRESTO, the improvement of integration and reworking techniques was addressed in this thesis.

The integration of the MVD is subdivided into two parts, *i. e.* sensor integration and detector integration. Sensor integration denotes all the components, techniques and tools necessary to

<sup>4</sup>The baseline carrier material TPG has been used for all studies in this thesis. The option of using a pCVD diamond carrier is currently not followed up.

<sup>5</sup>Due to possible usage restrictions, the choice of coolant is currently under re-evaluation.

<sup>6</sup>This movement is necessary to prevent a direct beam impact on the detector during beam tuning.

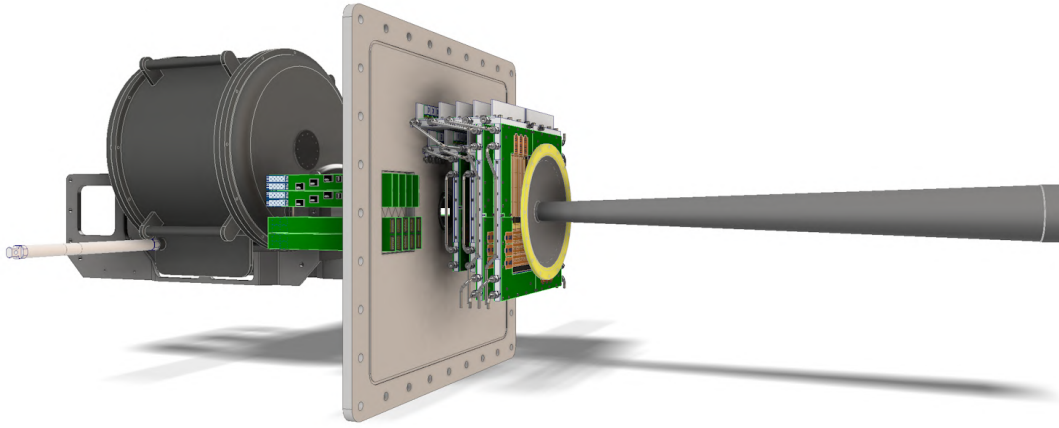


Figure 1.4: Render of the current status of the latest MVD CAD model. The beam comes from the left, passes the target exchange device, and hits the target stationed at the center of the front flange. Included is also the vacuum interface and beam pipe of the STS. The mounting structure of the MVD is not implemented yet. For a detailed discussion of the model, see also appendix A.2.

integrate functioning detector modules, *i. e.* half-stations<sup>7</sup>. Detector integration denotes all components, tools and necessities to integrate detector modules into a detector, including also the electrical integration, a monitoring and detector control system, and the cooling system.

In preparation of a pre-series quadrant, robust and sound procedures of high-yield sensor integration and fine-meshed QA of all components before and after each integration step have been studied. Institutes, industrial companies, and laboratories for processing, integration and QA have been identified. Potential bottlenecks of the mechanical integration, caused by their labor intensive QA (*w. r. t.* time, resources, manpower) and/or intrinsically low yield have been identified.

Chapter 2 introduces all the hardware components necessary for the sensor integration, including a proposed QA procedure and open questions that still need to be addressed before the final integration. Chapter 3 is structured similarly, but for the detector integration. It also includes a detailed review of the MVD cooling system. Chapter 4 summarizes the upgraded integration and high-yield reworking techniques developed within this thesis. A detailed, step-by-step draft of the integration flow is presented.

<sup>7</sup>Concerning the active part of the detector, which is the most difficult to integrate, the smallest functioning unit is the quadrant.

## 2 Sensor Integration

This chapter introduces the different hardware components used for the mechanical integration of the sensors. This includes the dedicated CMOS sensors (MIMOSIS), the carriers, the different adhesives, the readout flexible printed circuits (FPCs), the front-end board, and the heat sinks. All important aspects regarding the mechanical integration, the proposed QA procedure, and open questions are presented. Figure 2.1 shows a CAD view of a quadrant with the different components.

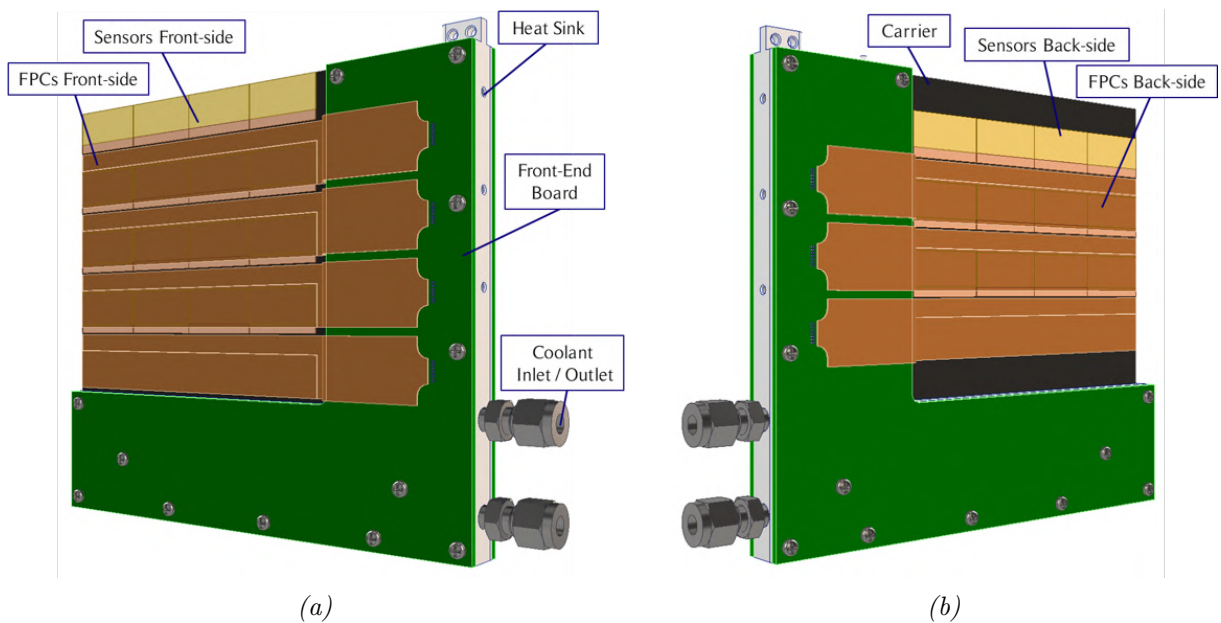


Figure 2.1: CAD view of the front-side (a) and back-side (b) of an MVD quadrant of geometry *c* including all the hardware components introduced in this chapter.

### 2.1 The Sensors

The MVD in its current design will be equipped with a total of 288 CMOS MAPS called MIMOSIS. The sensor is produced in the TowerJazz 180 nm CIS process and is designed by IPHC<sup>1</sup> to provide a spatial precision of  $5\ \mu\text{m}$  and a timing resolution of  $5\ \mu\text{s}$ , with a peak rate capability of  $80\ \text{MHz}/\text{cm}^2$  [1]. It is currently in the research and development phase with the first full-scale prototype called MIMOSIS-1 being intensively tested since 2020. In the studies of this thesis, MIMOSIS-1 sensors have been worked with. From an integration point of view, the prototype MIMOSIS-1, the succeeding prototype MIMOSIS-2, and the final sensor MIMOSIS-3 are identical. For all work related to this thesis, the properties of MIMOSIS-1 are representative for those of MIMOSIS-2 and -3, as the focus lies on the mechanical properties of the sensors, *i. e.* the form factor<sup>2</sup> and the bonding scheme, all of which are finalized.

<sup>1</sup>The Hubert Curien Pluridisciplinary Institute Strasbourg.

<sup>2</sup>due to a larger tolerance in the dicing of the prototype sensors, the actual MIMOSIS-1 and -2 sensors are slightly ( $\mathcal{O}(50\ \mu\text{m})$ ) larger than MIMOSIS-3 will be. This will be discussed further in chapter 4.1.2.

The sensor features:

- A pixel array of  $504 \times 1024$  pixels
- An active area of  $30.97 \times 13.55 \text{ mm}^2$
- A total area of  $31.15 \times 17.25 \text{ mm}^2$

The sensors are thinned to  $50 \mu\text{m}$ , minimizing their material budget  $x/x_0$  to 0.053%.



Figure 2.2:  $300 \mu\text{m}$  thick MIMOSIS-1 sensor held with a vacuum pick-up tool. The active pixel matrix is visible in the upper part of the sensor and the passive digital part is visible at the lower part of the sensor [13].

The required end-of-lifetime (EOL) dose of the sensor is 5 Mrad (ionizing) and  $7 \times 10^{13} \text{ n}_{\text{eq}}/\text{cm}^2$  (non-ionizing), which the most exposed sensors will accumulate in a single CBM year (*i. e.* 2 months of beamtime)<sup>3</sup>. These values fix the constraints *w. r. t.* radiation hardness of all other components. The harsh radiation introduces damages in all structures of the sensors which deteriorates their performance. Some effects, *e. g.* the rise of leakage currents due to non-ionizing radiation, can be mitigated by active cooling. This defines the operation temperature of the sensors of  $\sim 0^\circ\text{C}$ .

The prototype MIMOSIS-1 features two different pixel types: Half of the pixels on the matrix employ a DC-coupling between the sensing element and the amplification chain, and half of the pixels use an AC-coupling. The final sensor, MIMOSIS-3 will most likely feature only AC-coupled pixels. Therefore, only results for AC-coupled pixels are presented here. The performance of MIMOSIS-1 under radiation has been studied extensively and is up to the specifications, even for EOL ionizing doses, see figure 2.3.

A well-known effect of ionizing radiation in CMOS chips is a threshold-voltage shift in both n- and p-channel MOS transistors [14]. In the MIMOSIS sensors, the signal charge detected with a collection diode is amplified and then compared to a DC voltage generated by on-chip DACs. These are built of transistors, whose working points can shift after irradiation. This translates to a shift of the detection threshold of MIMOSIS sensors, depending on the level of irradiation which is strongly dependent on their placement in the detector. The necessity to correct for that by actively re-adjusting the steering voltages that set the thresholds partially defines the specifications of the FPCs and the front-end electronics, see also chapters 2.4 and 2.5.

This threshold shift does not scale linearly with the dose, but saturates [14]. Recent studies suggest a saturation within around 1 Mrad, which is shown exemplarily in figure 2.4a. After reaching a saturation limit, no readjustment of any steering voltages would be necessary at higher doses. A detailed study of this effect in MIMOSIS sensors is work in progress to confirm the saturation and the corresponding dose, called pre-conditioning dose, and to confirm that the performance of the chip is still inside the specifications after reaching the pre-conditioning dose plus EOL dose.

<sup>3</sup>The radiation field is strongly inhomogenous due to the magnetic dipole field of CBM and the high multiplicity of  $\delta$ -electrons in heavy-ion collisions [1].

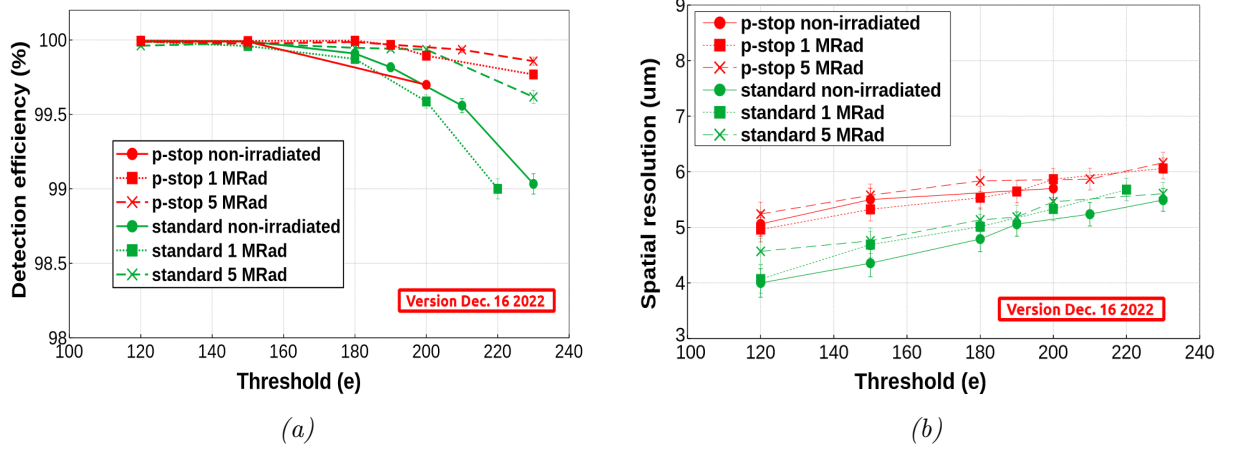


Figure 2.3: Detection efficiency (a) and spatial resolution (b) as a function of the threshold for MIMOSIS-1 AC-pixels for two different doping profiles of the epitaxial layer (‘standard’ and ‘p-stop’) before irradiation, after 20%, and after 100% of the EOL ionizing dose. All measurements were taken at  $+15^{\circ}\text{C}$  [10].

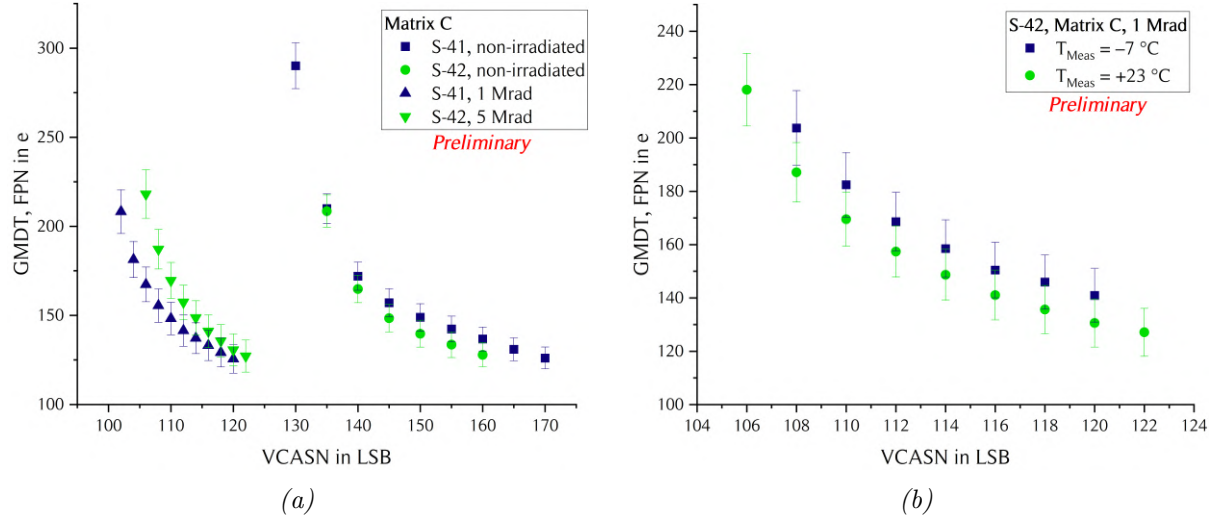


Figure 2.4: Measured global mean detection threshold (GMDT, indicated by symbols) and fixed pattern noise (FPN, indicated by vertical bars) as a function of the threshold set on the on-chip DACs for MIMOSIS-1 AC-pixels (a) of two different sensors before irradiation, after 20%, and after 100% of the EOL ionizing dose, respectively, and (b) of a single chip after 20% of the EOL ionizing dose for different temperatures [15].

To make use of the saturation of the threshold shift in the MVD, all sensors would have to be irradiated to a pre-conditioning dose of  $\sim 1$  Mrad before use in the MVD. This could guarantee a uniform response of the sensors over the whole detector for a whole beamtime despite the large inhomogeneities in the radiation field with gradients of up to 100% over a single sensor.

The MIMOSIS sensors can be electrically connected to powering, steering and readout with  $25\ \mu\text{m}$  Al wire bonds on the 151 bonding pads which are distributed in one row along the edge of the chip on the long side of the digital part. The pads have different purposes:

- 30 pads for the analog and digital power (1.8 V)
- 7 pads for the top- and back-biasing ( $-6, \dots, 0$  V, default:  $-1$  V and  $0, \dots, 20$  V, default: 10 V, respectively)

- 34 pads for the analog and digital GND
- 18 pads for the serial data output
- 10 pads for the clock
- 6 pads for the I<sup>2</sup>C communication
- 8 pads for reset and synchronization
- 10 pads for monitoring purposes
- 6 pads for markers
- 16 pads for the analog pixel injection
- 6 pads for the analog pixels

The sensor features a configurable number of serial data outputs. The output mode, *i. e.* the number of active data links of the chip, is hard-wired by the bonding scheme to 1, 2, 4, or 8 active serial data outputs. The occupancy drastically depends on the placement of the sensor inside the detector and hence not every sensor needs to run all eight data outputs.

The powering voltage for the sensors will be provided by radiation-hard FEAST DC/DC converters [16]. The digital power consumption of a single chip (factory new and after EOL doses) is shown in figure 2.5a. The analog power is below 30 mW which is small compared to the digital power. The total, idle power consumption of the chip is reduced by 22% with 2 instead of 8 active data outputs (simulated for a non-irradiated chip). The power density is very inhomogeneously distributed with a high power density  $\mathcal{O}(300 \text{ mW/cm}^2)$  in the passive, digital part in the periphery of the chip, and only  $\mathcal{O}(10 \text{ mW/cm}^2)$  on the pixel matrix [17]. Figure 2.5b shows the efficiency of the FEAST DC/DC converters for different input voltages and different loads.

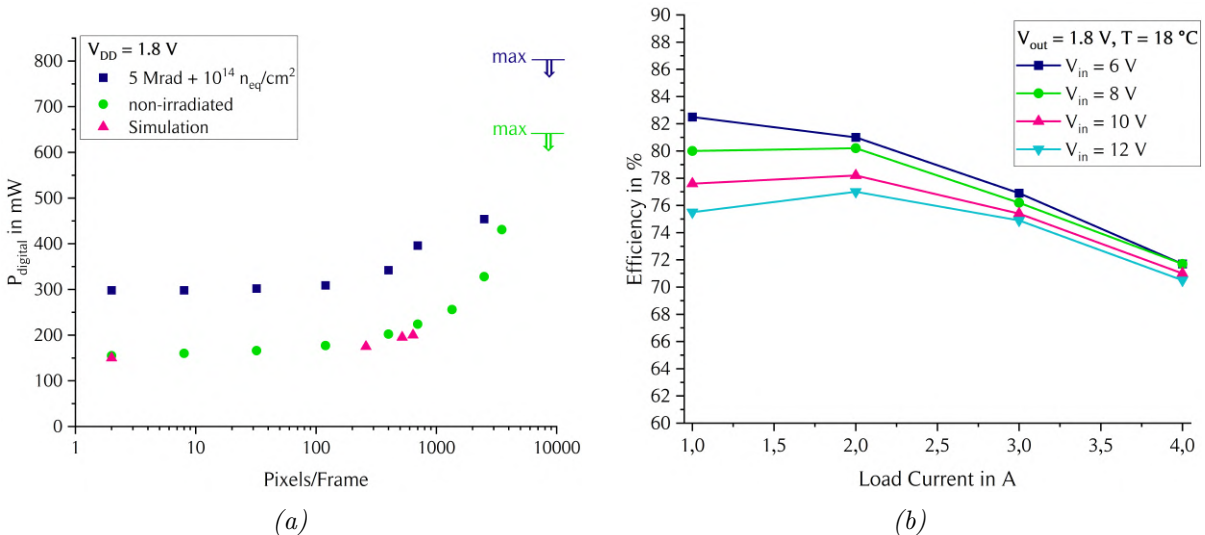


Figure 2.5: Power consumption (digital part) of MIMOSIS-1 (simulated, before irradiation, after EOL irradiation) for different occupancies with all data outputs active (a). The area of interest of the occupancy extends to  $\sim 1000$  pixels per frame [17–19]. Efficiency of FEAST DC/DC converter (variable input voltage, 1.8 V output, at  $18^\circ \text{C}$ ) for different output loads (b), taken from [16].

### 2.1.1 Proposed QA Procedure

The sensors can be visually inspected for obvious damage after thinning and dicing. The quality, electrical functionality and performance of the sensors can be assessed with needle probe testing. A custom needle probe card is used to power, program, and read out the chip [20].

A QA procedure has been proposed within this thesis. It is a sequence of 8 consecutive tests ranging from simple powering to a detailed characterization of every pixel. If a chip fails the powering test, all subsequent tests are omitted. The test procedure is only discussed qualitatively here. The implementation of the test procedure in a standalone TRB-based readout system is work in progress and is being optimized for MIMOSIS-1 in a collaborative effort of the working group. Qualitatively, the test procedure for MIMOSIS-2 and -3 will be identical, but the parameters and limits might have to be reiterated. The 8 tests are:

1. Powering Test

This test allows for spotting connectivity issues on the powering lines and for finding intrinsic issues on the power grid. The power consumption of the analog and of the digital part of the sensor are measured and compared to their nominal values which depend on the occupancy.

2. Back-Bias Scan

This test allows for spotting irregularities in the biasing. The back-bias current is measured with an ammeter.

3. Register Test

This test allows for spotting connectivity issues with the I<sup>2</sup>C-communication and for checking the functionality of all r/w registers. Several test patterns are written to and read back from the r/w registers.

4. DAC Scan

This test allows for checking the functionality and linearity of all steering DACs. The output of the DACs is measured with an external ADC.

5. Test of Data Outputs

This test allows for checking the functionality of all eight data outputs. This is extracted from the readout software.

6. Analog Scan

This test allows for finding a working range for the sensor. For this, several lines of pixels are pulsed with a pulse of a fixed charge for different thresholds using the in-pixel pulsing mechanism.

7. Threshold Scan

This test allows for measuring the mean detection threshold, thermal noise, and fixed pattern noise, and for finding broken, dead, and noisy pixels<sup>4</sup>. For this, all pixels are pulsed and their s-curves are taken.

8. Fake Hit Rate

This test allows for measuring the fake hit rate. The value can be extracted from the previous scans by counting the pixels that fire frequently at a high threshold, even though they are not pulsed.

---

<sup>4</sup>Broken pixels are pixels that can not be masked.

The quality assessment of the sensors can technically be done at a manual prober bench in the IKF cleanroom. It is however recommended to share the workload with other institutes. Manual probe testing is a very time-consuming process<sup>5</sup> and automatization options are very limited at the available prober bench at IKF. Substantial connectivity problems have been observed in preliminary tests which were traced back to a very high contact resistance. This is almost certainly caused by a build-up of aluminum oxide on the bonding pads<sup>6</sup> and possibly other residue. This translates to the necessity of performing  $\sim 10$  touchdowns per chip at a significant overdrive of  $\sim 100 \mu\text{m}$ , which rapidly deteriorates the alignment and cleanliness of the needle tips. For preliminary tests, the oxide layer was removed in a wet-etching process using a diluted phosphoric acid (1.02 / 1.00 by weight). The sensor was soaked in the etching bath for 15 s at  $50^\circ\text{C}$ , then rinsed in three acetone baths, and afterwards dried with nitrogen. A visible inspection shows a significant improvement of the cleanliness of the bonding pads, see figure 2.6. The rest of the sensors, *i. e.* the CMOS structures on the front-side and the bare silicon back-side, did not show any collateral damage from the etching procedure. The electrical connection of the sensor with the probe card was however significantly improved. A stable and reliable contact was established already after one touchdown with an overdrive of  $70 \mu\text{m}$ . Nonetheless, long-term effects should be studied to validate the wet-etching process. This includes the performance after re-oxidation, the quality of bonding and general observations of a possible degrading of the surface, also after storage in a dedicated, low-oxygen-level container. Additionally to the phosphoric acid, a commercially available cleaning solution has been identified (VIGON<sup>®</sup> PE 196A [21]). It is a water-based, alkaline cleaning fluid which inhibits the surface after cleaning, slowing down the re-oxidation process after cleaning. In preliminary tests, the functionality as cleaning agent for the bonding pads could be confirmed. Detailed material compatibility studies are, however, still work in progress. No concluding probe testing results can be presented in this thesis as this is also still work in progress.

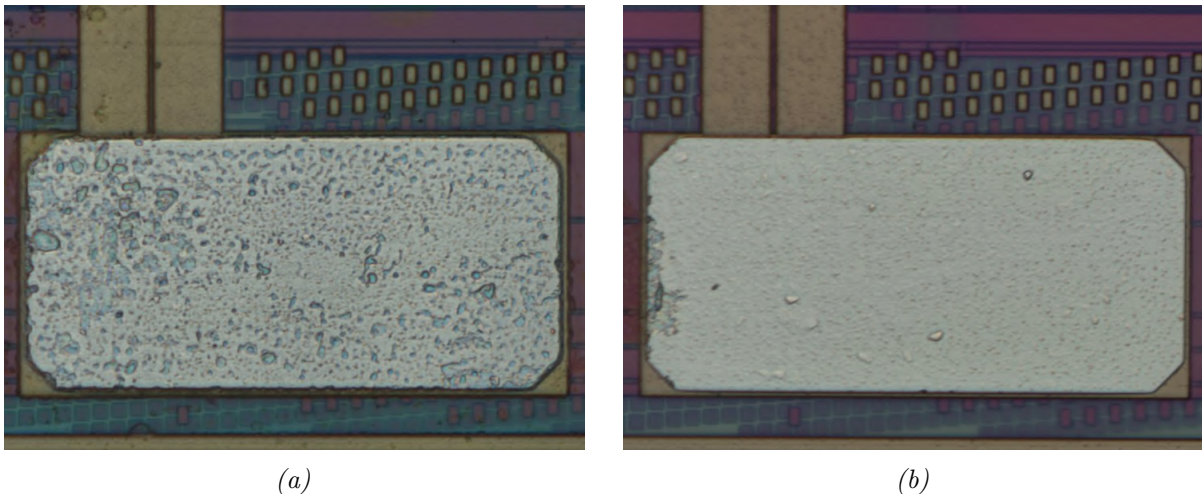


Figure 2.6: Picture of two bonding pads on MIMOSIS-1, one before (a), and one after (b) the etching procedure using diluted phosphoric acid as cleaning agent.

### 2.1.2 Open Questions

From a mechanical point of view, the MIMOSIS chip is already finalized. Also, the handling of the fragile thinned sensors is not a problem with the equipment available in the IKF and GSI

<sup>5</sup>The test time is estimated to be longer than 15 minutes per sensor including the placement of the sensor on the jig.

<sup>6</sup>The sensors have been stored for more than two years prior to probe testing, so this is not surprising.

laboratories. The open questions regarding the sensors are concerning a possible pre-conditioning, the quality assessment, the electrical integration, and the performance in a realistic environment.

- Pre-conditioning

If a saturation of the threshold shift at  $\sim 1$  Mrad is experimentally confirmed and the sensor still fulfills the specifications at the pre-conditioning dose plus the EOL dose, the feasibility of pre-conditioning all MVD sensors needs to be carefully evaluated. A focal point should be the technical implementation, which is significantly constrained by the fact that the sensors have to be powered and programmed during the pre-conditioning. Here, also the available resources need to be taken into account. In the R&D phase, the irradiation campaigns have been done in the laboratories of the Institute für Experimentelle Teilchenphysik (ETP) at the Karlsruher Institut für Technologie (KIT), where it takes about 4 hours to irradiate one sensor to 1 Mrad at the highest dose rate. While this is feasible for single sensors, it can not be scaled up for mass-production, *i. e.*  $\mathcal{O}(500)$  sensors.

- Quality Assessment

The implementation of the QA script set up for a TRB-based readout has to be concluded and the parameters and limits have to be optimized for the probe testing of the 26 unbonded MIMOSIS-1 at IKF [22]. MIMOSIS-2 and -3 should be tested and bonded as quickly as possible, best inside a few weeks after production, to minimize build-up on the pads. Therefore, it is recommended to share the workload between different institutes. Also, a dedicated solution for long-term storage of unbonded sensors, *e. g.* a nitrogen- or argon-flushed, sealed container should be defined. The parameters and limits of the QA script, which have to be determined experimentally, most likely have to be adapted to MIMOSIS-2 and -3. In total,  $\mathcal{O}(500)$  MIMOSIS-3 sensors have to be tested for the final MVD.

- Electrical Integration

There is a substantial amount of open questions regarding the electrical integration of the sensor. This is in line with a transition in the powering and readout scheme of the sensors. Until now, the focus was given to a high-precision characterization of the sensors' performance in the laboratory and to finding possible ways of improvements. Therefore, the sensors were mounted onto PCBs that combined all the necessities, while also including several decoupling capacitors mounted in the close proximity to the sensor to minimize noise. This environment does not reflect the setup of the MVD. As a next step towards integrating these sensors in the MVD, the powering with the radiation-hard FEAST DC/DC converters and the reading out over long, unshielded, single-layer FPCs is studied. The supply voltage range and acceptable noise level for a stable and reliable operation of the chip needs to be measured as well as the performance of sensors powered with FEAST DC/DC converters. Moreover, the performance needs to be measured for different cable lengths and in the absence of decoupling capacitors on the power lines close-by the sensors. Also, the performance needs to be measured with an MVD FPC which is, due to space constraints, not routing every connection of the sensor.

- Realistic Environment

MIMOSIS-1 has been extensively tested to validate its radiation hardness and resolution. The performance of the sensors should be tested also in a realistic environment before finalizing the design. The sensors should be able to run stably over long periods of times in a noisy environment with drastic occupancy fluctuations in space and time. A possible test stand for this could be the mCBM setup at SIS 18. Additionally, the performance with different temperature gradients across the matrix and the dependence on the absolute temperature should be validated for a smooth operation in the MVD.

## 2.2 The Carriers

The carrier is the mechanical support of the sensors and the readout FPCs inside the acceptance and conducts the heat dissipated by the sensors to an actively cooled heat sink outside the acceptance. The high-performance material Thermal Pyrolytic Graphite (TPG) has excellent thermal conductivity ( $\gtrsim 1500 \text{ W/m}\cdot\text{K}$  in the plane [23]) and is, with a thickness of  $380 \mu\text{m}$  ( $x/x_0$  of 0.200%), self-supporting. It is the baseline carrier material for all MVD stations in TR geometry.

TPG is an orthotropic material. It features a lot of macro-structure as the material is composed of several layers of small ( $\mathcal{O}(5 \text{ mm})$ ) very thin flakes which are only loosely bound, leading to a surface roughness of  $\sim 70 \mu\text{m}$ , see also figure 2.7. This roughness can be significantly reduced by polishing the sheets, which can either be done by the manufacturer or in a wet-grinding process at IKF. It is necessary to integrate only on polished TPG to allow for thin and even layers of glue. This ensures a low material budget, a sufficient thermal interface, and vacuum-compatibility.

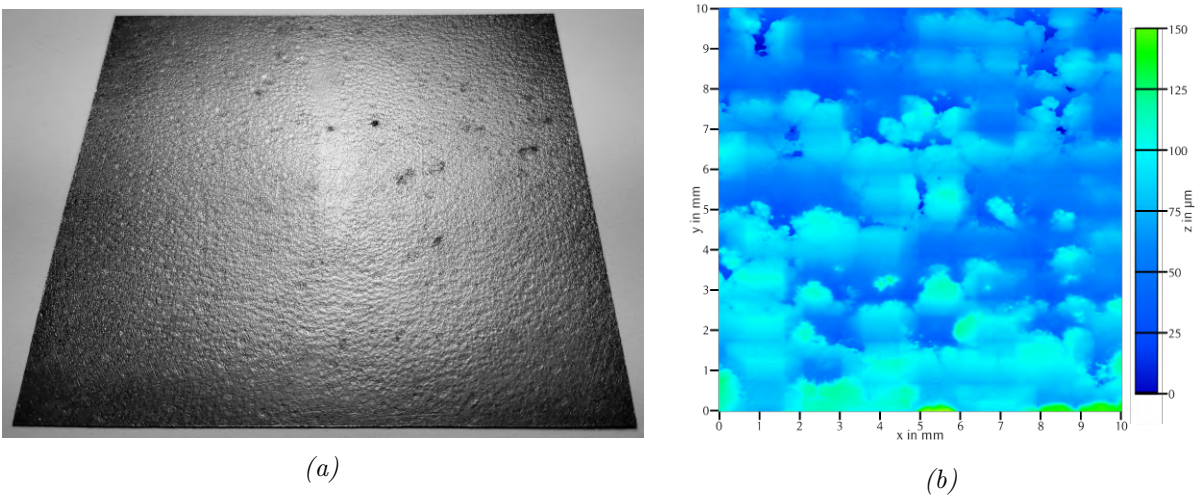


Figure 2.7: Picture of a sheet of bare, unpolished TPG (a). 3D-scan of the surface of a sheet of bare, unpolished TPG (b).

The form factors of the carriers of geometry  $b$  and  $c$  have been reevaluated and slightly changed from the TDR in the context of this thesis. The changes are related to the width of the FPC which is discussed in chapter 2.4. The updated values can be found in table 2.1.

Table 2.1: Form factors of the carriers of geometry  $b$  and  $c$  as stated in the TDR and the updated values found in the context of this thesis.

Geometry	TDR value in mm $\times$ mm	Updated value in mm $\times$ mm
$b$	$81.9 \times 85.7$	$82.0 \times 91.7$
$c$	$143.9 \times 124.9$	$143.8 \times 130.7$

Many TPG sheets are delivered with non-right angles and not-straight cuts along the edges. It is recommended to buy sheets with an excess of  $\sim 10 \text{ mm}$  over the final form factor on two adjacent sides. The sheets can then be machined to the correct form factor using an industrial laser vaporization cutter, which is discussed in chapter 4.1. Additionally to the imperfect angles and edges, some large-area TPG sheets have quite sizeable deviations from perfect planarity of up to  $\sim 3 \text{ mm}$ . This can not be corrected and those sheets are therefore not to be used in the MVD.

TPG is a form of graphite and as such it features a non-negligible electrical conductivity. An electrically insulating, radiation-hard, and surface-true coating of less than  $\sim 5 \mu\text{m}$  thickness

is mandatory and can be done with parylene-C in a CVD process<sup>7</sup>. This coating ensures a sufficient dielectric strength and, as a positive side effect, also increases the stability of TPG against abrasion. The hydrophobicity and bad wettability of parylene are significant drawbacks that become apparent during gluing. This is further discussed in chapter 2.3.

Despite the drawbacks of the surface structure, planarity, and the need to coat the material, TPG is close to being the ideal carrier material for the MVD due to its excellent thermal and mechanical properties, a sizeable radiation length (19.03 cm), commercial availability in the necessary form factors at manageable cost (0.15 €/mm<sup>3</sup> in 2020), and its machinability [1].

The carrier can be structured with a laser vaporization cutter to significantly ease the integration. This is discussed in detail in chapter 4.1.2. The .dxf sketches of the carrier can be found in [25].

### 2.2.1 Proposed QA Procedure

The quality assessment for the carriers includes a visual and a thermal inspection:

#### 1. Visual Inspection

This test allows for spotting visible damage of the sheets *s. a.* cracks and delamination, and for measuring their flatness. Sheets with visible damage and a flatness exceeding 500 μm should be rejected<sup>8</sup>.

#### 2. Thermal Inspection

This test allows for estimating the thermal performance of the TPG sheets when clamped into a heat sink. A resistive heater can be placed on the excess at the corner furthest away from the heat sink, producing a large, localized heat entry. The temperature distribution and the gradient between the hottest and the coldest point on the carrier are measures for the thermal performance and can be assessed using an IR camera. Sheets with visible deviations from a symmetric temperature distribution over the carrier should be rejected. The temperature gradient on the carrier must not exceed 160 K/m (hottest point for geometry *b*: ~20 K, geometry *c*: ~30 K) anywhere for 10 W of heating power with the heat sink actively cooled to ~0 °C<sup>9</sup>.

The quality assessment can be done in the laboratories at IKF where all the necessary equipment is available and, with a dedicated test stand for thermal assessment of MVD quadrants, already set up and running.

### 2.2.2 Open Questions

Especially for the smaller stations of geometry *b*, where the thermal and mechanical requirements are much more lenient, the feasibility of integrating on even thinner TPG carriers with a thickness of 250 μm needs to be studied<sup>10</sup>. The very thin sheets require more delicacy in handling, as they are more fragile. Nonetheless, they are self-supporting, even at form factors of geometry *c*. A change from 380 to 250 μm equals a reduction of the total material budget  $\frac{x}{x_0}$  by ~0.07% over the whole geometric acceptance to significantly reduce multiple scattering in the first two MVD stations.

<sup>7</sup>Parylene-C does not penetrate as deeply into TPG as other types and is the most economical option [24].

<sup>8</sup>This value is determined by the machinability of TPG with an industrial laser vaporization cutter, a processing technique developed and optimized within this thesis, see also chapter 4.1. A high planarity is also beneficial for the detector alignment, this is however secondary here, as deviations from perfect alignment can be corrected for in software.

<sup>9</sup>This value has been determined in thermal simulations.

<sup>10</sup>250 μm is the thinnest commercially available thickness of large-area TPG sheets.

## 2.3 The Adhesives

There are three different applications for adhesives in the MVD:

1. Gluing of the sensors
2. Gluing of the FPCs
3. Thread sealing of fittings

Suitable options for the different applications have been identified. Certain requirements have to be fulfilled by all adhesives:

- Sufficient radiation hardness
- Vacuum compatibility, low outgassing
- Possibility to cure at room temperature
- Reliable availability, preferably commercially

Radiation hardness and vacuum-compatibility are constraints dictated by the running environment of the MVD. For the liquid adhesives identified, room temperature curing is important. Curing the glue at significantly higher temperatures than the operation temperature could introduce significant thermal stresses on the components. Commercial availability includes a stable and reliable supply of sufficient quantities with consistent quality and properties. This is especially crucial for the mass production as most adhesives have a short shelf-life of  $\mathcal{O}(1\text{ y})$ .

### Sensor

The adhesive joins the sensors mechanically to the carrier. The layer should be as thin as possible to ensure a low material budget while also providing a homogeneous gluing surface for the large-area sensors, evening out the surface roughness of the TPG carrier. Glues are typically bad heat conductors, so thinner layers will result in smaller temperature gradients between the sensor and the carrier. Hence, a low viscosity liquid glue should be used. A sufficient wetting of the parylene-coated surface has to be ensured, such that the capillary forces in the glue produce a thin and even layer. The thermal conductivity of the glue is irrelevant as the thin layer will not affect the overall thermal performance.

The mismatch of the coefficients of thermal expansion (CTEs) of the sensors (Si:  $2.6 \cdot 10^{-6}/\text{K}$ ) and the carrier (TPG:  $\sim 0 \cdot 10^{-6}/\text{K}$ ) is small and is not expected to be important in the MVD [26]. Nonetheless, a residual elasticity of the glue after curing can be beneficial in reducing the thermal stress on the sensors. Furthermore, the glue should cure in  $\mathcal{O}(1\text{ day})$  at room temperature to keep the total temperature swing between integration and operation small. Two different glues have been selected based on these considerations. One glue, EpoTek 301-2, is produced by Epoxy Technology and commercially available at different suppliers [27]. The other one, RAL-247, is custom-made by the Rutherford Appleton Laboratory (RAL) [28]. Their most important properties are listed in table 2.2.

Air bubbles can be trapped inside the glue during the mixing of these two-components resins. These have to be removed prior to the gluing of the sensor to ensure the vacuum-compatibility of the assembly. It is recommended to outgas the Epo-Tek 301-2 in a moderate vacuum for about an hour [30]. Alternatively, bubbles can be removed in a centrifuge.

<sup>11</sup>Epo-Tek 301-2 is the semiconductor-grade version of Epo-Tek 301.

<sup>12</sup>These are the values for the latest batch. An older batch cured in less than 48 h at  $+50\text{ }^\circ\text{C}$  before reaching its shelf life and an even older batch cured in 24 h at  $+20\text{ }^\circ\text{C}$  before reaching its shelf life. Strong batch-to-batch fluctuations have been observed.

Table 2.2: Properties of the adhesives selected for the gluing of the sensors [1, 29–34].

Properties	Epo-Tek 301-2 <sup>11</sup>	RAL-247
Type	Two-component epoxy	Two-component resin
Manufacturer / vendor	Epoxy Technology	RAL (custom-made)
Curing time	3 h at +80 °C 48 h at +23 °C	> 240 h at +80 °C <sup>12</sup> Not at +20 °C
Viscosity before curing in mPa · s	260	~ 100
Elasticity after curing in MPa	3700 at +20 °C 4100 at -20 °C	10 at +20 °C 16 at -20 °C
CTE in 10 <sup>-6</sup> /K	61	Unknown
Radiation length in cm	35	Unknown
Radiation hardness	Sufficient	Sufficient
Surface wetting	Sufficient (using plasma activation)	Sufficient (using a wetting agent)

Both glues have bad surface wetting properties on the hydrophobic parylene coating. The difference between the surface energies of bare and of parylene-coated TPG is shown in figure 2.8a. To account for that in case of the RAL-247 resin, a wetting agent has been provided by the vendor. It has been determined that adding ~ 1.0% by weight to the mixture provides a sufficient wetting of the surface in tests gluing glass dummies onto parylene-coated TPG, see figure 2.8b. While the surface wetting properties get better with a higher amount of wetting agent, it also significantly increases the viscosity of the glue before curing. In general, more glue has to be used leading to thicker layers. The amount of wetting agent does not appear to affect the curing time.

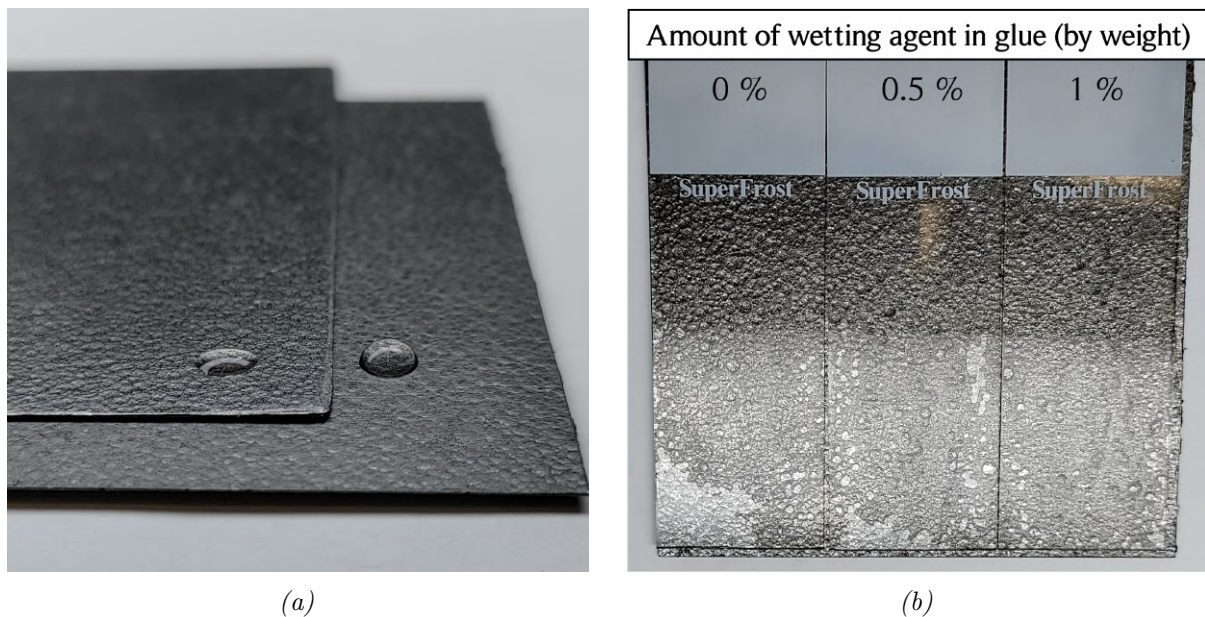


Figure 2.8: Water droplets on polished, uncoated and polished, parylene-coated TPG, demonstrating the hydrophobic nature of the coating (a). Glass plates glued onto polished, parylene-coated TPG using RAL-247 with different amounts of wetting agent (b). Air bubbles are visible that are caused by an insufficient surface wetting of the glue.

The EpoTek 301-2 epoxy is not optimized for primers or wetting agents. Instead, a treatment of the parylene surface by the means of plasma activation to increase the surface energy from 28 mN/m (surface energy of bulk parylene [35]) to the required 47 mN/m is recommended [36]. In preliminary studies at an external company specialized on parylene coating and plasma activation (Plasma Parylene Systems GmbH, Rosenheim, Germany [37]), an increase of the surface energy to 68 mN/m could be achieved by plasma activation. This higher surface energy was stable for 7 days [38]. This value has been determined for storage at room temperatures using a test ink.

It has been determined experimentally that an amount of 17  $\mu\text{l}$  is sufficient to glue the sensors with a thin and even layer on well-polished TPG. This corresponds to a thickness of the layer of  $\sim 30 \mu\text{m}$  ( $x/x_0$  of  $\lesssim 0.010\%$ ). During the integration of PRESTO it was determined that one large drop of glue was sufficient to glue MIMOSA-26 sensors with the lower viscosity RAL-247 glue. The capillary forces were strong enough to spread the glue homogeneously underneath the whole area of the sensors. For gluing the MIMOSIS sensors with the larger form factor using the higher viscosity Epo-Tek 301-2 glue, this is not sufficient. Instead, a more elaborate pattern has to be employed to ensure a proper spreading of the glue, also towards the corners and edges. The relating studies are presented in appendix A.4. They include pictures from infrared photography as a way to make the glue distribution underneath the silicon visible, making use of the infrared transmissivity of silicon. The optimized gluing pattern, amount of glue, and the distribution of glue underneath the sensor dummy throughout the curing time is shown in figure 2.9 for polished, uncoated TPG and figure 2.10 for polished, parylene-coated, plasma-activated TPG.

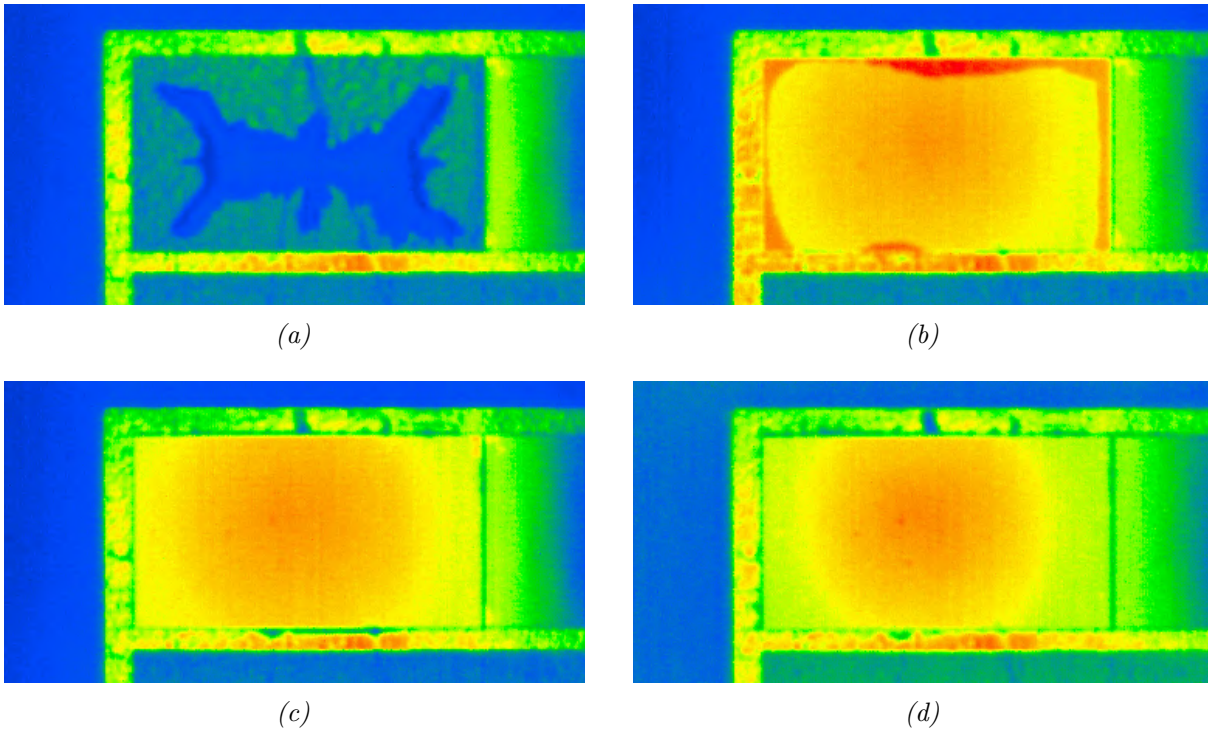


Figure 2.9: Infrared photos of the glue distribution on a polished, uncoated TPG carrier. (a) shows the distribution of the glue before placing the dummy, (b) two seconds and (c) two minutes after placing the dummy, and (d) after curing.

In direct comparison of figures 2.9 and 2.10, the difference between the surface energies of bare, and of parylene-coated and plasma-activated TPG is visible in the glue distribution, especially at the edges. In case of the coated TPG, the glue spread properly, but the amount of glue was not sufficient. This can be traced back to the different levels of polishing of the coated and uncoated TPG. Nonetheless, plasma activation appears to be a proper solution to providing a homogeneous layer of glue on a parylene-coated surface. The continuation and finalization of these studies on

coated TPG, including also a local, stand-alone plasma-activation device is a crucial step towards the production of an MVD pre-series module.

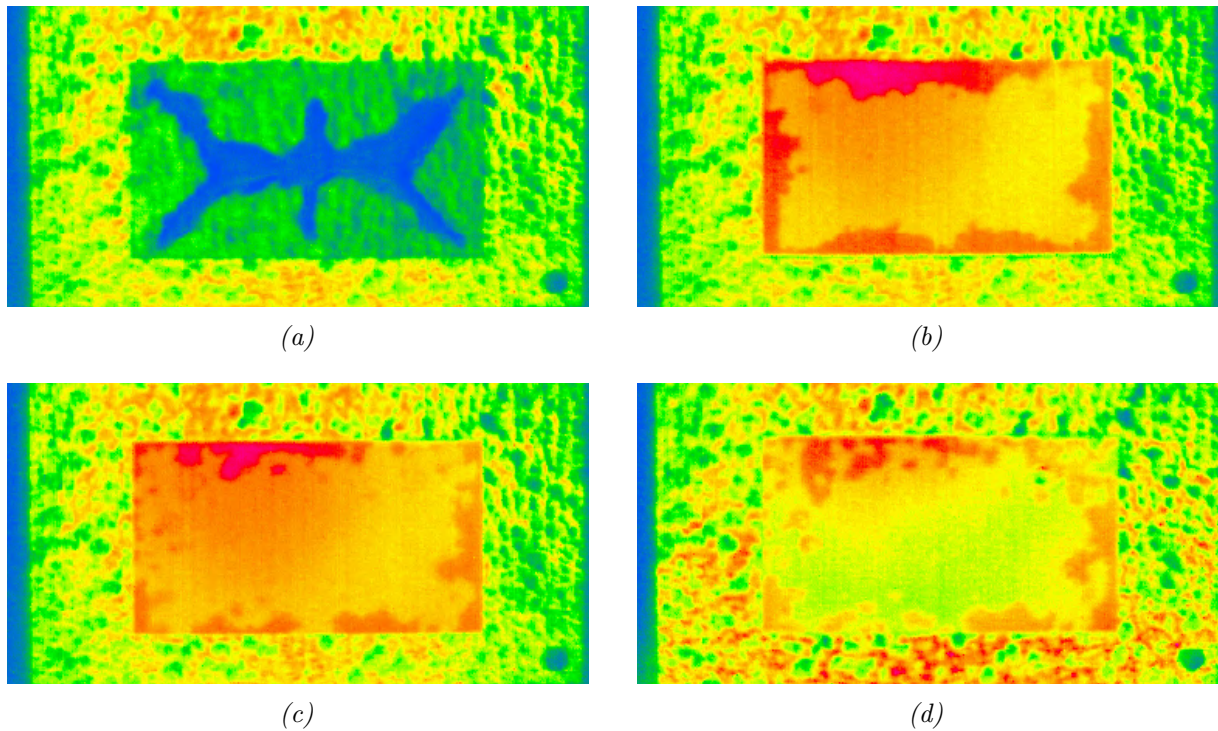


Figure 2.10: Infrared photos of the glue distribution on a polished, parylene-coated TPG carrier. (a) shows the distribution of the glue before placing the dummy, (b) two seconds and (c) two minutes after placing the dummy, and (d) after curing.

Currently, there is no experience with alternative low-viscosity liquid glues at IKF. While RAL-247 has an outstandingly low viscosity and high elasticity, the downsides outweigh these features. There are very large batch-to-batch fluctuations in the curing time and very limited support from the manufacturer. The latest batch delivered does not cure at room temperature. A detailed study would be necessary to determine a proper curing procedure at higher temperatures. The availability in the future is uncertain.

It is recommended to use Epo-Tek 301-2 for gluing the sensors on the TPG. The higher stiffness of the glue has to be weighed up against the reliable commercial availability and consistent properties. The temperature swings between integration (room temperature) and operation ( $\gtrsim 0^\circ\text{C}$ ) are however small which minimizes thermal stress by default.

## FPC

During prototyping it has been determined that the gluing of the FPC is the integration step with the worst yield. Ideally, the FPC is fixed to the surface with a thin and even layer of adhesive. This is difficult to realize as the FPC is a very flexible object with a long and thin gluing area ( $\sim 150 \times 5 \text{ mm}^2$ ). A low-viscosity liquid glue can provide thin and even layers. However, the large capillary forces can push the glue towards the sensors, covering the bonding pads. The capillary forces are much smaller in high-viscosity glues. Producing very thin layers with a high-viscosity glue is however not possible. The assembly risk has to be balanced against material budget when opting for liquid adhesives<sup>13</sup>. An option of the carrier with a special structure to mechanically impede the flow can alleviate the problem of the unwanted capillary effects of the low-viscosity

<sup>13</sup>The FPCs of the last prototype PRESTO have successfully been glued using the low-viscosity glue RAL-247.

glue. This is discussed in more detail in chapter 4.1.2. Additionally to the baseline glue for the sensors (Epo-Tek 301-2), a high-viscosity glue (Loctite Ablestik 45) has been identified.

Double-sided Kapton tape can serve as an easy-to-use alternative to liquid glues. This very different approach, which has been excluded during the prototyping phase due to inconsistent vacuum-compatibility, has been reevaluated. A thin tape (25  $\mu\text{m}$  Kapton 100HN foil, 60  $\mu\text{m}$  total thickness,  $x/x_0$  of 0.020%) fulfills the specifications *w. r. t.* radiation hardness, material budget, vacuum-compatibility and commercial availability. It features an acrylic adhesive with high adhesive strength. The tape can easily be cut and structured to any desired form factor using a scalpel. A proper structuring of the tape can prevent larger pockets of air forming underneath the tape on the rough surface of the TPG to ensure vacuum-compatibility<sup>14</sup> while having a large area of adhesion. The studies have been concluded with an ultra-thin FPC designed for the MIMOSA-26 sensor that has mechanical specifications representative of the final MVD FPC. A strip width of only 5 mm, covering only the width of the bonding pads, has been deemed sufficient for a stable adhesion of the FPC on polished and parylene-coated TPG. Small air bubbles with a diameter of  $\lesssim 100 \mu\text{m}$  remain on the gluing layers. No issues with the vacuum-compatibility, *s. a.* a lifting-off or a visible deformation of the tape or FPC have been observed, so these are not expected to be an issue with the long-term vacuum-compatibility of the assembly.

The tape has to be attached to the carrier and the FPC with sufficient contact pressure. This is possible using a dedicated jig supporting the carrier, especially for the integration of the back-side which happens subsequent to the integration of the front-side. The gluing of the FPC is reworkable with the double-sided tape, an additional advantage over the epoxy solutions. This is only true if the carrier is coated, which is discussed in detail in chapter 4.2. It is not expected that the quality of the wire bonding on the thin FPCs with the rather soft Kapton tape and the small air bubbles underneath is significantly worse compared to the epoxy solutions if a sufficient mechanical support of the carrier is guaranteed during the bonding process.

Table 2.3 summarizes the most important properties of the high-viscosity glue and the double-sided tape selected for the gluing of the FPC.

Table 2.3: Properties of the high-viscosity glue and the double-sided tape selected for the gluing of the FPCs [39–43].

Properties	Ablestik 45 <sup>15</sup>	Kapton 100HN Tape
Type	Two-component epoxy	Double-sided tape Acrylate adhesive
Manufacturer / vendor	Loctite	CMC Klebetechnik
Curing time	24 h at +25 °C	—
Viscosity before curing in mPas	37000	—
CTE in $10^{-6}/\text{K}$	58	20
Thickness in $\mu\text{m}$	—	60
Radiation length in cm	Unknown	31.5
Radiation hardness	Sufficient	Sufficient

The Epo-Tek 301-2 glue, which is also used for gluing the sensors, can serve as a backup option for the high-viscosity Ablestik 45. While the lower viscosity allows for achieving thinner layers and hence a smaller overall material budget, it also provides a big risk during the assembly. This can be alleviated providing dedicated hatches in the carrier restricting the flow of the glue. This is discussed in chapter 4.1.

<sup>14</sup>This has been proven to not be an issue during vacuum cycling.

<sup>15</sup>These are the properties for the rigid version. Depending on the amount of hardener, a semi-rigid and a flexible version of the glue can also be mixed.

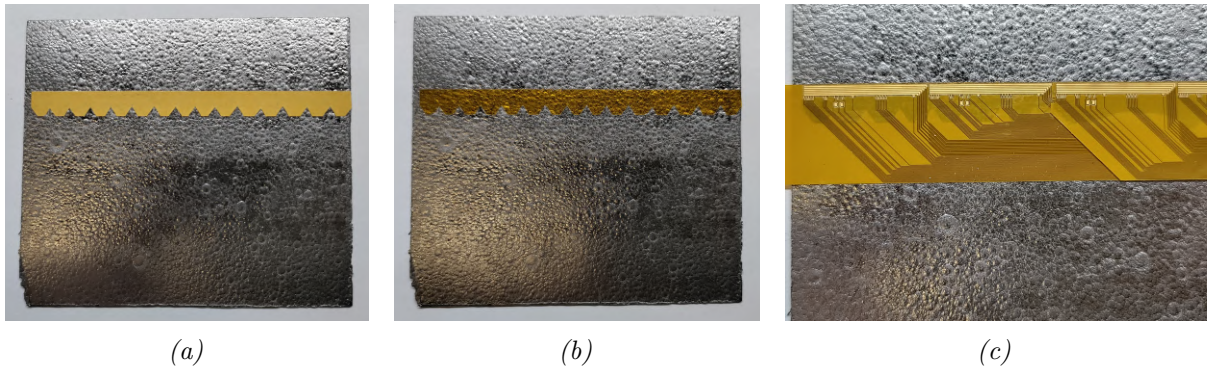


Figure 2.11: Double-sided kapton tape (top cover layer still attached) glued onto a sheet of polished TPG (a). The top cover layer is removed and the gluing can be visually inspected (b). A thin, partly single- / partly double-layer FPC is glued on top. The tape is still visible underneath the single-layer, allowing for an optical QA.

## Thread Sealant

Until now, the dedicated thread sealant Loctite 511 has been used to seal all threaded connections. It features excellent reworkability and its compatibility with Novec 649 has been proven over hundreds of temperature cycles and more than 2 years of constant wetting. The radiation hardness of this thread sealant is not known. To eliminate this single point of failure, the semi-rigid version of Loctite Ablestik 45 has been chosen as the thread sealant for all types of threaded connections, *e. g.* the in- and outlet fittings of the heat sinks and manifolds. Its compatibility with Novec 649 has been tested over several hundred temperature cycles but no concluding results can be presented yet. This is discussed in more detail in chapter 3.2. Unlike Loctite 511, Loctite Ablestik 45 is not thixotropic, but cures fully, so special care has to be taken when trying to rework the fragile connections at the heat sinks.

### 2.3.1 Proposed QA Procedure

To assess the quality of the liquid adhesives in use, a test sample from the same batch is always cured under identical temperature and humidity conditions. The parameters for the integration of the sensors have been optimized with dummies. A visual inspection of the sensor gluing is not possible. The quality assessment includes tests of the vacuum-compatibility (for the sensors and FPCs) and leak-tightness (for the thread sealants) after certain integration steps. This can only be confirmed after curing the glue.

The quality of the gluing of the FPCs with the double-sided tape can be inspected visually as both the tape and a single-layer FPC are see-through and trapped air bubbles can be spotted and removed.

### 2.3.2 Open Questions

Two open questions *w. r. t.* the adhesive selection and their use in the MVD remain which concern the CTE mismatch of the adhesive for the sensor and the logistics of plasma activation before gluing.

- CTE Mismatch Carrier / Adhesive / Sensor

It should be experimentally proven that the CTE mismatch between the carrier, the adhesive, and the sensor is not relevant in the operating range of the MVD using the EpoTek 301-2 epoxy cured at room temperature. For this, it could be tested whether deformations, cracks or peeling is observed with silicon dummies glued onto TPG during intense thermal cycling

between  $-25^{\circ}\text{C}$  and  $+25^{\circ}\text{C}$ . If, contrary to expectations, the CTE mismatch turns out to be a critical factor for the long-term stability of quadrants, an alternative low-viscosity, low-outgassing, radiation-hard and commercially available glue that also features high elasticity would need to be identified.

- Plasma Activation Lifetime and Logistics

During prototyping, the parylene coating of the carriers was done by the Fraunhofer Institute for Interfacial Engineering and Biotechnology (IGB). Additionally, an industrial partner performing parylene coating and plasma activation up to all MVD specifications has been identified. The lifetime of the activation level (a surface energy of  $68\text{ mN/m}$ ) has been measured to be 7 days. This is critically short, especially for the mass production, if it is done at an external company, when taking standard delivery times into account. Hence, the plasma activation should be decoupled from the coating and different options, using *e.g.* standalone desk-top plasma devices at the GSI or IKF laboratories, should be explored. It needs be ensured that the plasma does not etch the coating but activates it homogeneously. It should be evaluated to which extent the storage temperature and atmosphere can beneficially influence the lifetime of the plasma activated surface, possibly alleviating the time constraints in the integration introduced by it.

## 2.4 The Flexible Printed Circuits

The sensors have to be electrically connected inside the acceptance. This can be realized with low-mass FPCs produced in industrial standard processes. The sensors are connected row-by-row, routing all connections to the periphery. The FPC will combine all necessities of powering, programming, tuning, synchronizing, and reading out the sensors.

The form factor of the FPC inside the acceptance is mostly fixed as it is defined by the overlap of the active regions of front-side and back-side sensors. The form factor outside the acceptance is dictated by the connectors to be used. The FPCs should only be bent in one direction to minimize stress on the traces. The material budget of the FPCs has to be minimized for the part inside the acceptance. Outside the acceptance, where the connectors to the front-end electronics have to be soldered<sup>16</sup>, a stiffener is advised used to increase the mechanical stability.

It is intended to produce the FPCs in an industrial standard process, providing a low-risk and economical solution. It will be based on copper traces with flexible polyimide covers. The specifications will be similar to the low-mass FPC designed for PRESTO and the MIMOSA-26 sensor which was produced at ILFA GmbH, Hannover, Germany [44, 45]. The thickness of the layers of the PRESTO FPC is given in table 2.4.

Table 2.4: The different layers, the respective thickness and fill factor, and material budget of the low-mass PRESTO FPC designed for the MIMOSA-26 sensor [1].

Layer	$f \cdot d$ in $\mu\text{m}$	$x/x_0$ in %
Coverlay	$100\% \cdot 26$	0.009
Copper	$40\% \cdot 12$	0.009
Polyimide	$100\% \cdot 25$	0.009

A single-layer FPC will connect two adjacent sensors. Hence, one FPC is needed for one row of sensors for the stations of geometry  $b$ . For the larger stations of geometry  $c$ , a stack of two

<sup>16</sup>In the current conceptual design, SlimStack Board-to-Board instead of ZIF connectors are intended. The stable mechanical connection can ease the placement and alignment of the FPC.

single-layer FPCs would be needed. As an alternative, double-layer options should be explored<sup>17</sup>. The FPCs of the front- and back-side will be mirrored. Table 2.5 summarizes the most important properties of a low-mass MVD FPC as it could be realized by ILFA.

*Table 2.5: Properties of a low-mass MVD FPC according to the standard design rules by ILFA [46]. The feature size of  $100\mu\text{m}$  (single-ended) and  $300\mu\text{m}$  (differential; two single-ended lines plus additional space to avoid cross-talk) is slightly larger than the minimum realizable with ILFA ( $75\mu\text{m}$  [46]) and the low-mass MIMOSA-26 FPC designed at IKF ( $80\mu\text{m}$  [1]), and might still have to be optimized. The width of the power traces is determined requiring an ohmic resistance of  $\sim 100\text{m}\Omega$  for a  $10\text{cm}$  long trace of  $12\mu\text{m}$  copper. The width of the GND is double that of the power traces.*

Property	Detail	Value
Maximum FPC width in mm <sup>18</sup>	—	23
Total height in $\mu\text{m}$	Single-layer	65
	Double-layer	100
Trace height in $\mu\text{m}$	—	12
Trace width in mm	Single-ended	0.2
	Differential pair	0.6
	Power	1.5
	GND	3.0
Material budget $\%_{x_0}$ in $\%$ <sup>19</sup>	Single-layer	0.051
	Double-layer	0.093
Bending radius (dynamical) in mm	Single-layer	0.7
	Double-layer	1.0

Not all of the possible lines of the sensor can be routed on the cable due to the tight width constraints of less than 23 mm. The current understanding of the minimal amount of traces to power, program, tune, synchronize, and read out the sensors is summarized in table 2.6.

The hit rate limits are the key factor in determining the number of necessary data links on the FPCs. The hit rate limits for the possible number of active data links are [47]:

1 link: 20 hits/frame

2 links: 55 hits/frame

4 links: 190 hits/frame

8 links: 460 hits/frame

The number of necessary data links for the individual sensors in the detector depends on their occupancy, and therefore on their placement in the detector, the collision system, and the strength of the magnetic field. The occupancy of every sensor has been simulated. The results have been published in a Technical Note [47]. In the end, the number of active outputs defines the total width of the FPC, the maximum occupancy of the detector, and hence the maximum interaction

<sup>17</sup>For the PRESTO assembly, two single-layer FPCs were glued on top of each other to connect three sensors in a row. This stack can however feature a worse relative alignment and overall material budget than an actual double-layer FPC while also risking an insufficient vacuum-compatibility.

<sup>18</sup>Reserving this much space for the FPC of the row of sensors closest to the heat sink translates to a larger carrier size for geometry  $b$  and  $c$  than stated in the TDR. The values can be found in table 2.1.

<sup>19</sup>This value is calculated using a fill factor of the traces of 40%.

rate which the MVD can handle. The values should be carefully reiterated to optimize the MVD for maximum occupancy in TR geometry<sup>20</sup>.

*Table 2.6: The current understanding of the necessary number of traces on the FPC and their contribution to the total width of the FPC serving two sensors based on the feature size stated in table 2.5.*

Line	Type	# / Sensor	Width / FPC in mm
Power (A & D)	Power	2	6.0
Top / back bias	Single-ended	2	0.8
GND	GND	2	6.0
Data	Differential	2–8	2.4–9.6
Clock	Differential	1	1.2
I <sup>2</sup> C	Single-ended	2	0.8
Start	Differential	1	1.2
Reset	Single-ended	1	0.4
VMON & IMON	Single-ended	2	0.8

The total width of the FPC is then between 19.6 mm and 26.8 mm, depending on the number of data links. The maximum width allowed by the space constraints on the carrier is 23 mm. At the time of this thesis, the following number of links is intended:

Geometry *b*: 4 data links for all sensors

Geometry *c*: 2 data links for all sensors

As one FPC (layer) will serve two sensors, each layer of the FPCs of geometry *b* and *c* will have the same layout, except for the total length and, possibly, the number of data links<sup>21</sup>.

The FPC will be designed in several iterations, focusing first on the functionality, optimizing the layout, the necessary amount of traces, and the placement of power filtering elements. Afterwards, the feature size can be minimized to arrive at the final form factor, optimizing the material budget, the resistance of the power/GND lines, and the signal quality of the fast lines. The starting point will be the low-mass FPC designed for the MIMOSA-26 sensor during MVD prototyping which is shown in figure 2.12.



*Figure 2.12: Double-layer FPC for 4 MIMOSA-26 assembled from two single-layer FPCs.*

The open questions presented at the end of this chapter need to be addressed urgently to start with the design. The FPC is, together with the front-end board, one of the last two missing components to mechanically integrate a pre-production quadrant.

<sup>20</sup>In the studies presented in [47], the VX geometry of the detector was also considered where the total hit capability was limited by the occupancy of the most exposed sensors which are intended to run on all eight data links.

<sup>21</sup>Using the same layout for all FPCs introduces redundant data lines in the downstream stations, but can save on offset and production costs.

### 2.4.1 Proposed QA Procedure

The quality of the FPCs will be assessed by an optical inspection. The critical points are the electrical connections, *i. e.* the bonding pads which should be free from scratches and material remains that could hamper the bonding, and the FEB connectors which should be positioned and aligned correctly. Additionally, the manufacturer will perform an electrical inspection, measuring the resistance of the traces and comparing them to their nominal values.

### 2.4.2 Open Questions

A multitude of questions *w. r. t.* the layout, design, validation, and optimization of the FPC are still open at the time of this thesis.

- Number of Traces

The first input to start laying out the FPC is the necessary amount of traces. This includes all the necessities to power, program, tune, synchronize, and read out two sensors. Tests of the start / synchronization / reset operation are work in progress. The aim is to prove the feasibility of synchronization over I<sup>2</sup>C instead of the dedicated sync pads on the sensor to save on a differential line pair per sensor on the FPC. The number of data links per sensor needs to be reiterated to maximize the overall occupancy under the constraint of the total width of the cable. It needs to be determined whether, additionally to VMON and IMON<sup>22</sup>, any of the monitoring pads for temperatures and power should be routed. As of now, it is not intended to route any of the data and sequencer markers, anything related to the analog output of the pixels, or any of the analog injection pads for the steering voltages. Ideally, no pad on the sensor is left floating. The optimal bonding configuration for all the unrouted pads has to be determined experimentally.

- Sharing of Lines

The feasibility of sharing lines between two sensors needs to be studied. This will most likely be limited to the GND and /or the biasing traces. A shared GND on the FPC can be beneficial to stabilize the GND for the innermost sensor which is subject to higher occupancy and hence current fluctuations than the adjacent sensor. This will not decrease the overall width of the cable. A sharing of the high-ohmic top- and back-biasing traces can save the width of two traces per two sensors. A sharing of any of the other traces is prohibited by the bonding scheme when opting for a single-layer FPC as lines can not cross each other. Lines can be crossed in a double-layer FPC which allows for the sharing of lines. However, this comes at the cost of a local increase in the material budget from the via connecting the traces on the two layers (a cylindrical copper via with a thickness  $\sim 50\ \mu\text{m}$  and a diameter of  $\sim 100\ \mu\text{m}$ ). It should be evaluated if a separation of the analog and digital GND can be beneficial.

- Feature Size

Next, the feature size of all lines needs to be determined, optimizing also the power and GND traces. This includes balancing the ohmic resistance and voltage drops with the material budget and tight width constraint of 23 mm.

- Partly Double-layer FPC

The option of a partly double-layer FPC should be explored for the FPCs for geometry *c*. This would save the difficult process of merging two fragile FPCs together and is also beneficial for the overall material budget of the FPC. Should a partly double-layer FPC not

---

<sup>22</sup>These are the configurable outputs for the voltage and current DACs that are necessary for tuning the detection threshold.

be feasible, it is recommended to connect the two single-layer FPCs with a double-sided Kapton tape rather than a liquid glue. This will simplify the merging process and keep the reworkability of the connection.

- Additional Design Constraints

It should be evaluated to which extent the bonding process on the top layer of a double-layer FPC can introduce damage to the traces of the bottom layer. If this is significant, it would be beneficial to not route the traces of the bottom layer directly beneath the bonding pads of the top layer, posing a keep-out area for the traces on the bottom layer

- Pre-bent FPCs

Pre-bending options of the FPCs should be explored in order to remove any static tension on the components at the step from the carrier to the FEB.

- MIMOSIS Performance with FPC

As already described in chapter 2.1, the performance of MIMOSIS sensors powered with FEAST DC/DC converters, and programmed, tuned, synchronized, and read out with long, unshielded FPCs has to be measured as part of the electrical integration of the detector. These studies can already be concluded with the available MIMOSIS-1 sensors at the IKF laboratories. This could also include a field study in a more realistic environment, *s. a.* the mCBM setup at SIS 18 at GSI.

- Overall Material Budget of the FPC

Compared to copper, aluminum has a lower electrical conductivity (factor of 1.7), but a substantially longer radiation length (factor of 6.2) [1]. A change from copper traces to aluminum traces with equal electrical resistance equals a reduction of the FPC's material budget  $\%x_0$  by  $\sim 0.024\%$  to reduce multiple scattering. The contact with the company (LTU Enterprise, Kharkiv, Ukraine [48]) producing ultra-low-mass Al FPC, *s. a.* the CBM STS microcables, has already been established. The gain in material budget has to be traded against a possibly worse integration yield, as these FPCs are extremely fragile and, due to a quite sizeable step from the carrier to the front-end electronics, have to be bent. FPC options with Al traces can be explored at a later stage of the project, once a dedicated standard FPC has been consolidated. A lot of challenges may arise when changing from copper traces to aluminum traces. Unlike the STS microcables, an MVD FPC needs to have some very wide traces for powering which can be difficult to produce in Al. Also, the electrical connection to the sensors and the front-end electronics needs to be done by tape-automated bonding and soldering, instead of wire-bonding and a connector. This adds risk during the assembly and calls for expertise which is currently not available at the IKF. Calling for this option is not advised for a first-day MVD, but should be explored for *e. g.* upgrades.

## 2.5 The Front-End Electronics

The Front-End Board (FEB) is the first stage of the front-end electronics. It features connectors connecting the sensor FPCs, the power input from the FEAST DC/DC converters, and the ReadOut Boards (ROBs) upstream. It also contains passive components for power filtering as well as GBT-SCA chips for sensor control and monitoring. For the small stations of geometry  $b$ , one SCA chip will serve one side of a half-station. For the larger stations of geometry  $c$ , one SCA chip will serve one side of a quadrant. This yields a total of 24 SCA-chips for the MVD.

The FEBs will be screwed onto the heat sinks which serve as the mechanical support of the boards and their cold plate. Their form factor is mostly defined by the form factor of the heat sinks.

For the small stations of geometry *b*, a C-shaped FEB is intended which serves the front- / back-side of a half-station. For the larger stations of geometry *c*, it has to be evaluated if a C-shape (form factor: half-station) or if an L-shape (form factor: heat sink, with an interconnection between two quadrants) is more beneficial. An electrically insulating but notable thermal contact between the FEBs and the heat sinks *e. g.* can be achieved with a Kapton MT foil [49]. For every station size, there will be a version for the front- and back-side.

The placement of the components on the FEBs is defined by the mechanical constraints: The sensor FPC connectors have to be placed in line with the sensor rows<sup>23</sup>, the ROB FPC connectors should be routed to the sides of the detector and should be on the same level as the ROBs on the front flange to prevent twisting of the FPCs. Each one of the 3 GBTx-chips on a ROB connects 10 data links from the sensors. The number of active data links per quadrant needs to be determined soon to define the number and placement of connectors on the FEBs. This will also determine the number and placement of the ROBs<sup>24</sup>. All connectors should be placed such that the coolant connectors are still accessible.

A version of the FEB optimized for the integration and characterization needs to be designed and tested. It should feature the identical placement of sensor FPC connectors to ease the placement of the FPCs but has no harsh constraints on the form factor. During the assembly of the quadrants, the C-shaped FEBs could be avoided with a dedicated integration FEB. This way, the mechanical integration and QA of single quadrants could be decoupled from the integration of the two quadrants into a half-station. The readout of the sensors with this board could be based on the TRB readout to perform the functionality tests of the quadrants with the same setup as the probe testing beforehand.

There is no design of the FEBs yet, neither mechanical nor electrical. Before starting the design of the board, the requirements by the sensors have to be specified to define the necessary components. This includes also a validated FPC which can be expected by 2025. The mechanical layout, *i. e.* the placement of the SMD components on the board, can then be optimized in the CAD model to afterwards electrically layout the board. In the latest CAD model of the detector, placeholders with the same form factor as the heat sinks and a thickness of 2.5 mm are used.

The communication and DAQ with SCA- and GBTx-chips of MIMOSIS sensors is work in progress as a step towards a CBM compatible DAQ and a first iteration of the FEB.

## 2.6 The Heat Sinks

The actively cooled heat sinks evacuate the heat from the sensors and front-end boards (FEBs), and also serve as the mechanical frame of the detector. The assembled carriers sit on a balcony on the heat sink and are fixed with a screwed clamp. The cooling channels in the heat sinks are optimized for mono-phase, low-viscosity liquid cooling with small pressure drops. To efficiently guide the heat to the coolant, the cooling channel reaches directly underneath the balcony (see figure 2.13a), minimizing the heat conduction path in the bulk aluminum. The heat sinks have been modified from version 2.5 (see *e. g.* [1]) and several features have been added in the latest versions 3 a and 3 b, finalizing the design.

The form factor is constrained by the placement of services, by the size of the beamhole, the carriers and the front-end boards, and by the overall detector keep-in volumes. The design has been optimized with engineers at GSI and the manufacturer, CTX. The heat sinks with the smaller form factor of geometry *b* have been designed in similar fashion to the updated heat sinks of geometry *c*. Geometry *a* is not needed for the baseline detector setup (TR geometry).

<sup>23</sup>Using SlimStack Board-to-Board connectors mechanically fixes the sensor FPC which eases its placement and alignment.

<sup>24</sup>With the current, non-optimized number of data links, 704 links spread over 84 GBTx-chips, *i. e.* 28 ROBs would be necessary.

The reiterated form factors of the carriers can be found in table 2.1. The radii of the beamhole have been taken from the TDR (geometry *b*: 5.4 cm, geometry *c*: 10.4 cm [1]). The active part of the detector has a fourfold rotational symmetry. The services of the detector, *i. e.* cooling, powering and data, break this symmetry as they are routed to the left and right of the detector. Hence, two versions of heat sinks exist per geometry *b* and *c* with mirrored versions of cooling channels inside. Exemplarily for all new heat sink designs, version 3a of geometry *c* is shown in figure 2.13.

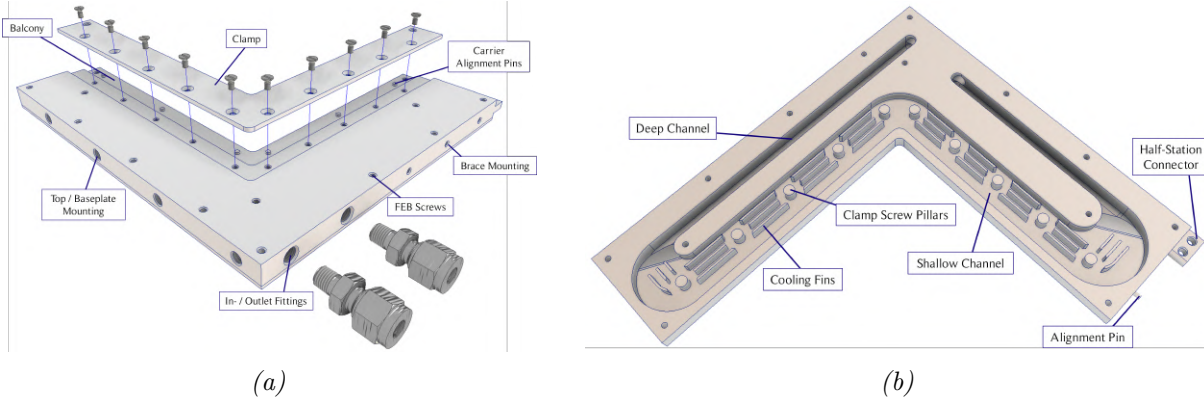


Figure 2.13: CAD view of the heat sink version 3a (geometry *c*), including the screwed clamp fixating the carrier that sits on the balcony, and the NPT in- and outlet fittings (a). Cross-sectional CAD view of the cooling channel of the heat sink version 3a (geometry *c*), including the vacuum-brazed cover plate (b).

Fins have been placed in the wide part of the cooling channel to improve the heat transfer between heat sink and coolant and to improve the mechanical stability of the heat sink. The heat sinks are produced in Al6063<sup>25</sup> with a CNC-milled cooling channel that is closed in a vacuum brazing process. Unlike in version 2.5, the covering plate does not cover only the channel, but the whole workpiece. This ensures a flatness of at least 150  $\mu\text{m}$  and no deformations up to pressures of 10 bars. This comes at an increase of the overall thickness of the heat sinks from 10 mm to 12 mm. The space in between the detector stations is large enough to accommodate this.

The connector mounting two heat sinks together to a half-station has been improved for better mechanical stability against stress along the *z*-axis and ease of manufacturing. An alignment pin and a brace that can additionally be screwed from the sides into the half-stations ensure a stable and planar C-shape of the half-stations. Half-stations can be mounted with screws from the top and bottom to the top and base plate, respectively, to form half-detectors. The relative alignment of the half-detectors will be ensured by alignment pins placed on the top and base plate rather than the heat sinks. This will ensure that any potential mechanical stress is absorbed by the robust mounting structure and not by the delicate quadrants.

The metric fittings previously used have been changed to NPT fittings due to their excellent commercial availability and larger inner openings. Copper gaskets have been excluded due to their bad compatibility with aluminum, see chapter 3.5. Instead, a thread sealant can be used, in this case the semi-rigid version of Loctite Ablestik 45.

The heat sinks feature screw holes of different metric sizes to fix the clamp and the front-end electronics on the heat sinks, to fix the connector between to quadrants and the brace of the half-stations, and to fix the half-stations themselves to the top and base plates. Pins have been placed on the balcony to align and fixate the carrier in its nominal position. The space on the balcony reserved for the carrier is deliberately larger than the carrier by 100  $\mu\text{m}$  on one side to prevent collisions of the fragile carriers and sensors of adjacent quadrants.

<sup>25</sup>This alloy features a good rigidity and thermal conductivity and can be vacuum-brazed.

Two heat sinks of the latest generation, version 3 a and b of geometry *c*, have been produced, see figure 2.14. As of now, only a visual inspection and metrology has been performed. A detailed inspection of the thermal performance is work in progress.

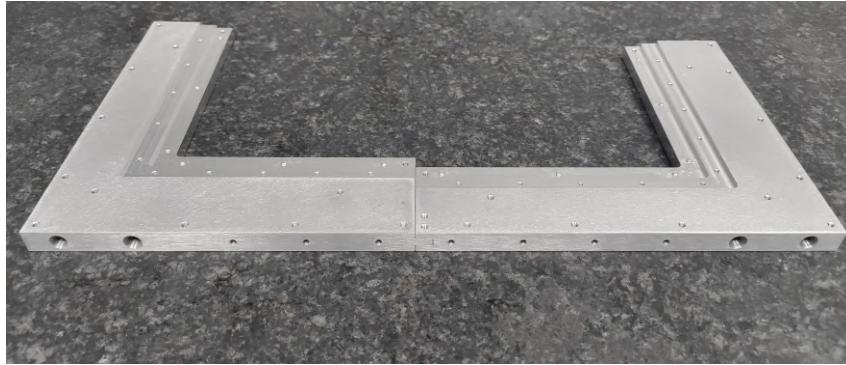


Figure 2.14: Half-station (geometry *c*) assembled from two heat sinks of the latest version 3 a and b. The deviations from perfect flatness are smaller than 0.05 mm and not visible on the planar marble table.

All dimensions are well in the tolerances of 0.1 mm. A C-shaped half-station can easily be assembled from the quadrants and features only marginal clearance. Most crucial for the use in the MVD is the C-shape of the assembly which must not deform under its own weight. This value should be measured precisely as this defines the safety margins of the carrier dimensions. Also, the deviations from perfect flatness of the assembly should be marginal to minimize the static stress on the carriers. The flatness of the heat sinks has been measured to be 30  $\mu\text{m}$  for version 3 a and 50  $\mu\text{m}$  which is significantly better than the required 150  $\mu\text{m}$ .

The design of the heat sinks is very far progressed and only minor modifications, if any, in the design *s. a.* the placement of screw holes are expected.

### 2.6.1 Proposed QA Procedure

The quality assessment of the heat sinks includes metrology and a leakage test:

#### 1. Metrology

The outer dimensions and the planarity of the heat sinks have to be measured to ensure they are up to the specifications including the tolerances defined in the technical drawings (better than 0.2 mm for all values) [50]. This can be done *e. g.* with a caliper gauge (precision of 0.05 mm).

#### 2. Leakage Test

The in- and outlet fittings have to be screwed into the heat sinks and a leakage test including  $\sim 50$  temperature cycles should be performed<sup>26</sup>. If Novec 649 is selected as the coolant, the temperature cycles should range between  $-25^\circ\text{C}$  and  $+25^\circ\text{C}$ . Alternatively, if glycol/water is selected as the coolant, the temperature cycles should range between  $-10^\circ\text{C}$  and  $+25^\circ\text{C}$ . The discussion on the choice of coolant can be found in chapter 3.5. Leaks can be spotted with a leak detector optimized for coolants, *s. a.* the testo 316-4 with an R134a sensor [51]. The pressure drops and the average flow can be measured to spot significant production flaws in the channel. This can all be done at the MVD cooling test stand at IKF. Acceptable values and limits can only be defined after sufficiently testing the latest of version heat sinks and validating their thermal performance. For the prototype heat sinks (version 2.5), results have been published in a technical note [52]. Similar values are expected for version 3a and b.

<sup>26</sup>This takes less than 2 days and can be mostly automatized.

## 3 Detector Integration

This chapter introduces the different hardware components used for the mechanical and electrical integration of the detector. This includes the top plates hosting the FEAST DC/DC converters, the coolant manifolds, the detector mounting structure including the electrical interfaces, the MVD cooling system, and the detector controls system. The important aspects regarding the mechanical integration, the proposed QA procedure, and open questions are presented. The detector integration is not as far progressed as the sensor integration. The components are far from the design freeze and therefore mostly concepts and ideas are presented rather than final form factors and tolerances. It is recommended to build a full-size mechanical mock-up system of the detector to evaluate and optimize the design of the structural frame of the detector.

### 3.1 The Top Plates

The top plates of the MVD are part of the mechanical frame of the detector, connecting half-stations to half-detectors at the top. Additionally, they serve as the return manifold for the coolant of the heat sinks and as the mechanical support and cold plates for the FEAST DC/DC converters that power the sensors. The sensors and FEBs take up only a fraction of the cooling capacity of the mono-phase liquid cooling. The power entry of the FEAST DC/DC converters can easily be cooled away with the same cooling system, also in vacuum.

Placing FEAST DC/DC converters inside the MVD box instead of outside is beneficial for several reasons:

- The placement in the vacuum allows for shorter supply cables between the converters and the sensors which results in smaller voltage drops and less noise pickup over the cables.
- It minimizes the number of electrical feedthroughs on the front flange<sup>1</sup>
- It efficiently uses the space available on the top of the detector.

The FEAST DC/DC converters will be mounted upright on a PCB which sits on a dedicated cooling fin<sup>2</sup>. The fins are screwed on top of the top plates. They have the identical profile as the cooling fins of the STS power stacks, only differing in length and the placement of screw holes. The coolant flows directly underneath the fins to optimize the heat exchange. If necessary, the thermal interface between the FEAST DC/DC converters and the cooling fins, and the cooling fins and the top plates, can be improved using a thermal interface material *s. a.* PGS. The assembly is shown in figure 3.1a.

Two versions of the top plates have been designed: a small one connecting the half-stations of geometry *b*, and a large one connecting the half-stations of geometry *c*. The top plates are screwed vertically into the half-stations. These screws are accessible, even after mounting the FEAST DC/DC converters on top. Due to the different form factors of the quadrants of geometry *b* and *c*, the small and large top plates are positioned on different levels and can be interconnected. An interconnection with a triangular crossbar construction can help minimize the shear stress on the half-detectors and significantly improve the rigidity of the detector mounting structure. This is shown in figure 3.1b.

---

<sup>1</sup>The space upstream of the MVD around the front flange is extremely limited due to the target exchange device, and the highly dense routing of all the services of the MVD and STS.

<sup>2</sup>The actual ASIC is mounted on a thermal via which is directly connected to the cooling fin.

The design of the top plates allows for use of the same design for the left and right half-detector, without mirrored versions. The top plates are, similar to the coolant manifolds, easy to manufacture with CNC-milling and -drilling from a 12 mm thick aluminum block. 3 parallel holes are drilled into the side of the short top plate (5 holes for the long top plate), serving as the in- and outlets. A perpendicular drilling from the back-side connects the in- and outlets. The hole from the interconnection is closed with an endcap fitting<sup>3</sup>, see figure 3.1a. This design can produce a cooling channel without employing elaborate processes *s. a.* friction stir welding or vacuum brazing while also keeping small tolerances on the outer dimensions. 1/4 " NPT fittings for 1/4 " SS 316 Swagelok piping are used. On the side where the half-stations are touching, recesses are placed where the crossbars are mounted. Additionally, alignment pins to guarantee the relative alignment of the half-detectors after beam tuning can and should be placed there.

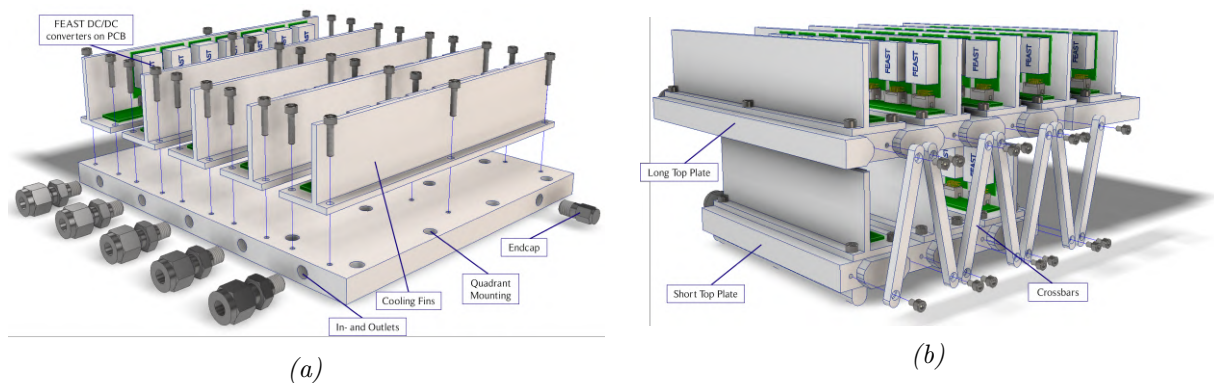


Figure 3.1: Assembly of a large top plate with the fittings and the FEAST DC/DC converters, including their cooling fins (a). Assembly of the top plates for a half-detector, including crossbars to strengthen the assembly against shear forces (b).

### 3.1.1 Proposed QA Procedure

The quality assessment of the top plates is similar to the QA of the heat sinks (see chapter 2.6.1 and includes metrology and a leakage test.

#### 1. Metrology

The outer dimensions and the planarity of the top plates have to be measured to ensure they are up to the specifications including the tolerances which are expected to be better than 0.1 mm for all values. This can be done *e. g.* with a caliper gauge (precision: 0.05 mm).

#### 2. Leakage Test

The same tools and test procedures as for the heat sinks will be used for the leakage test of the top plates.

### 3.1.2 Open Questions

The mechanical design of the top plates has to be finalized. The design of the top plates is closely linked to the electrical integration of the detector. There is space for 94 FEAST DC/DC converters in the current design. If this number does not match the requirements of the MVD powering concept, the design will have to be adjusted accordingly, possibly modifying the form factors, the placement of screws, and the crossbar construction<sup>4</sup>. Analog and digital voltage will be provided

<sup>3</sup>This fitting does not collide with anything and does not extend into any keep-out volumes. It can also serve as a vent fitting, in case the whole MVD has to be drained.

<sup>4</sup>The MVD powering system still has to be designed and tested.

separately. Due to space constraints and economical reasons there will not be  $\sim 600$  DC/DC converters to supply each sensor individually, but they have to be grouped. The number of sensors in a group and the shape of the grouping needs to be optimized, taking the vastly different power consumption of the analog and digital power and also possible failures of single sensors in a group into account. Groups of sensors can be turned off with an en-/disable pin on the FEAST DC/DC converter. It has to be evaluated whether it is feasible to turn off single sensors<sup>5</sup>. A dedicated latch-up protection system needs to be designed as part of the powering and biasing system. A power filtering concept running in the strong magnetic field and under varying current needs to be worked out. The supply of the top- and back-bias needs to be worked out independently as those voltages can not be provided by FEAST DC/DC converters due to their magnitude and polarity, respectively. It has to be determined experimentally if they need to be switchable together with the supply voltage of the sensors to prevent damage.

## 3.2 The Coolant Manifolds

The MVD will employ several manifolds distributing the coolant from the chiller to the quadrants and back. The placement and design is dictated by the available space and the mobility of the half-detectors and the piping.

All piping from the quadrants is routed upstream *w. r. t.* to the stations towards the front flange. The half-detectors have to be moveable by 50 mm away from the beam axis. The services, including the piping, have to be able to accommodate for this movement. This is possible with flexible piping or hosing. To ensure the material compatibility with the coolant, stainless steel corrugated hoses which are rather inflexible should be used instead of more flexible options *s. a.* PVC or silicone hoses. Material compatibility is discussed in more detail in chapter 3.5. Due to space constraints and to achieve the highest possible mobility of the half-detectors, only two flexible hoses should be used per half-detector (one in- and one outlet). Hence, the distribution manifolds have to be placed inside the target chamber and are moving together with the half-detectors. The manifolds can be mounted to the respective baseplates that move with the half-detectors. The manifolds need to be mechanically stable to take up any tension in the hoses during movement of the half-detectors. This will minimize the load on the remote positioning system, allow for larger tolerances in the piping, and minimize the space occupied by hoses in the target chamber. The manifolds have to be mounted such that the in- and outlet fittings are horizontal. They should be placed underneath the baseplate. This allows for full access to the stations from the side and even for removing/replacing single half-stations, if necessary, without removing all the piping.

The tight space constraints in the target chamber prohibit the placement of valves, so a regulation of the flow for individual quadrants or half-stations is not possible. A very simplistic approach to the design of the manifolds is proposed that can easily be custom-made with only CNC-drilling either in aluminum or, if it needs to be more rigid, stainless steel.

Two manifold demonstrators have been produced, one at the GSI workshop and one in an industrial workshop by Facturee [53]. The manifolds are produced from Al6063 and each employ one inlet ( $\frac{1}{2}$  " NPT) and ten outlets (five  $\frac{1}{4}$  " NPT and five  $\frac{1}{16}$  " NPT). The outlets of the manifold have been shorted using  $\frac{1}{4}$  " SS 316 Swagelok piping. The threaded connections have been sealed using the semi-rigid formula of Loctite Ablestik 45 cured at room temperature<sup>6</sup> and have been tightened using the recommended torque on all fittings. The connecting pipes were measured, cut, and bent using simple hand tools. The precision of the bent pieces has been assessed using

<sup>5</sup>For permanently noisy sensors, it can be sufficient to mask individual pixels or to set a very high threshold to effectively shut them down. However, it can also be necessary to fully turn off single sensors in case of *e. g.* latch-ups.

<sup>6</sup>This adhesive can serve as a known-to-be radiation hard alternative to standard thread sealants *s. a.* Loctite 511.

a 3D-printed jig. The assembled manifold demonstrator is connected to the MVD cooling test stand at IKF which is running on Novec 649. Here, it can be used to demonstrate

1. The consistency and quality of the conical NPT threads with various sizes.
  - ⇒ The threads on the industrial piece were all uniform and of high quality.
2. The leak-tightness of NPT fittings of various sizes with Loctite Ablestik 45 as thread sealant over several hundreds of temperature cycles between  $-25^{\circ}\text{C}$  and  $+25^{\circ}\text{C}$ .
  - ⇒ No leaks have been spotted with a dedicated leak detection device. The level indicator of the chiller, however, showed a significant drop over a short period of time which should have been detected easily. The reason for this might be an issue of the level indicator rather than an actual leak which could not be confirmed yet. Therefore, Loctite Ablestik 45 could not be conclusively approved or disapproved as a thread sealant for the MVD.
3. The compatibility of Loctite Ablestik 45 with Novec 649.
  - ⇒ No compatibility issues have been observed.
4. The reworkability of threaded connections tightened with Loctite Ablestik 45.
  - ⇒ Reworking is possible, but the breakaway torque is much larger than for dedicated thread sealants, so special care needs to be taken at fragile connections.
5. The consistency and quality of the piping that is cut and bent with hand tools.
  - ⇒ It is possible to manufacture advanced piping shapes bent in several places with the necessary precision using hand tools only. However, for more complex piping, as the MVD will employ, CNC pipe bending is recommended.
6. The feasibility of using 3D-printed reference jigs to assess the quality of the piping before assembly.
  - ⇒ 3D-printed jigs can be useful references to verify the shape, lengths and (relative) angles of complex piping.

The demonstrator is a proof of concept towards the final manifold design. Threads to mount the manifolds to the baseplate need to be added and the placement and amount of inlets and outlets need some modification for the final manifold.

### 3.2.1 Proposed QA Procedure

After a visual inspection, the quality of the manifolds is assessed with a leakage test. The same tools and test procedures as for the heat sinks will be used for the leakage test of manifolds.

### 3.2.2 Open Questions

The design of the manifolds needs to be finalized. The final layout of the piping is a necessary input for that. The design is also coupled to the design of the baseplate and master table, defining the placement and mounting of the manifolds.

The total number of fittings in the MVD should be minimal, *i. e.* limited to the NPT threaded in- and outlet fittings. The manifolds and heat sinks should be connected by bent pipes instead of straight pipes with angled fittings. This reduces the number of single points of failure in the system and is using up the least amount of space. This comes at the cost of in parts complex shaped piping. Several bends in different planes are necessary for some pipes. The producibility of such pipes by hand with high precision is very low, so CNC pipe bending needs to be explored. The bending shapes, pipe lengths, and profiles can be optimized in the CAD model and afterwards directly exported as .stp files to import them into CNC pipe bending machines.

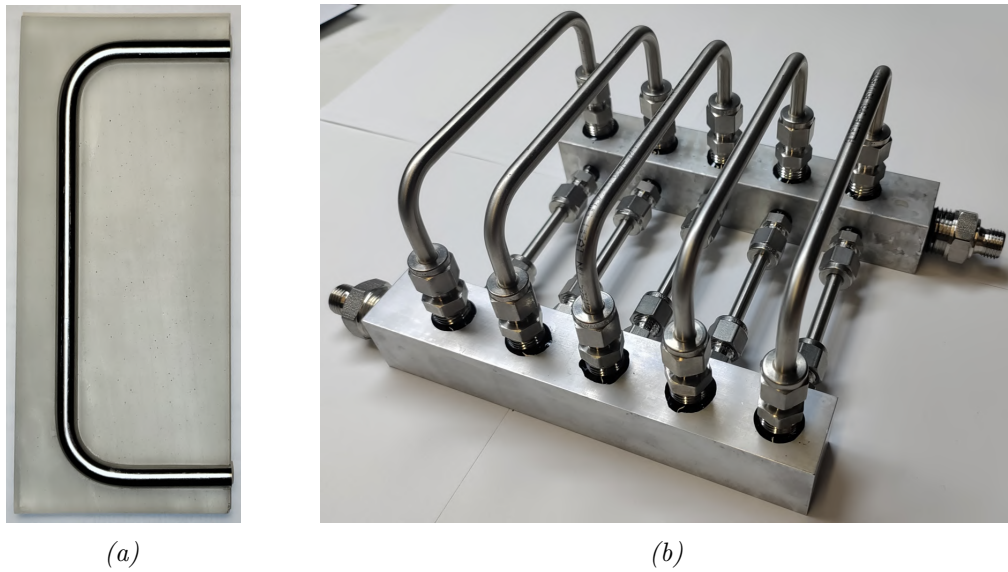


Figure 3.2: Pipe inside a 3D-printed jig to confirm the bend and cut (a). Assembly from two shorted manifolds with 22 threads to confirm the compatibility of semi-rigid version of Loctite Ablestik 45 as the thread sealant with Novec 649 (b).

### 3.3 Detector Mounting

The detector mounting structure consists of two parts: The front flange, featuring all the necessary feedthrough flanges, and the master table, featuring the remote positioning system and the baseplate. Figure 3.3a shows the current layout of the front flange and figure 3.3b shows the conceptual idea of the master table.

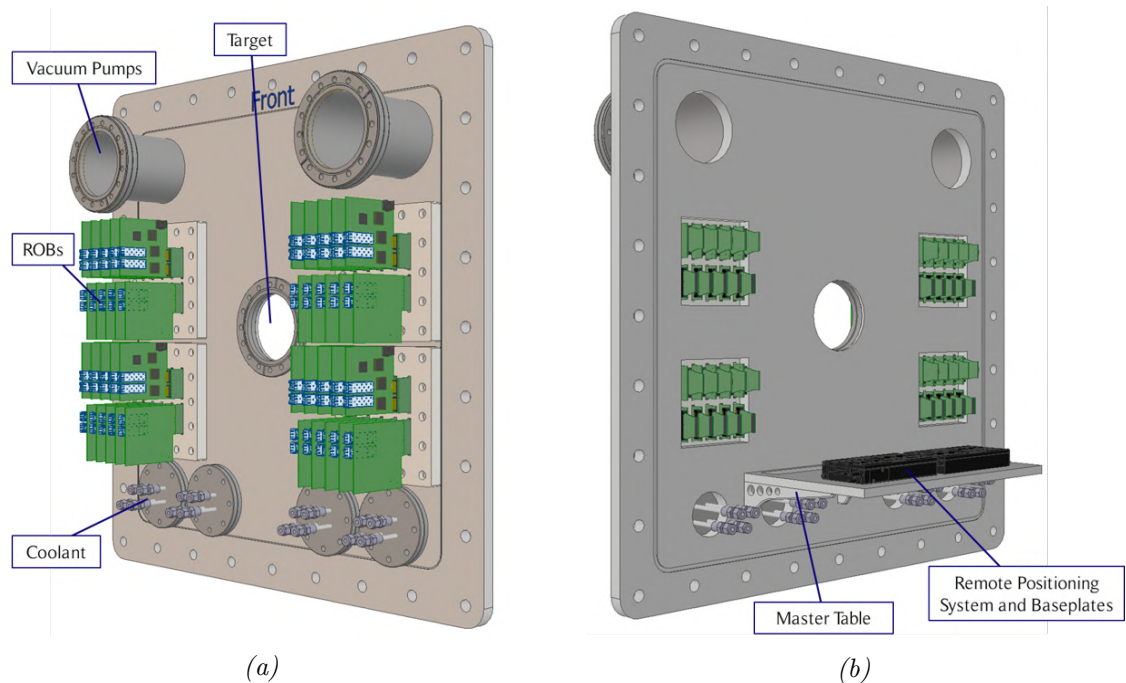


Figure 3.3: CAD view of the current layout of the service feedthroughs on the MVD front flange (a). CAD view of the conceptual idea of the MVD master table mounted to the front flange including a dummy remote positioning system for the detector (b).

## The Front Flange

The front flange is a  $800 \times 800 \times 20 \text{ mm}^3$  plate of stainless steel which is mounted upright to the target chamber. It features a number of vacuum feedthrough flanges connecting the vacuum pumping and the target, and routing all the services towards and from the detector. The placement of the different flanges of the front flange is optimized to efficiently route the services inside the target chamber. The requirements on the vacuum *w. r. t.* purity and outgassing are not extremely harsh, as the intended pressure is only  $\sim 10^{-4}$  mbar. The necessary connections on the front flange are:

- Target Vacuum

One or two flanges connecting the pumps for the target vacuum are necessary. They can be placed on the top where there is no interference with any other components.

- Target Exchange Device

The target (and hence also the target exchange device) is placed in the center of the flange.

- Power Feedthrough

One feedthrough for the power is predicted. It should be placed at the top center of the front flange. This will ensure a short connection to the FEAST DC/DC converters sitting on the top plates. The feasibility of routing the top- and back-bias in the same feedthrough has to be evaluated. It also has to be evaluated whether industrial solutions are possible or whether the flange has to be custom-made.

- DAQ and Detector Controls

The DAQ and detector controls will be done on the ROBs. Those will be placed outside the vacuum chamber. Due to the large number and high density of readout channels, standard solutions are not feasible. A custom-made PCB-type feedthrough is in the development with successful prototypes. Passive feedthrough PCBs are glued into slits in the flange<sup>7</sup>. Either two (20 ROBs each) or four (10 ROBs each) assemblies are necessary. The ROBs have to be mounted vertically, left and right of the target flange, to directly connect the half-stations. FPCs connecting the ROBs with the half-stations have to be designed. The fiber cables of the ROBs have to be routed upstream.

- Coolant

One coolant feedthrough for each half-detector is necessary. They feature two 1/2 " (outer diameter) stainless steel pipes, one for the in- and one for outlet. Depending on the operation temperature of the MVD, a thermally insulated option may be necessary. The flanges will likely have to be custom-made to fit the space constraints. The flanges should be placed on the bottom of the front flange, positioned rather centrally. This allows for routing the hoses easily towards the manifolds underneath the master table and prevents possible condensation water from dripping onto electronics.

- Additional Necessities

Additional components on the front flange might be beneficial. A dedicated valve for controlled and slow venting of the target chamber can be helpful to reduce turbulence while venting, especially close to the fragile bonding wires. Also, having the option to flush the target chamber with nitrogen can be beneficial in order to minimize corrosion of the components during *e. g.* maintenance, when the target chamber has to be vented. Additionally, a feedthrough for the remote positioning system might be necessary, depending on the choice of technology.

---

<sup>7</sup>The large gaps are filled with Loctite Ablestik 45, smaller gaps can be filled with a lower viscosity glue *s. a.* Epo-Tek 301-2.

## The Master Table

The master table is the rigid, horizontal stainless steel structure that supports the MVD inside the target chamber. It is tightly mounted to the front flange. The remote positioning system of the MVD is sandwiched between the master table and the two baseplates. The baseplates of the half-detectors fix the half-stations and manifolds.

A reproducibility of the positioning of better than 50  $\mu\text{m}$  is envisioned which can be achieved with dedicated stops placed on the master table. The design of the remote positioning system has not started yet. There are several options for the choice of technology *s. a.* piezo motors or pneumatic solutions. The system has to function in a strong magnetic field, in the harsh radiation environment, has to be vacuum-compatible, and be able to carry a load of  $\mathcal{O}(10\text{kg})$ . Industrial solutions exist and should be explored. It might be necessary to design a custom solution, considering the price for off-the-shelf solutions and the tight space constraints.

### 3.3.1 Proposed QA Procedure

The design of the front flange and the master table is not close to final with mostly conceptual ideas implemented. The QA will mostly be confirming the placement of the components and performing a functionality test, *i. e.* checking the vacuum tightness of the flange, the functionality of the remote positioning system, and an electrical characterization of the ROB FPCs.

### 3.3.2 Open Questions

The design of the front flange needs to be finalized. It can be helpful to iterate the design with the CBM engineers. This includes also the FPCs connecting the ROBs to the half-stations. The design of the master table and the baseplate have to be finalized. The design of the remote positioning system should be started soon, at least to define a realistic keep-out volume in the CAD drawings, as these components do not fall into the direct responsibilities of the MVD team [54].

## 3.4 Detector Control System

The MVD will be equipped with a dedicated DCS. SCA chips placed on the FEBs and ROBs will provide the interface for controlling and monitoring everything on the half-stations. Supply currents and voltages should be monitored. Additionally, it is necessary to read out the current and voltage DACs with an ADC to tune the thresholds of the detector. If the sensors are not pre-conditioned, they will undergo a significant threshold shift during the runtime of the experiment and a re-characterization is necessary which would require a total of 576 radiation-hard ADC channels or radiation-hard multiplexers for threshold tuning alone. If the sensor are to be pre-conditioned, a pin-out for an add-on ADC board to tune the thresholds before and after every beamtime would be sufficient<sup>8</sup>. The total number of available ADC channels during the beamtime is determined by the number of SCA-chips (in total 24 chips on the FEBs with 31 ADC channels per chip, all available for monitoring purposes). Additionally, the status of the remote positioning system, the cooling system, and the vacuum need to be monitored. This includes the absolute position of the half-detectors, the in- and outlet pressure, temperature and flow of the coolant, and the pressure of the vacuum.

The components of the DCS have to be fully remotely controlled and the monitoring has to be compatible with the CBM DCS which is based on EPICS tools. An EPICS DCS was developed for the operation and validation of PRESTO in a TRB-based readout [55]. The system needs to be adapted and optimized for the MVD, operating with MIMOSIS sensors and SCA chips. This

<sup>8</sup>Due to the harsh radiation environment of the MVD, the first station has to be exchanged after every beamtime, so the MVD will anyhow be accessible before and after every beamtime.

should ideally be implemented already for the validation and operation of a pre-series quadrant. The final DCS can adopt many aspects from the prototype DCS.

## 3.5 The MVD Cooling System

### 3.5.1 Design Considerations

The vacuum-compatible detector cooling concept of the MVD is based on conductive cooling inside the acceptance using thermal high-performance materials, and mono-phase liquid cooling outside the acceptance. The operation temperature is determined by sensor technology and sensor performance to guarantee a proper signal-to-noise ratio and detection efficiency over the sensor lifetime. The TDR suggests a conservative operation temperature of  $\sim -20^\circ\text{C}$  for all sensors to reduce leakage currents and improve radiation hardness [1]. All laboratory tests with the first full scale prototype sensor MIMOSIS-1 were conducted at controlled room temperature. Even at these higher temperatures, the sensor fulfills all specifications *w. r. t.* radiation hardness, S/N-ratio and resolution. It is expected that the final sensor, MIMOSIS-3, will perform at least as well as MIMOSIS-1 under the harsh radiation conditions at controlled room temperature<sup>9</sup> [56]. This suggests a relaxation of the requirements on the overall operation temperature by approximately 35 K to below  $+15^\circ\text{C}$  for all sensors. An operation temperature close to room temperature is also desirable in order to reduce thermal stress on the components and to retain a high elasticity of the glue. The temperature difference over the largest carriers has been simulated and measured to be below 10 K at the maximum expected thermal load [52].

Due to the tight space constraints, the heat sinks have to be as thin as possible while still ensuring small pressure drops. The thickness must not exceed 15 mm to allow for 40 mm spacing of the detector stations. The latest version of the heat sinks is 12 mm thick and specified for static pressures of up to 10 bar by the manufacturer.

The total power dissipation of the MVD is the sum of the contributions by the sensors (up to  $288 \times (0.45 + 0.03)$  W (digital + analog)<sup>10</sup>, see also figure 2.5a), FEAST DC/DC converters (DC/DC converter plus sensors:  $288 \times 0.48$  W/0.75%, see also figure 2.5b) and SCA-chips ( $24 \times 0.1$  W [57]). Ohmic losses in the cables as well as the heating of the coolant due to friction in the piping can be neglected. Introducing an additional design safety factor of +20% yields a nominal cooling capacity of  $(165 + 56 + 3)$  W (sensors + DC/DC converters + SCA chips).

The cooling of the ROBs needs to be addressed separately. At the time of this thesis, convective cooling with (pre-chilled) air is intended and is hence not part of the MVD mono-phase liquid cooling setup. The operation temperature can be up to  $60^\circ\text{C}$  [58]. The nominal cooling capacity including a safety factor of +20% is  $(0.6 + 0.4 + 4.8 + 0.1 + 0.1)$  W (VTTx module + VTRx module + GBTx chips + SCA chips + LV connection) per ROB. This yields 168 W for a total of 28 ROBs<sup>11</sup>.

### 3.5.2 Choice of Coolant

#### Novac 649

The baseline coolant of choice is Novac 649<sup>12</sup> (3M) which has an outstandingly low viscosity in sub-zero temperatures while also featuring a very low global warming potential [59, 60]. Its most important properties are listed in table 3.1. Novac 649 is relatively easy to handle using stainless steel piping and compression (or VCR) fittings. Novac 649 will undergo a hydrolysis

<sup>9</sup>The analog part of the pixel is the bottleneck structure for this and it is already in the design freeze phase.

<sup>10</sup>This is an upper limit with a generous safety margin. Assumptions: All sensors in very high occupancy with 8 data links active, at EOL doses. The analog power lies between 23 mW (no load) and 30 mW (full load).

<sup>11</sup>This holds true for the current, non-optimized number of data links with 704 links spread over 84 GBTx-chips, *i. e.* 28 ROBs.

<sup>12</sup>This is a trademark name for perfluoro(2-methyl-3-pentanone) with  $> 99.9\%$  purity.

reaction with dissolved water producing perfluoropropionic acid (PFPrA) and heptafluoropropane (HFC-227ea). This reaction is in an equilibrium in a closed system and the corrosive effects of the acid are insignificant due to the bad solubility of water in Novec 649 ( $< 20$  ppm by weight) and the weakness of carboxylic acids. Corrosion only becomes relevant in a leaky system where water can enter from the outside. A detailed discussion of the properties of Novec 649 as well as its handling, material compatibility and safety can be found in a CERN Memo and references therein [61].

On December 20 2022, 3M announced its plans to completely exit Per- and polyFluoroAlkyl Substance (PFAS) manufacturing by the end of 2025 [62]. This is in line with a restriction proposal for around 10 000 PFASs published by the European Chemical Agency (ECHA), published on February 7 2023 [63]. An alternative supplier (Hangzhou Qiqi Import and Export Co. Ltd) for industrial quantities of perfluoro(2-methyl-3-pentanone) has been selected by the cooling engineers of the CBM STS and positively validated for purity  $> 99.9\%$  [64].

However, Novec 649 is not acknowledged as a coolant by ECHA and falls under the proposed PFAS ban<sup>13</sup> [65]. Hence, possible alternatives have to be studied. Alternative PFAS and chemicals with high GWP, such as Novec 7100, Freon or perfluorohexane should be avoided as well. It is also self-evident that a change in technology, e.g. to bi-phase  $\text{CO}_2$  Si-microchannel cooling, is practically impossible at this point of the project as this would require a complete redesign of the MVD.

## DI Water and Ethylene Glycol/Water

Deionized water with added ethylene glycol is an alternative mono-phase liquid coolant in line with the PFAS ban<sup>14</sup>. Glycol reduces the freezing temperature while increasing the viscosity. The mixing ratio has to be optimized according to the specifications of the system. Exemplarily the thermal properties of water and ethylene glycol/water (50/50, by weight) are given in table 3.1. Glycol/water is easy to handle, while also being cheap and easily available.

The bottleneck property of glycol/water is the comparably high viscosity which causes high pressure drops in small channels. This can be alleviated by increasing the coolant temperature to  $\sim 0^\circ\text{C}$  (inlet) and reducing the coolant flow. At the same load, the same temperature rise in the coolant as for Novec 649 can be achieved with a quarter to a half of the coolant's volume flow when switching from Novec 649 to water or glycol/water, respectively, due to their higher heat capacity. Hence, pressure drops can be kept at moderate values while keeping the same thermal performance, shifting only the absolute temperature. This has been experimentally verified in a comparison of glycol/water mixtures and perfluorohexane<sup>15</sup> in turbulent flow at  $-10^\circ\text{C}$  during the design of the first LHCb Inner Tracker [66]. A quantitative analysis of the pressure drops in turbulent flow and its dependencies on inlet temperature, glycol/water mixing ratio and volume flow for the MVD setup can be done using CFD simulation tools or experimentally, which is however beyond the scope of this thesis. The results could be used to precisely determine the optimal parameters of a (glycol/)water-based MVD cooling setup. For Novec 649, this has already been done experimentally and the results have been published in a CBM Technical Note [52].

The poor stability of their dielectric properties is a significant drawback of deionized water and glycol/water when compared to fluoroketones such as Novec 649. Even at low cooling temperatures, the electrical resistivity can be significantly decreased by solving ions in the water. Maintaining a high level of cleanliness is therefore very important. Aluminum is known to be

<sup>13</sup>A transition period of 18 months and a five-year exemption is included in the ban for coolants operating below  $-50^\circ\text{C}$  *s. a.* Novec 7100. This is, however, for this system not feasible due to material compatibility and thermal stresses induced by drastic temperature swings of  $\mathcal{O}(70\text{K})$ .

<sup>14</sup>The use of propylene glycol instead of ethylene glycol is not recommended for this application due to a higher flammability hazard.

<sup>15</sup>Perfluorohexane and Novec 649 have identical thermo-physical properties apart from a strikingly different GWP.

Table 3.1: Properties of Novec 649, deionized water and ethylene glycol/water (50/50, by weight). Values taken from [60, 67–69]. See table A.2 for the discussion on radiation hardness.

Property	T <sub>ref.</sub> in °C	Novec 649	DI water	Glycol/water
Liquid density in kg/m <sup>3</sup>	−30	1761.5	—	1104.6
	0	1674.4	999.9	1090.2
	+20	1616.3	998.2	1080.6
Thermal conductivity in W/m·K	−30	0.069	—	0.412
	0	0.063	0.560	0.405
	+20	0.060	0.598	0.402
Specific heat capacity in J/kg·K	−30	1085	—	3320
	0	1092	4217	3412
	+20	1100	4182	3473
Kinematic viscosity in 10 <sup>−6</sup> m <sup>2</sup> /s	−30	0.88	—	49.97
	0	0.52	1.79	9,51
	+20	0.40	1.00	4.51
Dynamic viscosity in 10 <sup>−3</sup> Pa·s	−30	1.55	—	55.20
	0	0.87	1.79	10.37
	+20	0.65	1.00	4.87
Freezing temperature in °C	—	−108	0	−37
Boiling temperature in °C	—	+49	+100	+106
Electrical resistivity in Ω·cm	—	> 10 <sup>12</sup>	> 10 <sup>5</sup>	> 10 <sup>5</sup>
Radiation hardness	—	Sufficient	Sufficient	Sufficient
GWP	—	1	0	0

galvanically corroded by copper in the presence of water, which acts as the corrosion liquid. This prohibits the use of copper gaskets as alternatives to thread sealants in the MVD<sup>16</sup> [70]. Material compatibility can become critical at higher temperatures as the solubility of ions strongly increases. Above 60 °C, deionized water will even corrode stainless steel [71]. Also, a high oxygen content and a pH far from 7 (neutral) will increase corrosion. The coolant velocity should always be between 0.5 and 2.0 l/min to minimize erosion [70]. The harsh radiation environment can enhance corrosion due to radiolysis effects which are, however, minor, see also A.6. All these effects can be controlled using ion-exchangers and recombiners, microporous membrane contactors and demineralisation filters [72].

### 3.5.3 Recommendation

The much more relaxed operation temperature for the sensors and the uncertainty *w. r. t.* the probable restrictions in the use of Novec 649 call for a change of the baseline coolant towards ethylene glycol/water.

It is strongly recommended to not change the coolant again once the system is in operation. This is to prevent any contamination which could produce harmful chemicals if they reacted with radicals produced by radiolysis in the strong radiation field, possibly corroding the detector from the inside. A very high level of cleanliness of the coolant is mandatory from the start and needs to be maintained throughout operation.

<sup>16</sup>There are no compatibility issues of aluminum and stainless steel with deionized water.

The coolant temperature at the heat sink inlets should be  $\gtrsim -10^\circ\text{C}$  to ensure a large safety margin for the sensors' operation temperature. This can easily be achieved with a thin ethylene glycol/water mixture (glycol content  $\lesssim 30\%$  by weight). This will be the safest option to deliver the cooling demands independently of the proposed PFAS ban.

The coolant pressure at the heat sink inlet should be  $\lesssim 4$  bar (with the vacuum pressure as zero-reference) to keep pressure drops small. This also ensures a large safety margin for the pressure rating of the heat sinks.

The coolant volume flow per heat sink does not need to be larger than  $\sim 0.5$  l/min due to the high heat capacity of glycol/water. This amounts to  $\sim 6$  l/min for the whole MVD, as the quadrants of the first two half-stations will be cooled in series. This translates to an increase of the coolant temperature in the detector of less than 1 K. The small volume flow will also keep pressure drops small. To reduce corrosion effects, the coolant should never be still inside the detector – even if it is running idle. For this, it might be beneficial to design a cooling plant that can operate in an idle mode with further reduced flow.

Table 3.2: Proposed parameters of the MVD cooling setup based on the constraints presented in this chapter.

Proposed parameters of the MVD cooling setup	
Cooling capacity	$\sim 225$ W
Coolant	Ethylene glycol/water $\lesssim 30\%$ by weight
Inlet temperature (heat sink)	$\gtrsim -10^\circ\text{C}$
Inlet pressure (heat sink)	$\lesssim 4$ bar (in vacuum)
Volume flow	$\sim 6$ l/min

It is recommended to measure the ion content of the coolant with a conductivity meter at the in- and outlet to monitor and evaluate the corrosion rate. It is typically difficult to measure the oxygen content and the pH inline without changing the salinity. It should therefore be made possible to take coolant samples from an easily accessible port. The necessity of ion-exchangers and demineralisation filters should be evaluated. They are typically expensive and require periodic maintenance to sustain a high degree of purity.

As the MVD will be operating in vacuum, it is impossible to build a system that is leakless due to operation in under-pressure *w. r. t.* the environment. This translates to high demands on the components, especially inside the target chamber. The necessary tightness can be achieved with Swagelok stainless steel compression fittings and NPT threaded fittings<sup>17</sup>. Small leaks inside the target chamber can be spotted in changes of the vacuum pressure and humidity. Bigger leaks can be spotted in large changes of the inlet and outlet pressure and flow. In case of a large leak, shutdown valves in the cooling loop should be triggered, also powering off the detector. In this catastrophic case, a large amount of coolant could end up inside the detector. To prevent collateral damage, a high resistivity of the coolant is critical, which can however corrode soft metals and alloys *s. a.* solder.

As stated in the TDR, a shared Novec 649 cooling system with the CBM STS was anticipated [1]. Triggered by the proposed ban of PFAS, the STS group is also in the process of evaluating the feasibility of switching the coolant from Novec 649 to glycol/water [73]. However, a cooling plant for Novec 649 has already been designed and optimized for the high demands by the STS group which can not be reused for glycol/water [74]. The MVD cooling demands can be met with industrial solutions. Hence, a stand-alone cooling unit should be used, *s. a.* the CC series by

<sup>17</sup>A coolant-compatible and radiation-hard thread sealant has to be used to prevent spiral leakage in threaded fittings. Commercial options exist.

Huber which has been extensively used during the prototyping phase of the MVD. The chiller could possibly be placed underneath the CBM upstream platform, ensuring short supply lines.

Alternatively, a custom-built option could be used. The temperature of the STS return pipes is  $-11.5\text{ K}$  [74] and could therefore be used as the source in a heat exchanger with a glycol/water heat bath. Together with a pump and the necessary monitoring devices, this setup could deliver the cooling power independently of the cave's air conditioning as there is no additional heat entry, and could easily be designed to be radiation-hard<sup>18</sup>.

Condensation and ice buildup on the cooling pipes is another aspect to keep in mind. A thermal insulation of the pipes is necessary. Vacuum insulated piping is not expected to be necessary as standard PE foam insulation should be sufficient. The most critical connection will be at the feedthrough on the front flange. Here, custom-made thermally insulated options do exist. The coolant feedthroughs should be placed at the lowest point of the front flange and no electronics should be placed underneath there, in case condensation water is dripping. Dedicated drains can alleviate this problem.

Cooling above the dew point is probably not feasible, but operation above  $0^\circ\text{C}$  could prevent any ice buildup in the cooling loop. This, however, would require verification that the sensors fulfill the specifications even at  $+30^\circ\text{C}$  and EOL doses.

---

<sup>18</sup>This is not expected to be a driving factor as the total ionizing dose per CBM year underneath the upstream platform is  $\mathcal{O}(10\text{ rads})$  [75].

## 4 Selected Integration Techniques

This chapter summarizes the important aspects of the mechanical integration of the MVD which have been developed within this thesis with the focus on the sensor integration and machining of TPG carriers. A laser processing technique of TPG for high-precision integration of thin, large-area CMOS MAPS on large planar stations has been developed and optimized. As an outlook, a design for a vacuum-compatible, cutting-edge material budget, planar  $\mu$ -tracker based on MIMOSIS sensors using the TPG processing techniques developed within this thesis, has been proposed. This tracker design could be used in the mCBM setup at SIS 18 at GSI. To improve the integration yield the integration of the MVD, reworking strategies for the critical integration steps have been developed. A detailed, step-by-step sensor and detector integration flow from all basic hardware components is proposed, focusing on reworkability and availability of infrastructure and equipment.

### 4.1 TPG Laser Processing

The macro structure and orthotropic properties of TPG which were discussed in chapter 2.2 hampers precise mechanical cutting. However, vaporization cutting with industrial laser cutting devices yields excellent results without introducing mechanical stress. This allows for compensating the insufficient cutting precision by the manufacturer.

A laser depaneling device (LPKF CuttingMaster 2000 [76]) at the GSI Department for Experimental Electronics is available for the CBM MVD team for cutting and structuring TPG by laser ablation. It features a pulsed laser ( $\lambda = 355 \text{ nm}$ ) with variable pulsing frequency ( $10, \dots, 500 \text{ kHz}$ ) and variable power ( $0, \dots, 11.89 \text{ W}$ ). The workpiece can be mounted on a large movable table (working area:  $350 \times 350 \text{ mm}^2$ ) that can be positioned precisely with linear motors (total positioning accuracy:  $\pm 25 \mu\text{m}$  with a beam diameter of  $17 \mu\text{m}$ ). The device is equipped with a camera and a pattern recognizing software to automatically align the table with fiducial marks placed on the workpiece. The device is programmed using an easy-to-use software provided by the vendor. A 2D-sketch can be drawn directly in the software or loaded externally in various data formats such as .dxf. Afterwards, the parameters for the laser and the movement of the table are programmed. The laser operates in scan fields. These are areas of up to  $50 \times 50 \text{ mm}^2$  in which the laser head tilts. For larger working areas, the table is repositioned to move between different scan fields. This contributes to the finite positioning accuracy of  $\pm 25 \mu\text{m}$ . The scan fields have to be optimized depending on the geometry of the cuts and hatches<sup>1</sup> to minimize the parallax arising for deep cuts. Also, it is important to place the workpiece directly in the focus of the laser. Therefore, a flatness of  $500 \mu\text{m}$  or better over the whole area of the carrier is necessary to achieve consistent and precise cuts and hatches.

The parameters of the laser have to be optimized for cutting and hatching depending on the material. Parameters yielding precise and consistent results for processing of TPG have been found experimentally and are summarized in table 4.1.

#### 4.1.1 Cutting

TPG can be precisely cut to straight edges and  $90^\circ$  angles with a precision of  $\mathcal{O}(10 \mu\text{m})$ . This precision can be reached by defining the cut to be either to the outside, the inside, or directly

---

<sup>1</sup>Laser hatching is a technique, where an area ('hatch') on the surface of the material is ablated to a certain depth by scanning it with the laser beam.

Table 4.1: Parameters of the laser vaporization cutter optimized for cutting up to  $500\ \mu\text{m}$  of TPG and hatching  $50\ \mu\text{m}$  deep into TPG.

Parameter	Cutting	Hatching
Power in W	8	8
Pulsing frequency in kHz	50	50
Beam diameter in $\mu\text{m}$	17	17
Number of passes	24	3
Isolation width in $\mu\text{m}$	204	—
Distance pass-to-pass in $\mu\text{m}$	—	19

on the line from the input sketch, and defining the proper isolation width of the cut. For thick sheets, the isolation width has to be adapted for the depth of the cut. For the  $380\ \mu\text{m}$  thick MVD carriers, the best results have been reached with an isolation width of  $204\ \mu\text{m}$  (12 times the beam diameter). The cut is oriented to the outside along the edges of the carrier, and oriented to the inside for the fiducial holes. Figure 4.1 illustrates the process in a sketch of the cross-sectional view of a cut.

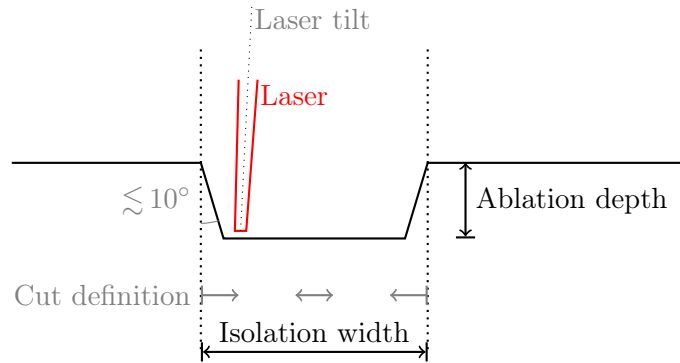
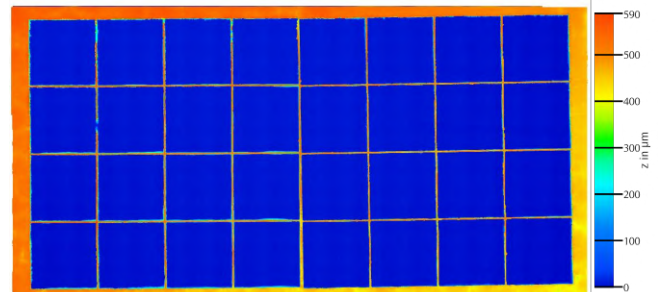


Figure 4.1: Sketch of the cross-section of a laser vaporization cut indicating the ablation depth, the laser beam shape and diameter, the isolation width, the cut definition (i. e. the position of the isolation width w. r. t. the line from the input sketch), and the conical shape along the edge of the cut (opening angle  $\lesssim 10^\circ$ ) which results from the beam shape and scan field parallax effects (i. e. the tilt of the laser). The dimensions and angles are not to scale.



(a)



(b)

Figure 4.2: Laser processed TPG with different structures (a):  $5 \times 5\ \text{mm}^2$  squares, separated by a bridge of  $100\ \mu\text{m}$  (cut); circles with diameters of 8, 4, 2 and 1 mm (cut); CBM-MVD lettering (hatch). 3D-scan of the  $4 \times 8$  square pattern ( $5 \times 5\ \text{mm}^2$ ) seen in figure 4.2a, taken with a digital microscope (b). The height is indicated by the colors.

‘Drilled’ holes in the corners of the carrier can serve as fiducial marks to precisely align the front- and back-side relative to each other. This can be seen *e.g.* in figure 4.3. These fiducials should be still visible on the fully integrated quadrant. Figure 4.2 shows the precision of cuts and holes in TPG.

### 4.1.2 Hatching

The depth of the ablation is influenced by the power of the laser and the number of passes. The overall depth of a cut can be controlled with the precision of a few micrometers by fine-tuning these values [76]. An area can be hatched down efficiently and very precisely by scanning the surface with a set of close, parallel passes of the laser. The tuning of the laser parameters was done by scanning through the power and number of passes, and then measuring the depth of the hatch with a digital microscope.

This technology allows for a different approach to the mechanical integration of the sensors on the carrier. To compare, a detailed description of the mechanical integration of the last prototype (PRESTO) which was fully based on jigs can be found in the TDR [1]. Figures 4.3a, b and 4.4 illustrate the new approach to the integration. Instead of using integration jigs, the sensors are placed in dedicated hatches (depth of  $\sim 50 \mu\text{m}$ ) on the carrier. The precision of the hatches-based technique is at least as good as the precision reached with the jig-based integration technique while also featuring several additional benefits to improve the precision, ease the integration process, and possibly improve the integration yield.

- Sensor-to-sensor distance

A sensor-to-sensor distance of  $\sim 100 \mu\text{m}$  is crucial to guarantee an electrical separation of the sensors. For PRESTO, the sensor-to-sensor alignment was done by hand under a microscope on a dedicated jig. With the new technique, the alignment is done reproducibly with the precision of the laser vaporization cutter. Here, the sensor-to-sensor distance between adjacent sensors is controlled by leaving a small bridge between adjacent hatches.

- Safety margins

To prevent collisions between the carriers of adjacent quadrants, a safety margin of a  $\sim 100 \mu\text{m}$  between the edges of the carriers and heat sinks have to be kept. The heat sinks are the frame of the MVD and should therefore define the origin *w.r.t.* which the sensors are integrated. For PRESTO, the carrier and sensors were aligned by hand to the edges closest to the beam for the integration on a jig. Therefore, the production tolerances of the heat sinks of  $\mathcal{O}(100 \mu\text{m})$  had to be added up, increasing the safety margins.

With the new technique, the safety margins can be reduced by cutting the carrier to the desired dimensions with the laser vaporization cutter and using the heat sink as the reference point. Alignment holes drilled into the carrier allow for a precise and stable alignment of the carrier in the heat sink which defines the origin. Fiducial holes aligned *w.r.t.* the edges of the heat sink allow for precise placement of the sensor hatches, for both front-side and back-side sensors.

- Reproducibility

For PRESTO, the alignment of the components on jigs was done by hand. With the new technique, those jigs become obsolete and the alignment and placement of components is highly reproducible.

- Additional integration steps

With the new technique, the modules are integrated with the carrier already fixed inside the heat sink. This drastically improves the handling of the carrier and significantly decreases the risk of damaging the sensors, FPCs, and bonds on the front-side when flipping the

assembly to integrate the back-side. Moreover, the risky step of moving a fully equipped carrier into the heat sink is saved<sup>2</sup>.

- Restriction of the glue flow

During the assembly of PRESTO, a strong tendency of the glue for the FPC to flow onto the sensors' bonding pads has been observed, making this integration step the most risky of the overall assembly [13]. To mitigate this problem, a double-sided tape was chosen to glue the FPCs instead of a low-viscosity glue. Anyhow, the hatches provide an additional advantage by impeding the flow of the glue which is beneficial for gluing the sensors, but can also improve the situation for the FPC gluing, depending on the choice of adhesive. If the FPCs were to be glued with a low-viscosity epoxy instead of a double-sided tape, a well-defined gluing area by hatches could significantly decrease the risk of glue flowing onto the sensors' bonding pads. This needs to be studied in more detail.

- Material budget

The local reduction of the material budget due to the hatches is a minor, but beneficial side-effect to reduce multiple scattering in the stations. This also reduces the total thermal performance of the carrier, which is, however, not critical for this application when working with the baseline carrier (thickness: 380  $\mu\text{m}$ ). It has been shown experimentally that the mechanical and thermal performance of a TPG carrier with a thickness of only 250  $\mu\text{m}$  is still sufficient for the MVD [77].

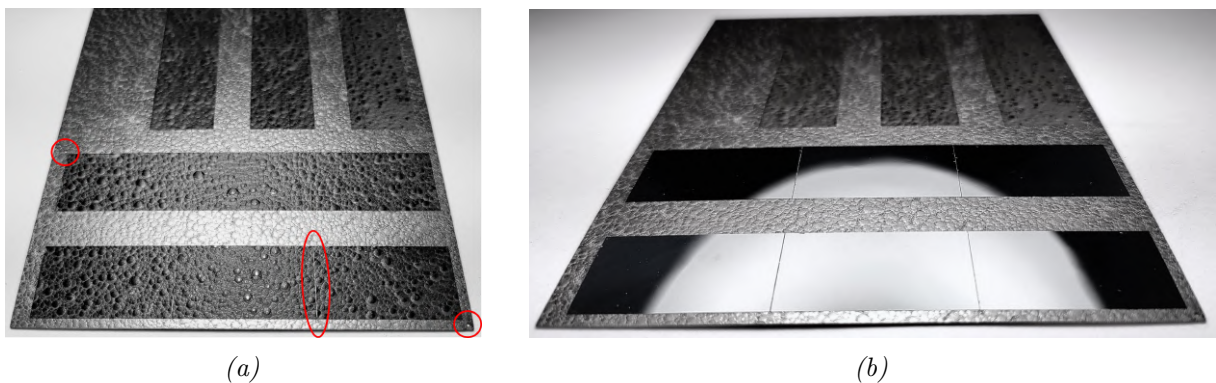


Figure 4.3: Laser processed TPG: Hatches with MIMOSIS form factor and depth of 50  $\mu\text{m}$ . The two fiducial marks for the front- / back-side alignment (diameter: 1 mm) are indicated as well as one of the  $\sim 70 \mu\text{m}$  bridge separating the hatches. Details of the dimensions are listed in table 4.2 (a). Silicon dummies with MIMOSIS form factor (thinned to 50  $\mu\text{m}$ ) placed in the hatches.

The dimensions of the actual hatches are systematically smaller than what is set and the bridges are systematically larger than what is set, see also table 4.2. This is expected from the shape of the laser cone and the parallax at the outer edges of the scan fields and can easily be corrected for, see also figure 4.1. The width set for the bridge separating two adjacent sensors is realized only on the top. The bridge is, as expected, thicker at the bottom.

The thinnest bridge has the most inconsistent shape and thickness. 35  $\mu\text{m}$  as the desired value is already at the edge of the positioning precision of the laser and TPG flakes off substantially.

<sup>2</sup>Technically, the heat sink can be used as the integration jig also without the option based on hatches. Reaching the same precision of the alignment is, however, more difficult with jigs and would require several modifications of the heat sink design.

Table 4.2: Dimensions set on the laser vaporization cutter for a set of hatches and the bridges between adjacent hatches guaranteeing the sensor-to-sensor distance, and their actual values as measured with a digital microscope.

Object	Dimensions set in mm	Dimensions measured in mm
Hatch	$31.15 \times 17.25$	$(31.14 \pm 0.02) \times (17.24 \pm 0.02)$
Hatch	$31.20 \times 17.30$	$(31.19 \pm 0.02) \times (17.29 \pm 0.02)$
Bridge	0.035	$0.045 \pm 0.020$
Bridge	0.070	$0.075 \pm 0.015$
Bridge	0.100	$0.115 \pm 0.015$

Setting  $70 \mu\text{m}$  already yields a very consistent shape. Including parylene coating, a sensor-to-sensor distance between adjacent sensors of  $100 \mu\text{m}$  is feasible<sup>3</sup>.

It is important to optimize the scan fields of the laser to have a smoothly hatched surface, *s. a.* the hatches in figure 4.4. If the scan fields overlap inside the hatch, bridges with a width of  $\sim 10 \mu\text{m}$  remain at the edges of the scan field. They are the result of different angles of impact of the laser and the finite precision of the linear motors positioning the table.

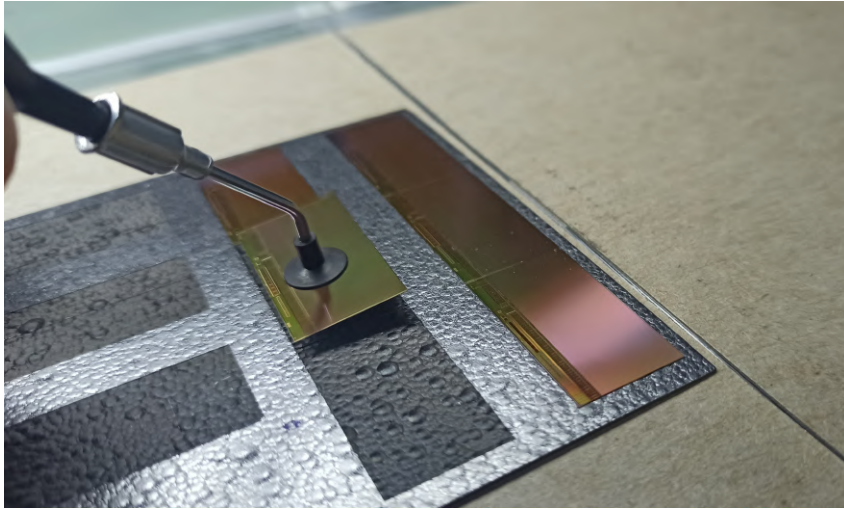


Figure 4.4: MIMOSIS-1 sensors (thinned to  $60 \mu\text{m}$ ) placed in TPG hatches.

It should be noted that MIMOSIS-1 and -2 are prototype chips. Therefore, there are no strict requirements on the precision of the dicing. The cut is not very close to actual chip dimensions but

a margin of  $\mathcal{O}(20 \mu\text{m})$  is left on three sides for thinned MIMOSIS-1,

a margin of  $\mathcal{O}(100 \mu\text{m})$  is left on all four sides for unthinned MIMOSIS-1,

a margin of  $\mathcal{O}(50 \mu\text{m})$  is left on three sides for thinned MIMOSIS-2,

a margin of  $\mathcal{O}(170 \mu\text{m})$  is left on all four sides for unthinned MIMOSIS-2 [78].

The size of the hatches has to be adjusted to the dicing tolerances when integrating the prototype sensors<sup>4</sup>. The final sensor, MIMOSIS-3, will be diced to the actual chip dimensions.

<sup>3</sup>TPG can be coated with parylene of a thickness of less than  $5 \mu\text{m}$ . The micro-structures in TPG do not influence the quality of the coating which is surface-true due to the CVD process.

<sup>4</sup>Also, the thickness of the coating of  $\sim 5 \mu\text{m}$  has to be considered

### 4.1.3 Outlook: $\mu$ -Tracker With Minimum Material Budget

The precise TPG cutting and hatching techniques presented in this chapter can be applied to build a vacuum-compatible, cutting-edge material budget, planar  $\mu$ -tracker based on MIMOSIS sensors. The limits of the conductive cooling concept of the MVD are explored with TPG as carrier material in a double-sided assembly. The task is to explore the limits of the total material budget of vacuum-compatible tracking devices. The proposed design can also be used as a small-scale proof of concept for the mechanical integration using laser processed TPG instead of jigs in a double-sided assembly. The proposed design features:

- Two MIMOSIS sensors, thinned to 50  $\mu\text{m}$ .
- A 100% overlap of the pixel matrices allowing for  $\mu$ -tracking over the whole geometric acceptance.
- A cutout underneath the pixel matrices, minimizing the material budget to the bare minimum, *i. e.* only the sensors.
- Mechanical support and thermal contact only on the digital part of the sensor.

The sensors will be glued only on the digital part and on the corners of the matrix. The digital part is outside of the geometric acceptance and has a much higher heat density than the pixel matrix. The active part of the sensor is cooled conductively, making use of the sizeable thermal conductivity of silicon ( $\sim 150 \text{ W/m}\cdot\text{K}$  at room temperature [79]). The additional support for the pixel matrix in the corners (each only an area of  $0.25 \text{ mm}^2$ ) is necessary for the alignment of the sensors in the hatches and is favorable from a thermal point of view.

The compact tracking device could serve as an mMVD in the mCBM setup at SIS 18 at GSI. The focus of mCBM is the synchronization of the detector sub-systems and the demonstration of the free-streaming DAQ concept. The amount of new components specifically for the mMVD will be kept to the bare necessities, *e. g.* the mounting structure and parts of the services. To a large extent, MVD components will be used that have not been optimized to the mMVD form factors, *s. a.* heat sinks and FPCs.

Figure 4.5 shows the CAD model of the design. A demonstrator using a sheet of 380  $\mu\text{m}$  TPG and two 50  $\mu\text{m}$  silicon dummies with MIMOSIS form factor has been built, proving the feasibility of the mechanical integration of such a device, see figure 4.6. The .dxf sketches of the carrier can be found in [80].

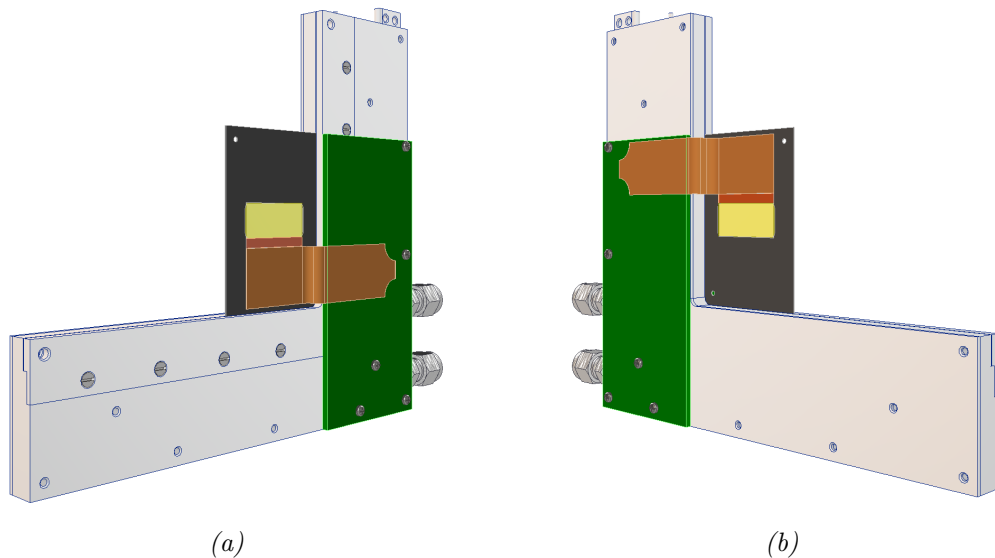


Figure 4.5: CAD view of the front- (a) and back-side (b) of the proposed  $\mu$ -tracker design.

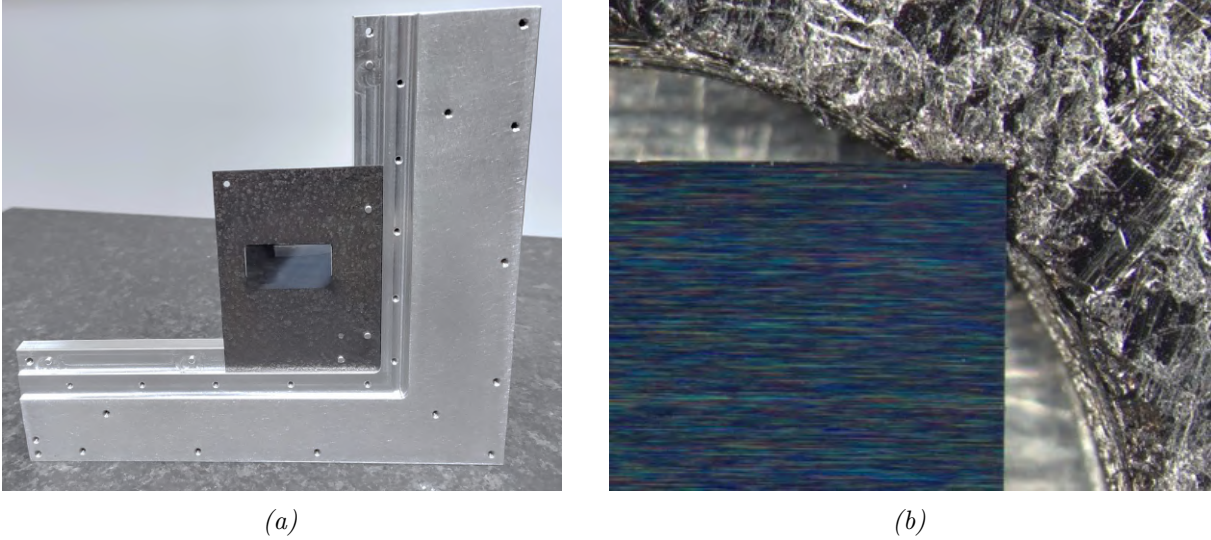


Figure 4.6: Front-side of the mechanical demonstrator of the proposed  $\mu$ -tracker inside a heat sink (a), and an enlarged view on the corner of the silicon dummy, which is glued into a tiny hatch in the surface (b). The radius of the curvature is 2 mm, highlighting the precision of the laser vaporization cutter.

The thermal performance of the proposed design in different configurations has been evaluated using In-CAD Autodesk Inventor Nastran FEA (nonlinear stationary heat transfer). The thermal conductivity of TPG is largely constant in the temperature range of interest ( $-20, \dots, +20^\circ\text{C}$ ,  $1500\text{ W/m}\cdot\text{K}$  in the plane) [23]. The thermal conductivity of silicon depends strongly on the temperature within the temperature range of interest, and is interpolated linearly between the values at  $-23^\circ\text{C}$  ( $195\text{ W/m}\cdot\text{K}$ ) and  $+27^\circ\text{C}$  ( $156\text{ W/m}\cdot\text{K}$ ) [79]. The thermal conductivity of silicon is practically independent of the doping in the temperature range of interest [81]. The sensors are therefore estimated as a homogeneous silicon cuboid with an inhomogeneous heat density distribution. The temperature of the heat sink is set to a fixed value. The power dissipated and its distribution over the sensor can be estimated for maximum occupancy with a sensor at its EOL dose. It is assumed that the complete analog power is dissipated on the matrix (up to  $7\text{ mW/cm}^2$ , see also chapter 2.1). If the sensor is running idle, the digital circuitry on the matrix does not consume any power. The difference of the offset in digital power ( $298\text{ mW}$ ) and the value at maximum occupancy ( $454\text{ mW}$ ) is shared between the matrix and the passive part of the sensor. Assuming that all of the occupancy-dependent part of the digital power is dissipated on the matrix alone gives a generous upper limit on the digital power density (up to  $37\text{ mW/cm}^2$ ) on the matrix and hence on the overall thermal performance with a very large safety margin. The important parameters of the simulation are listed in table 4.3. The actual power density of the matrix is  $\lesssim 10\text{ mW/cm}^2$ . This value is based on simulations for non-irradiated sensors with 8 active data outputs at a mean occupancy of 640 hits per frame [17].

Several cases have been simulated to study the effects of the absolute temperature, the thickness of the carrier, and the thermal interface on the corner of the matrix. The results are summarized in table 4.4 and the corresponding plots can be found in the appendix A.5. A temperature difference of up to 5 K over the sensor is deemed acceptable<sup>5</sup>.

As expected, the maximum temperature difference is slightly larger ( $< 10\%$ ) for the option with the thinner carrier. Also, due to the temperature dependence of the thermal conductivity of silicon, lower operation temperatures are favorable. A good thermal contact of the corners

<sup>5</sup>This value is motivated by requirements for the MVD sensor during the conceptual design phase. There is no measurement of the MIMOSIS performance with a (controlled) temperature gradient, but recent studies with MIMOSIS-1 suggest only a small dependence of the sensor performance on the absolute temperature (judged by s-curves and DAC scans), see also figure 2.4b.

Table 4.3: Parameters of the thermal simulations for the proposed low-material budget  $\mu$ -tracker designs [23, 79]. The power densities have been estimated based on figure 2.5a.

Parameter	Detail	Value
Power density in mW/cm <sup>2</sup>	Pixel matrix	44
	Digital part	260
Thermal conductivity in W/m·K	TPG	1500 in x-y - plane 10 in z
	Silicon	193 at -20 °C
		177 at 0 °C 161 at +20 °C
Thickness in $\mu$ m	TPG	380, 250
	Silicon	50

of the matrix to the carrier can significantly reduce the maximum temperature difference by  $\sim 25\%$ . The absolute values of the maximum temperature difference are in parts below, and in parts slightly over the acceptable value, especially for the option with the corners of the matrix unconnected. The safety factor of  $\sim 4$  *w. r. t.* the power density on the matrix and the relaxed estimate on the maximum acceptable temperature difference over a sensor should also be taken into account. The feasibility of this advanced concept and design is confirmed by combining the sufficient thermal performance shown in simulations with the mechanical practicability shown with the mechanical demonstrator.

Table 4.4: The temperature difference between the hottest point on the matrix and the coldest point on the carrier for several configurations and operation temperatures of the proposed  $\mu$ -tracker design. The values have been simulated with In-CAD Autodesk Inventor Nastran FEA (nonlinear stationary heat transfer). The most important simulation parameters can be found in table 4.3.

$d_{\text{TPG}}$ in $\mu$ m	$T_{\text{Heat sink}}$ in °C	Matrix corner	$\Delta T_{\text{Max.}}$ in K
380	-20	Glued	4.1
		Unconnected	5.1
	0	Glued	4.4
		Unconnected	5.5
	+20	Glued	4.7
		Unconnected	5.9
250	-20	Glued	4.5
		Unconnected	5.6
	0	Glued	4.8
		Unconnected	5.9
	+20	Glued	5.1
		Unconnected	6.3

If sufficient ( $\gtrsim 25$  mm) space is reserved for an FPC as is done in the proposed design, the thermal performance can not be improved anymore by increasing the size of the carrier as the temperature on the TPG saturates. The thermal contact between the sensor and the carrier is crucial to guaranteeing that the heat dissipated by the digital part of the sensor is conducted into the carrier and not onto the pixel matrix. This can be realized by a thin and even layer of glue.

The idea can be pushed to larger form factors, using four sensors. As the aspect ratio of the MIMOSIS pixel matrix is not 1:2, two different configurations can be realized: The first option is having less than a 100% overlap of the geometric acceptances (front- and back-side) and a quadratic opening ( $\sim 4 \times 4 \text{ mm}^2$ ) in the center, *e.g.* as a beam hole in a fixed target experiment, and no inactive material inside the acceptance. The other option is keeping the full overlap of the geometric acceptances and a 100% fill factor, but this introduces carrier material at the outer corners of the acceptance.

The concept is pushing the limits of the total material budget of a vacuum-compatible tracking device. A significant challenge is the scaling to large form factors, which is typical for MAPS detectors. The version of two sensors back-to-back can be scaled to ladders of several sensors. A reduction of the power density is beneficial, alleviating the requirements on the cooling. Also, lower operation temperatures improve the thermal performance, making use of the rapidly increasing thermal conductivity of silicon.

## 4.2 Reworking Strategies

In a complex assembly like the MVD quadrants with 28 sensors and double-sided integration, it is crucial to define high-yield and low-risk reworkability options for all critical integration steps. The proposed integration flow is described in detail in chapter 4.3. Critical integration steps have been identified and include the gluing of the sensors and the FPCs, as well as the wire bonding. Everything else related to sensor or detector integration can either be easily reworked (*e.g.* the mounting of the FEBs, fittings, piping), and/or is expected to have perfect yield (*e.g.* cutting, hatching, coating, and activation of the carrier).

- Sensors

The challenging part is to completely remove a broken sensor to not increase the material budget locally<sup>6</sup>, without influencing the adjacent sensors, while maintaining the coating of the TPG. The high adhesive strength of the epoxy, the delamination of TPG, and the high integration density on the carrier prohibit any mechanical processes, *s.a.* ripping off the sensor or CNC-milling. The hatching technique for TPG presented in chapter 4.1.2 has been adopted for hatching down single sensors from the carrier with high precision. It can be applied to sensors not covered by FPCs, if the fiducial marks for the alignment of the laser are still visible on the carrier. A small residue of the substrate of the sensor is left to ensure that the coating is not destroyed. Also, the surface energy of silicon is sufficient for gluing another sensor on top without the need for another plasma activation<sup>7</sup>. The placement of the new sensor is simple as the old hatch is almost fully restored.

Unlike TPG, a CMOS MAPS is not a homogeneous material. The top  $\sim 10 \mu\text{m}$  is Al in Si (this is the circuitry) and underneath is bare silicon ( $25 \mu\text{m}$  epitaxial layer, the rest is substrate). The parameters of the laser vaporization cutter have been optimized to hatch down  $\sim 40 \mu\text{m}$  of the sensor:

3 passes at 6 W with a pulsing frequency of 50 kHz.

Additionally to the residue of the substrate of the sensor, the  $30 \mu\text{m}$  of the glue layer remain. The material budget increases locally by the material budget of one layer of glue and  $\sim 10 \mu\text{m}$  of silicon, *i.e.* a material budget  $x/x_0$  of  $\lesssim 0.02\%$ .

The feasibility of laser ablating individual sensors was demonstrated with electrically broken MIMOSA-26 sensors and metalized, thinned dummies with MIMOSIS form factor, see figure 4.7. It has been observed that the structures in the metalization layer are still

<sup>6</sup>The repair strategy presented in the TDR, *i.e.* gluing and bonding a second sensor on top of a broken one, has been considered unsatisfactory for detector-grade MVD quadrants.

<sup>7</sup>The required surface energy is  $47 \text{ mN/m}$  and bare silicon has a surface energy of  $43 \text{ mN/m}$  [82].

visible in the epitaxial layer / substrate after the hatch. This can be expected from the inhomogeneities in the metalization layer that result in local differences of the vaporization energies and absorption coefficients. The high reflectivity of the sensors' surface, which can be seen for the unhatched MIMOSA-26 sensors in figure 4.7a, is not an issue. A metalized dummy sandwiched between two bare silicon dummies, all placed inside sensor hatches, has successfully been hatched down, see figure 4.8. The table of the laser vaporization cutter was aligned to the fiducial marks used for producing the sensor hatches, proving that the placement precision of the table of the laser vaporization cutter is sufficiently reproducible.

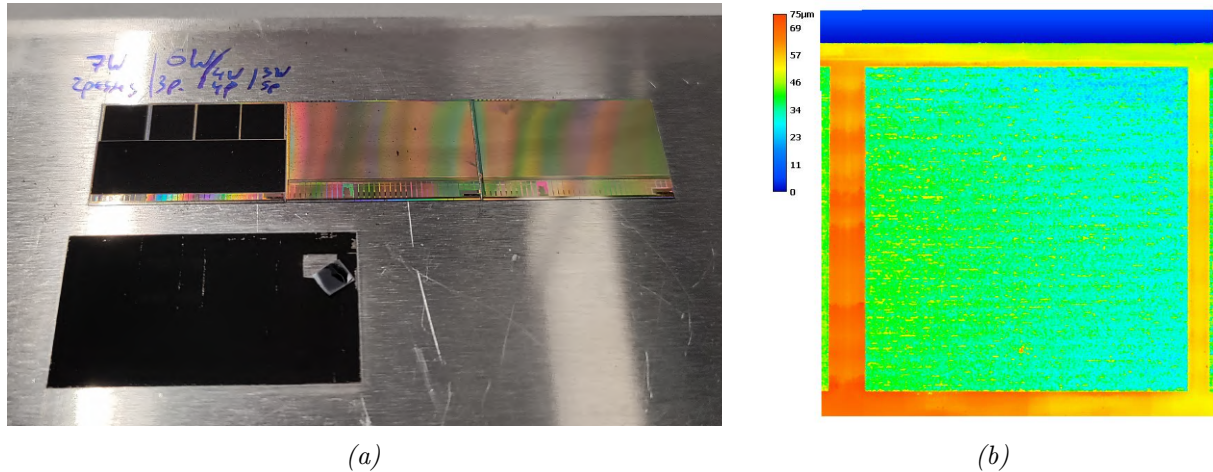


Figure 4.7: Aluminum carrier for sensor hatching studies: Three MIMOSA-26 sensors, one with  $5 \times 5 \text{ mm}^2$  square hatches of different depths and a  $7 \times 21 \text{ mm}^2$  hatch (top left). The two adjacent MIMOSA-26 sensors are not hatched. A metalized, thinned dummy with MIMOSIS form factor hatched down completely with a small, delaminated piece (a). 3D-scan of a  $5 \times 5 \text{ mm}^2$  square hatch on a sensor with optimized settings, taken with a digital microscope (b). The noticeable global gradient in the height profile results from the natural curvature of the sensor which is caused by internal stress and is still present after gluing.

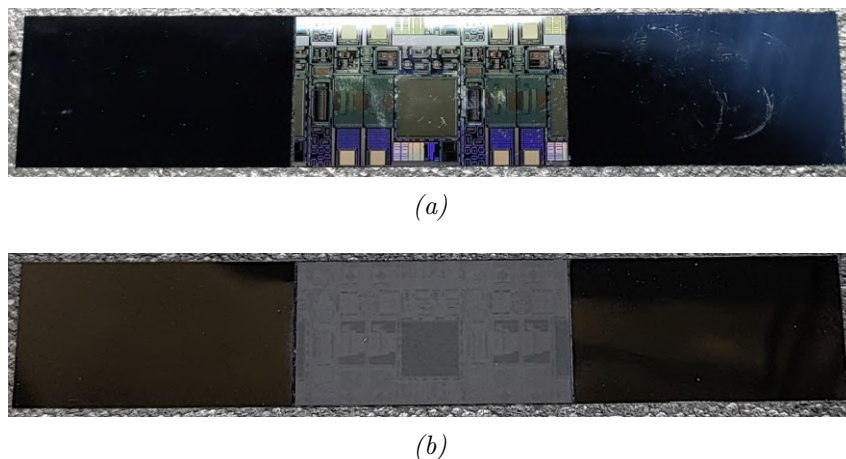


Figure 4.8: A metalized dummy sandwiched between two bare silicon dummies, all placed inside sensor hatches, before (a) and after (b) hatching it down. The CMOS and metalization structures are still visible after the hatch.

- FPCs

The gluing of the FPCs can be reworked if the double-sided adhesive tape is used instead of the epoxy options. The FPCs can be carefully peeled off the double-sided adhesive tape,

with the tape remaining adhered to the carrier. The feasibility of this is very closely linked to the delaminating properties of TPG. The adhesion between the tape and bare TPG is significantly stronger than the cohesion of the TPG itself. Parylene coating can, however, significantly improve the surface properties of the carrier, allowing for a sufficient adhesion between the tape and the carrier. This adhesion is stronger than the adhesion between the tape and the FPC, allowing the reworkability of this connection.

A new FPC can be glued onto the double-sided tape. Additionally to the drawbacks of the alternatives (Loctite Ablestik 45 and EpoTek 301-2) discussed in chapter 2.3, the reworkability of FPCs glued with the epoxy adhesives is worse due to their high adhesive strength and the delamination of TPG. A large peel angle close to  $180^\circ$  is crucial. Else, the TPG will slightly delaminate underneath the coating. The tape itself can also be peeled off parylene-coated TPG with a very large peel angle, allowing for a full rework of the FPCs. The adhesion of the tape to the parylene-coated surface is sufficient, even without plasma activation.

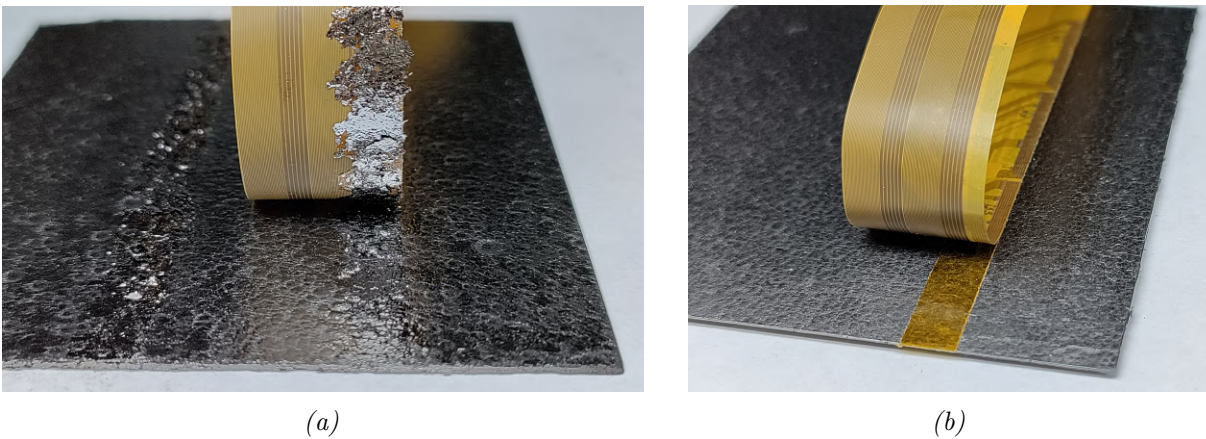


Figure 4.9: Peeling off a single-layer FPC that was glued with double-sided adhesive tape from an uncoated (a), and a parylene-coated (b), polished sheet of TPG.

It is almost impossible to remove very stiff FPCs without slightly delaminating the TPG underneath the coating. This has been observed with double-layer FPCs for the MIMOSA-26 sensors that were stacks of two single-layer FPCs, glued together with an epoxy. The issue of delamination has been directly linked to the maximum peel angle that can be reached. For ultra-thin, single-layer FPCs, reworking can easily be done. It has to be evaluated whether this is also feasibly for ultra-thin, (partly) double-layer FPCs. Double-layer FPCs that are assembled from two single-layer FPCs can be reworked by first peeling the top FPC off the bottom FPC, and then the bottom FPC off the carrier. This is only feasible if they are glued with the double-sided tape as well and not with a stiff epoxy.

The exact properties of the adhesive on the double-sided tape under strong irradiation is not known. Another iteration of this study, focusing on this question, can be helpful. However, only a decrease of the adhesive strength is expected which would increase the reworkability even further.

- Bonding

In case a re-bond is needed, the old bonds can be ripped off the sensor and FPCs. The reworkability of wire bonds is limited by the size of the bonding pads. The size of the bonding pads on the sensor and the FPC allow for two bonds per pad, possibly even three.

## 4.3 Sensor Integration Flow

The integration flow presented here is a detailed, step-by-step guide for the integration of an MVD half-station. The order is optimized for yield and reworkability. The necessary equipment for the different integration steps has been identified. Most of the necessary equipment and infrastructure for the MVD integration that can not be provided at the IKF is available for the CBM MVD team at GSI. It is therefore recommended to perform the majority of the integration at a dedicated stand in the cleanroom of the GSI Detector Laboratory (DL) before finishing the detector integration. This will allow for a time-efficient integration procedure of the MVD and minimize the risk introduced by frequent transporting between IKF and GSI.

The relatively short lifetime of the plasma activation of the carrier translates to a quick gluing of all components on the carrier (front- and back-side). The high risk of damaging sensors by electric discharge of the plasma prevents any re-activation. Hence, the front- and back-side integration of the sensors can not be decoupled. To allow for reworking single sensors with the hatching technique presented in chapter 4.2, the FPCs can only be glued row-by-row, allowing for a detailed QA of the row of sensors before covering the row with the FPC of the succeeding row. This introduces the risk of damaging bonds during the placement of the next FPC which has to be weighed up against the option of reworking single sensors on a quadrant. The FPCs should be glued with the double-sided tape to allow for reworking them independently of the activation level of the carrier. The design of the integration jig is described in the appendix A.3. The proposed sensor integration flow is:

### 1. QA of all necessary components

The quality of all necessary hardware components has to be assured before starting the integration. For a quadrant of geometry  $c$ , 28 MIMOSIS sensors, one carrier, four FPCs for the front-side and three FPCs for the back-side, one heat sink, one front-side FEB and one back-side FEB, the selected adhesives, and several sets of screws of different lengths and sizes are needed. For a quadrant of geometry  $b$ , the form factor of the components is smaller, and only eight MIMOSIS sensors and two FPCs for the front-side and two FPCs for the back-side are needed. The QA procedure for the components is described in detail in chapter 2.

### 2. Processing of the carrier

As a first step, the carrier is cut on the two adjacent sides that are placed in the heat sinks. Holes for the alignment pins on the heat sink balcony and two fiducial marks are cut. The carrier is placed in the heat sink and the positions of the fiducials *w. r. t.* the sides of the heat sinks are measured to align the hatches, compensating the heat sink's production tolerances. Afterwards, the hatches for the sensors can be produced on the front- and back-side using the fiducial marks to align them<sup>8</sup>. The remaining two sides of the carrier can be cut, finalizing its form factor. This integration step has to be done at the laser vaporization cutter at the GSI Department for Experimental Electronics available for the CBM MVD team. It takes about 1 hour to fully cut and hatch one carrier. The 2D-sketches of the cuts, holes, and hatches in the carriers (front- and back-side, geometry  $b$  and  $c$ ) can be found in [25].

### 3. Coating of the carrier

As a next step, the carrier has to be coated with  $\sim 5 \mu\text{m}$  of parylene-C. This step can be done at Plasma Parylene Systems GmbH. There are no logistical challenges, *s. a.* harsh requirements on the packaging attributed to this integration step.

<sup>8</sup>A unique identifier should be laser-engraved into the carriers and heat sinks to match them correctly during the integration process.

#### 4. QA of the carrier's coating

The coating has to be visually inspected with a standard light microscope for inconsistencies, especially along the edges of the hatches. It can be confirmed with dummies that the form factor of the hatches is correct and sufficient after coating.

#### 5. Plasma activation of the carrier

As the lifetime of the plasma activation is critically short with  $\sim 7$  days, it needs to be decoupled from the coating process. The carrier can not be plasma activated again after the sensors have been glued onto the TPG, as the electrostatic discharge during the plasma activation can destroy them. Hence, the subsequent integration steps of gluing the sensors and the double-sided tape for the FPCs are the most time-critical steps. They should be performed as soon as possible after the integration, including also their QA. It is hence recommended to do these steps at the same laboratory, either at IKF or GSI, where the necessary infrastructure has to be provided, *i. e.* a plasma activation device, a station for glue mixing (*e. g.* a precision scale and vacuum chamber to outgas the glue), a glue distribution system (*e. g.* a single-channel pipette), and a low-volume testing vacuum chamber, all set up in a clean environment. The plasma activation for both sides of the carrier takes a few minutes with a hand-held plasma activation device that is available for the CBM MVD team at the cleanroom of the GSI DL.

#### 6. Gluing of the double-sided tape for the FPCs

First, the strips of double-sided tape for the FPCs are glued onto both sides of the carrier and pressed firmly. The placement of the tape can be done by hand. A precision of 100  $\mu\text{m}$  is sufficient and the placement and alignment is guided by the sensor hatches. The top cover layer should not be removed yet.

#### 7. QA of the double-sided tape for the FPCs

The vacuum-compatibility of the double-sided tape strips has to be assured. Large bubbles of air trapped underneath the tape can be spotted in a visual inspection and can be removed by hand. It has been shown that tiny air bubbles do not affect the vacuum-compatibility. Nonetheless, the vacuum-compatibility should be confirmed in a medium vacuum. If issues arise, the corresponding tape can be removed carefully and a new strip can be glued.

#### 8. Mounting of the carrier to the support structure

The support structure is made out of two pieces: The heat sink with the clamp holding the carrier, and the front-side of the integration jig which supports the carrier inside the acceptance during integration.

#### 9. Gluing of 16 sensors on the front-side of the carrier

16 sensors (four rows of four sensors each) are glued onto the front-side of the carrier with 17  $\mu\text{l}$  of EpoTek 301-2 placed in each of the hatches in the optimized gluing pattern. The glue is fully cured for 48 hours at room temperature. Curing at higher temperatures should be avoided to reduce the thermal stress due to CTE mismatches. Also, higher temperatures will degrade the surface energy from the plasma activation even quicker.

#### 10. Gluing of 12 sensors on the back-side of the carrier

The heat sink - carrier assembly is turned around and placed in the back-side of the support jig. 12 sensors (three rows of four sensors each) are glued onto the back-side of the carrier with 17  $\mu\text{l}$  of EpoTek 301-2 placed in each of the hatches in the optimized gluing pattern. The glue can fully cure for 48 hours at room temperature. This is the last time-critical step of the assembly.

#### 11. QA of the sensor gluing

The vacuum-compatibility of the assembly is tested in a medium vacuum. If issues with the vacuum-compatibility arise, the reworking strategy presented in chapter 4.2 can be applied.

#### 12. Metrology of the sensors

The positions of the sensors are fixed at this step of the assembly and the sensors, including fiducial marks, are still uncovered. The position of the sensor fiducial marks need to be measured to use them as seeds for a track-based alignment of the detector afterwards.

#### 13. Mounting of the front-side integration FEB

The front-side integration FEB is screwed onto the front-side of the heat sink which is only possible after the carrier is mounted, because it sits on top of the clamp that fixes the carrier.

#### 14. Gluing of the first FPC

The first FPC, *i. e.* the one closest to the heat sink, is glued. For this, the top cover layer of the tape is removed, the FPC is connected to the FEB and then pressed gently onto the tape. In case the double-layer FPCs has to be assembled from two single-layer FPCs, it is recommended to adhere a strip of double-sided tape to the top-side of the bottom FPC first before adhering the bottom FPC to the carrier. Afterwards the top FPC can be adhered to the bottom FPC which is already firmly attached to the carrier. This allows for optical QA of all connections and reworkability.

#### 15. QA of the FPC gluing

The vacuum-compatibility of the assembly is tested in a medium vacuum. If issues with the vacuum-compatibility arise, the reworking strategy presented in chapter 4.2 can be applied.

#### 16. Bonding of the first row of sensors

The first row of sensors is wire-bonded to the FPC. Additionally to the required bonds, also several sacrificial bonds should be made for QA purposes. The bonding should be done with an automatic bonder, of which several are available for the CBM MVD team at the cleanroom of the GSI DL. The working area of the Delvotec M17L is large enough ( $652 \times 350 \text{ mm}^2$  [83]) to fit the form factor of the MVD carriers of geometry *c* with the heat sinks as mechanical support. For the smaller quadrants of geometry *b*, the smaller version (Delvotec M17S, working area of  $254 \times 152,4 \text{ mm}^2$  [83]) should be sufficient.

#### 17. QA of the bonding

Besides a visual inspection of the bonds, the quality of the bonding can be assessed by destructive pull-tests of the sacrificial bonds. The breaking force should be larger than 5 g, with an average breaking force of 8 g. The pull-testing of the bonds can be done with a manual pull-tester head available for the CBM MVD team at the cleanroom of the GSI DL<sup>9</sup>.

#### 18. Characterizing the sensors' performance

The integration FEBs are connected to the powering and readout system and the sensors are characterized. The QA procedure of the probe testing is repeated and the results before and after integration are compared. If a sensor fails the test, it is re-bonded and tested

---

<sup>9</sup>An encapsulation of the bond feet or the whole bonds with *e. g.* EpoTek 301-2 is not intended. A bond encapsulation comes along with additional risk during the assembly and operation, as the different coefficients of thermal expansion can yield to additional stress on the bond feet, possibly destroying the bonds over time and several temperature cycles. Mechanical issues from vibrations of non-encapsulated bonds, triggered *e. g.* by the vacuum pumps or the cooling liquid in the heat sinks, have not been observed during prototyping.

again. If this does not solve the problem, the reworking strategy for the sensor presented in chapter 4.2 can be applied. The exact coordinates of the fiducial marks on the newly glued sensor have to be measured. Afterwards, the sensor can be bonded and characterized.

#### 19. Pre-conditioning the sensors

At this integration step, the sensors can be pre-conditioned with X-rays to the required dose. It is recommended to do this row-by-row, keeping the ability to rework single sensors if they take permanent, critical damage during the pre-conditioning<sup>10</sup>. The feasibility and technical realisation of a possible pre-conditioning needs to be evaluated carefully.

#### 20. Characterizing the sensors' performance

After pre-conditioning the sensors, they have to be characterized again to account for the threshold shift. The values obtained in this characterization step are final and can be used to tune the detector during the beamtime.

#### 21. Finishing the front-side integration

The remaining rows are integrated and tested row-by-row. The steps 14 to 20 are repeated.

#### 22. Finishing the back-side integration

For the integration of the back-side of the carrier, the assembly is flipped and mounted to the back-side of the integration jig. Afterwards, the steps 13 to 21 are repeated for the back-side.

#### 23. Integrating the second quadrant of a half-station

The integration flow for the second quadrant of a half-station is identical to the first one, using only the different version of the heat sink. The only difference is that the cooling channel is mirrored which however only influences the detector integration. Hence, all the steps from 1 to 22 can be repeated.

#### 24. Mounting two quadrants to a half-station

The back-side integration FEBs are removed. The two quadrants are screwed together on the corresponding connector. Next, the C-shaped back-side FEB is screwed and the FPCs are connected. Then, the assembly is flipped, the front-side integration FEBs are removed, the C-shaped front-side FEB is screwed, and the FPCs are connected.

#### 25. Final QA and storage

For the final QA, the heat sinks need to be connected to a cooling system for tests under realistic conditions. This includes powering and reading out the half-station with the FEAST DC/DC converters and GBTx, respectively. Several vacuum, power, and temperature cycles should be performed, closely monitoring the performance, to later ensure a stable, long-term operation<sup>11</sup>. After the final QA, the half-stations should be stored in a clean environment with stable, controlled temperature and humidity, *e. g.* a nitrogen flowbox in a cleanroom.

<sup>10</sup>*E. g.* for MIMOSIS-1, a significant vulnerability of the on-chip DACs to ionizing radiation has been observed during SEE studies [19].

<sup>11</sup>For this, the half-stations can already be integrated into the dedicated MVD EPICS control and monitoring system.

### 4.3.1 Open Questions

Four open questions *w. r. t.* the sensor integration remain which concern a component database, the tests of the vacuum-compatibility, the metrology, and the bonding.

- Component database

A database has to be set up featuring all components with identifiers and the results from their QA. Here, infrastructure already built for the CBM STS can possibly be reused.

- Tests of the vacuum-compatibility

The test protocol for the vacuum-compatibility of the assembly is not defined yet. The testing vacuum chamber should be small to allow for quick pumping, but needs a sufficient size to fit at least one quadrant, better a half-station of geometry *c.* A large aperture to (un-)load the chamber is important. The requirements on the vacuum are not very harsh, the intended pressure of  $\sim 10^{-2}$  mbar can easily be achieved with a rotary vane pump. The chamber should either be see-through (*e. g.* made from glass or acrylic) or equipped with a window to observe lifting-off of components. Special care needs to be taken during the venting procedure to prevent damage of the fragile quadrants, *e. g.* of the numerous wire bonds.

- Metrology

A detailed plan for the metrology of the quadrants has to be worked out, including the identification of the proper equipment. The metrology can possibly be realized by a custom-made device developed for the CBM STS (precision of 10  $\mu\text{m}$ ) which is located at the cleanroom of the GSI DL. The feasibility of this and the availability of the device have to be explored.

- Bonding

The bonding scheme needs to be finalized along the design of the FPC and then implemented for the automatic bonding. Additionally to the discussion in chapter 2.4,  $\mathcal{O}(10)$  bonds per sensor that are not necessary for the operation of the detector and can be used for destructive pull tests have to be identified.

## 4.4 Detector Integration Flow

The integration flow presented here is a rough draft of all the necessary detector integration steps. The work can in parts be done in the laboratories of the IKF. As the majority of the sensor integration should take place at GSI, the final steps of the assembly, where the fragile half-detectors are mounted to the solid master table on the front flange, should be done at GSI, avoiding unnecessary transportation of the detector or half-stations. A stable integration support structure for the front flange should be designed. The half-detectors should be mounted standing up. This support structure can also be used to transport the detector. If a dedicated cover with the form factor of the target chamber is added, the support structure can also be used for storage of the MVD. The proposed detector integration flow is:

1. QA of all the components

The quality of all necessary hardware components has to be assured before starting the integration. This includes the top plates with FEAST DC/DC converters, the coolant manifolds with the piping, the front flange and master table with the feedthrough flanges, the remote positioning system and the baseplates.

## 2. Bending the pipes

The stainless steel pipes connecting the heat sinks and top plates with the in- and outlet manifolds need to be bent and cut to the correct shapes and lengths. The layout, lengths and angles can be extracted from the CAD model. This should be done in a CNC pipe bending process.

## 3. QA of the piping

The quality of the piping can be assessed using 3D-printed jigs. The pipes should then be pre-swaged before the assembly to minimize the stress on the half-stations and top plates. The manifolds can be connected to a stand-alone cooling unit to perform leakage tests under pressure. If necessary, the leaky components can be reworked.

## 4. Assembling the top plates

The PCBs housing the FEAST DC/DC converters and the cooling fins have to be mounted onto the top plates.

## 5. Assembling the baseplates

The coolant manifolds have to be screwed onto the baseplates. Here, a proper thermal insulation of the manifolds and the baseplate should be identified. The baseplates are mounted onto the remote positioning system.

## 6. Mounting the small half-stations

The two upstream MVD half-stations (geometry *b*) are mounted from underneath to the baseplate. The small top plate is mounted from the top to mechanically stabilize the assembly.

## 7. Connecting the services of the small half-stations

The small half-stations are still very accessible at this point. All the piping should be connected now. Also, the respective FEAST DC/DC converters should be connected to the FEBs at this step of the assembly.

## 8. Mounting the large half-stations

The two downstream MVD half-stations (geometry *c*) are mounted from underneath to the baseplate. The large top plate is mounted from the top to mechanically stabilize the assembly. The triangular construction with the crossbars can be mounted to further increase the mechanical stability.

## 9. Connecting the services of the large half-stations

The rest of the half-station piping and the remaining FEAST DC/DC converters should be connected to the FEBs at this step of the assembly.

## 10. Assembling the second half-detector

The integration flow for the second half-detector is identical to the first one. Hence, all the steps from 6 to 9 can be repeated.

## 11. Assembling the ROB feedthrough flanges

The ROB flanges have to be assembled by gluing the passive feedthrough PCBs into the slits in the flanges. The vacuum tightness of the assembly should be tested afterwards. The ROB should not be connected to the feedthrough board yet to prevent damage.

#### 12. Assembling the front flange

All the feedthrough flanges (power, ROB, coolant, possibly nitrogen) have to be mounted to the front flange from the upstream side. Then, the master table is screwed onto the front flange from the downstream side. The vacuum tightness of the flanges should be tested before mounting the half-detectors.

#### 13. Mounting of the half-detectors

The remote positioning system should be in the parking position with the half-stations moved apart from each other to prevent collisions during the assembly. The half-detectors are mounted onto the master table from underneath and the remote positioning system is tested.

#### 14. Connecting the services

The coolant manifolds are connected to the coolant feedthroughs with the flexible hoses. The ROBs are connected to the feedthrough boards and the ROB FPCs are connected to the half-stations, station by station, starting with the most upstream station. A QA of the electrical connection should be done before connecting the succeeding station.

#### 15. Commissioning in the laboratory

The fully assembled MVD is covered by a protective box of similar form factor to the target box. This box can be flushed with *e. g.* nitrogen. The MVD can be commissioned in the laboratory, performing the final QA which includes power and temperature cycles.

#### 16. Mounting in the cave

The MVD can now be moved to the CBM cave and be installed there. This includes screwing the front flange to the target chamber and connecting all the services. The MVD can be commissioned in vacuum and at the target operation temperature.

## 5 Summary and Outlook

This chapter summarizes the findings and advances towards the integration of an MVD pre-series module. The structure of the thesis, separating sensor and detector integration, and the selected integration techniques is kept.

With this thesis, significant advances in the transition from prototyping to the mechanical integration of a pre-series module of one of the largest quadrants of the CBM MVD (geometry  $c$ ) have been made. This includes not only the development of advanced integration techniques, but also fine-meshed QA procedures and reworking possibilities. Open questions that need to be addressed before mass production have been identified and, wherever possible, a detailed workplan has been proposed.

### 5.1 Sensor Integration

The experience gained in the handling of large-area thinned silicon pixel sensors and in motorized manual needle probe testing form the necessary pre-requisites for mass-testing sensors of the MIMOSIS family. Subsequently, those can be integrated in a complex assembly with a high integration density *s. a.* the MVD. A QA procedure for MIMOSIS sensors based on needle probe testing has been developed and is ready to be implemented and optimized for MIMOSIS-1 sensors in a collaborative effort of the working group. The prober bench setup available at IKF has been optimized *w. r. t.* the mechanical support of single sensors, and the co-planarity of the sensor chuck and needle tips. Preliminary probe testing efforts with a custom-made needle probe card featuring 101 needles revealed significant connectivity issues due to oxidation, and possible other residue, of the bonding pads on the prototype sensors. A solution for this problem has been identified and tested using a wet-etching process on the bonding pads with diluted phosphoric acid. The preparations for mass testing are ongoing.

The form factors of the TPG carriers have been finalized. The drawbacks of TPG, associated to its bulk and surface properties, *i. e.* softness, delamination, abrasion and electrical conductivity, have been addressed and mitigated. This comes with additional work steps to carefully prepare the carriers prior to the integration. For the surface properties, a minimization of abrasion and the reduction of the surface electrical conductivity can be achieved by parylene-C coating. Together with a consecutive plasma activation to improve the gluability on the hydrophobic coating, this has been identified as a suitable option which is compatible with all other selected materials. Together with an industrial partner, the coating and activation procedure has been tested and validated for the MVD.

The adhesive selection presented in the TDR has been carefully re-examined. The distribution pattern and adhesive amount for MIMOSIS sensors has been optimized on TPG with silicon dummies of the correct form factor using infrared photography as QA tool. A thin, double-sided tape has been identified as a high-yield, low-mass gluing alternative to epoxies for attaching the FPCs to the carrier. The option also has proven to provide a high reworkability in tests. A radiation-hard alternative to the dedicated thread sealant used in prototyping has been identified. The long-term stability and coolant compatibility appears to be fine, but could not be conclusively clarified yet.

No progress has been made on FPC development as this is crucially dependent on the probe testing and the stand-alone QA procedure which is work in progress.

The engineering design of the heat sinks has been finalized to a large extent with only minor changes in the placement of *e. g.* screw holes expected. Two heat sinks forming a half-station of geometry *c* have been produced and fulfill the MVD specifications *w. r. t.* to precision and planarity. The validation of the thermal performance is in preparation.

## 5.2 Detector Integration

The detector integration was not the focus of this thesis. Nonetheless, some progress has been made. Actively cooled top plates housing up to 94 FEAST DC/DC converters for the powering of the sensors have been designed.

A demonstrator of the coolant manifolds has been designed and intensely tested. The tests were focused on compatibility issues with the coolant and the producibility of challenging piping with high precision by hand.

A parametric CAD model of the MVD is work in progress. It features the highest level of detail as the prerequisite for further activities, *s. a.* the spotting for conflicts in the design due to static collisions of components and dynamic collisions between components *e. g.* during the assembly or beam tuning. The keep-in volumes defined for the collaboration in a CBM Technical Note [54] have been confirmed, also after a changing to a different ROB form factor.

A quick overview on the latest status of the MVD cooling system, finalizing the specifications and re-iterating the choice of coolant is given. This is triggered by the search for alternative coolants to Novec 649 and alleviations of the constraints on the MVD operation temperature.

## 5.3 Selected Integration Techniques

A goal of this thesis was the development of a reliable and robust integration flow for the largest quadrants, comprising the preparation of components and their handling, and QA procedures.

A high-precision, high-yield processing technique for TPG using an industrial laser depaneling device has been developed. The parameters have been optimized for precision cutting and surface hatching which is impossible by mechanical procedures due to the delamination properties of the material. The surface hatching technique opens the door for a novel, jig-less integration technique. Placing sensors in dedicated hatches on the surface provides a low-risk and reliable assembly technique with consistent sensor-to-sensor distance. Laser-cut alignment holes and fiducial marks allow for a high-precision placement of the hatches with excellent alignment, also between the front- and back-side. The technique has been optimized for the integration of the carrier directly in the heat sinks to further reduce the assembly risk. A mechanical demonstrator of a double-sided, vacuum-compatible p-tracker with minimal material budget inside the acceptance based on MIMOSIS sensors has been integrated with this technique proving the feasibility. The thermal performance has been intensely studied in FEA.

High-yield and low-risk reworking strategies for all critical integration steps have been developed and tested. For sensors that break during integration, the laser hatching technique has been adopted and optimized to remove single sensors glued onto the carrier in a controlled manner and with high precision, without introducing mechanical stress on the other components. The local increase of material budget for the reworked sensor is minimal and the alignment of the new sensor is identical. For the ultra-thin FPCs, reworking is possible when gluing them to a parylene-coated carrier with the double-sided tape by peeling them off at a large angle. The necessary mechanical support during bonding is guaranteed by an integration jig that has been designed.

A detailed sensor integration flow has been proposed. It is driven by the necessity for a plasma activation process and has been optimized for a high reworkability at all steps, and the option to pre-condition the detector. It is a step-by-step assembly guide including a fine-meshed QA. A focus lies also on the identification of companies, institutes, and laboratories to provide the

necessary equipment and infrastructure identified. The necessary tools for the integration have been designed.

A preliminary detector integration flow has been proposed. It is however, due to the status of the detector integration mechanics, not nearly as comprehensive as the sensor integration flow.

## 5.4 Outlook

This thesis serves as the blueprint for the mechanical integration of the MVD. The techniques developed in the course of this thesis can be combined to mechanically integrate a pre-series module, demonstrating the yield and efficiency of the QA measures and integration techniques.

Open questions regarding the different components and the integration have been summarized at the end of every sub-chapter. Results from the probe testing of MIMOSIS-1 are expected soon and will trigger the design of a dedicated, low-mass FPC to power and read out the sensors. The design of the FEB and the implementation of a CBM-compatible readout are work in progress. In parallel, the powering based on FEAST DC/DC converters and the grounding scheme of the detector will be addressed. Here, options of galvanic separation of the heat sinks and piping, *e. g.* by employing dielectric fittings, should be explored. The efforts will converge in the mechanical and electrical integration, and commissioning of a pre-series module of the largest station with geometry *c*, and of a dedicated mMVD module to implement into mCBM by March 2025. The reuse of MVD components in the proposed  $\mu$ -tracker allows for integrating a similar, functional module into mCBM.

The design of the mounting structure and the remote positioning system needs future advice by engineers.

The finalization of the MVD CAD model is work in progress and provides a helpful tool in optimizing the detector integration flow. It will also serve as the basis to update the MVD GEANT model towards realistic material budget estimations.

The laser processing studies presented here can be pushed further as they allow the production of TPG carriers in complex form factors. Also, elaborate 3-dimensional structures can be hatched onto the surface and even inclined planes and controlled height gradients can technically be realized. Studies to improve the surface roughness of the hatched surfaces can be made. Instead of hatching the surface with constant parameters, the hatching depth could be adjusted locally, optimized to reduce mountains and valleys on the surface. The surface profile is a necessary input for this. It can be determined with an optical scan of the surface. The hatching of the sensors can be pushed even further, removing the silicon completely and hatching the top  $\sim 15\ \mu\text{m}$  of the  $30\ \mu\text{m}$  epoxy layer. It needs to be evaluated, whether the adjacent sensors suffer collateral damage during the hatching procedure. While there has been no visible damage in preliminary tests with dummies, it can not be excluded at this point. The final validation of this reworking technique requires further examination with functioning sensors.

After the integration of an mMVD into mCBM and the successful integration of at least one pre-series module, the mass-production of the detector can start. As already discussed in this thesis, a sharing of the workload, *e. g.* of the sensor QA can be beneficial, despite of the added logistics induced by the distribution of hardware and the preparation of the related infrastructure. The MVD will be one of the last detectors to be installed in the CBM cave as the installation and commissioning of both the magnet and the STS have to be finished beforehand.

# A Appendix

## A.1 Ionizing Radiation Doses of the MVD

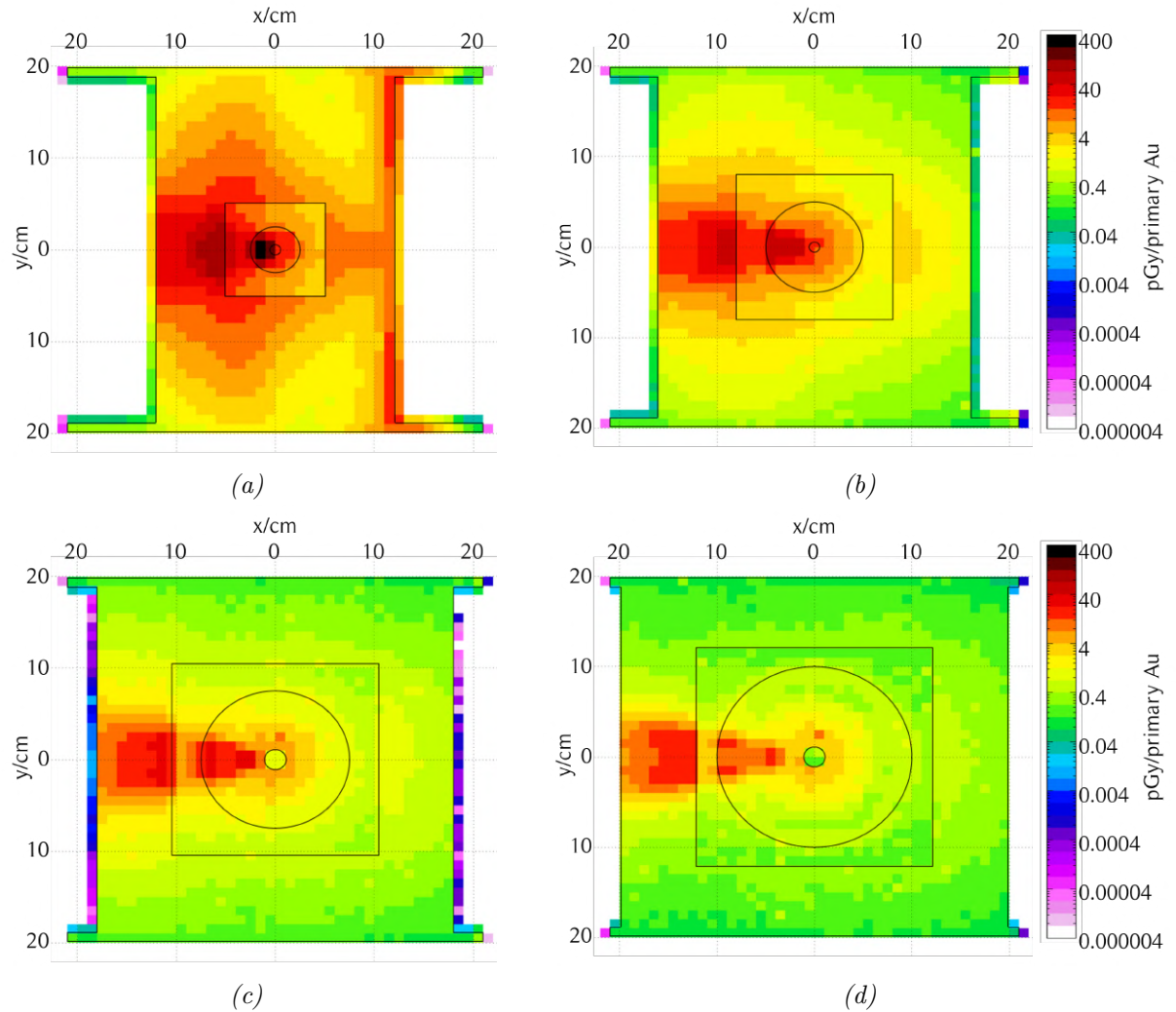


Figure A.1: Ionizing dose per primary ion for the first (a), second (b), third (c), and fourth (d) MVD station, placed 8, 12, 16, and 20 cm downstream of the target, respectively (TR geometry). The doses were simulated with FLUKA for Au – Au collisions with 11 A Gev beam energy at full magnetic field for geometry v20d\_tr. Taken from [84].

## A.2 The Updated MVD CAD Model

A fully parametric CAD model of the MVD with close to final form factors of many components, including also part of the piping, has been set up. The highest feasible level of detail is implemented. The model is work in progress and the current status is presented here.

The new model is a step towards the design freeze of the detector components. The ‘Analyze Interference Among Components’ feature of Autodesk Inventor CAD can be used to spot static collisions of components and mistakes in the design. Using the assembly presentation feature, a dynamical explosion view can be set up. This allows for spotting dynamic collisions between components, *e. g.* during integration or when moving the half-detectors during beam tuning. The sensor and detector integration flow can be dynamically visualized and optimized in this CAD model. The keep-in volumes defined for the collaboration in a CBM Technical Note [54] have been confirmed. The assembly and accessibility of the MVD and target exchange device have to be evaluated. After finalizing the CAD model, it can be translated to a ROOT Geometry File and subsequently be used for realistic material budget evaluations necessary for physics simulations.

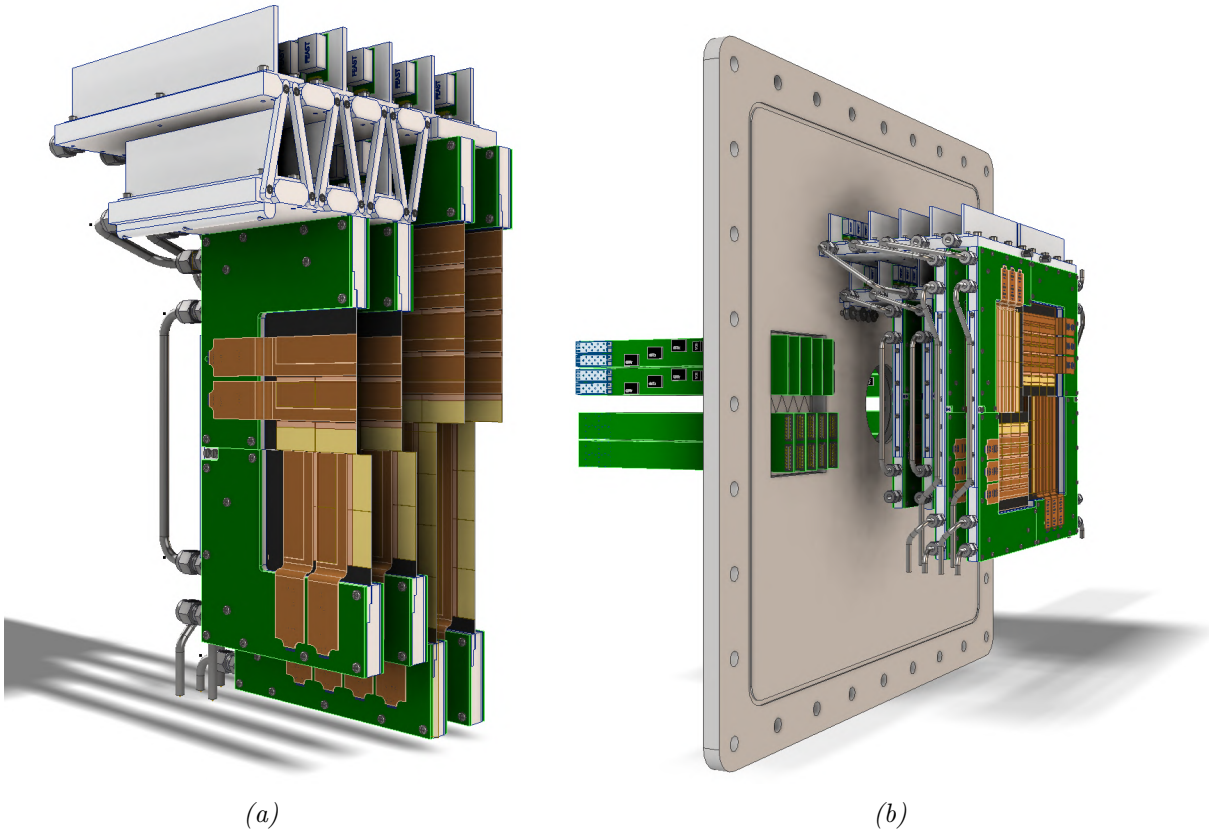


Figure A.2: Current status of the CAD model of the left half-detector, including four half-stations, two top plates, and piping (a). Current status of the CAD model of the MVD, including the half-detectors and the front flange (b).

The starting point of the model is the active part of the detector where the form factors are mostly final. For the parts that are not finalized yet, *s. a.* the layout of the FEB, sufficient keep-out volumes with safety margins are implemented and respected. It is envisioned to use the same ROBs as the STS which are already implemented. The form factor is very different from what was implemented in the last CAD model. The upstream keep-in volumes can be respected regardless. Actively cooled top plates have been designed and space for up to 94 FEAST DC/DC converters is reserved there. A lot of the passive components, especially regarding the

mounting structure, master table and remote positioning system<sup>1</sup> still need to be designed and included subsequently. Also, the pipe and cable routing towards the front flange, including the feedthroughs, needs to be finalized.

The finalization of the remaining detector components and the CAD model is expected by 2025.

### A.2.1 MVD Geometric Acceptance

The geometric acceptance of the MVD can be directly extracted from the CAD model. Four radii can be defined: The smallest distance from the beam axis under which a particle can be detected ('first pixel'), the inner and outer radius under which the MVD covers the full azimuth, and the largest distance from the beam axis under which a particle can be detected ('last pixel'). This is shown in figure A.3.

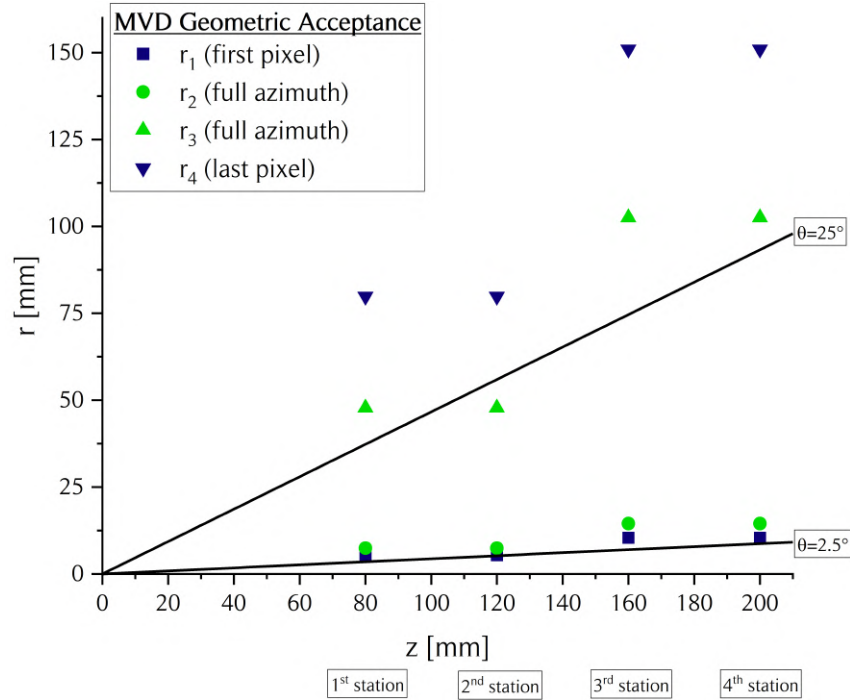


Figure A.3: The geometric acceptance of the four MVD stations in TR geometry. The values shown are the smallest distance from the beam axis under which a particle can be detected, the inner and outer radius under which the MVD covers the full azimuth, and the largest distance from the beam axis under which a particle can be detected. Indicated is also the nominal geometric acceptance of CBM.

## A.3 Integration Support Jig

A dedicated integration jig supporting the carrier inside the acceptance during integration has been designed and produced. The testing and validation is work in progress. The carrier is mounted to the heat sink as the primary support for the integration. The heat sink is then mounted to the integration jig. The jig is a large plate of aluminum with several holes to mount the heat sink and also several support bars. The support bars are produced in an ESD-safe plastic and can be screwed onto the integration jig to locally support the carrier inside the acceptance. The placement of the bars has been optimized to allow for pressing the FPCs onto

<sup>1</sup>These components do not fall into the direct responsibilities of the MVD team. The responsibilities are not assigned yet [54].

the double-sided adhesive tape on the carrier and to ensure a sufficient mechanical support during the bonding process. The handling of the quadrants is also simplified with the integration jig.

The jig has a very simplistic design as it is a single plate with CNC-drilled holes. Several sets of screw holes are placed such that it can be used for all of the MVD integration. The front- and back-side of the quadrants of geometry  $b$  and  $c$  can be integrated with the same jig. Figure A.4 shows the design and the integration of a large carrier with this jig.

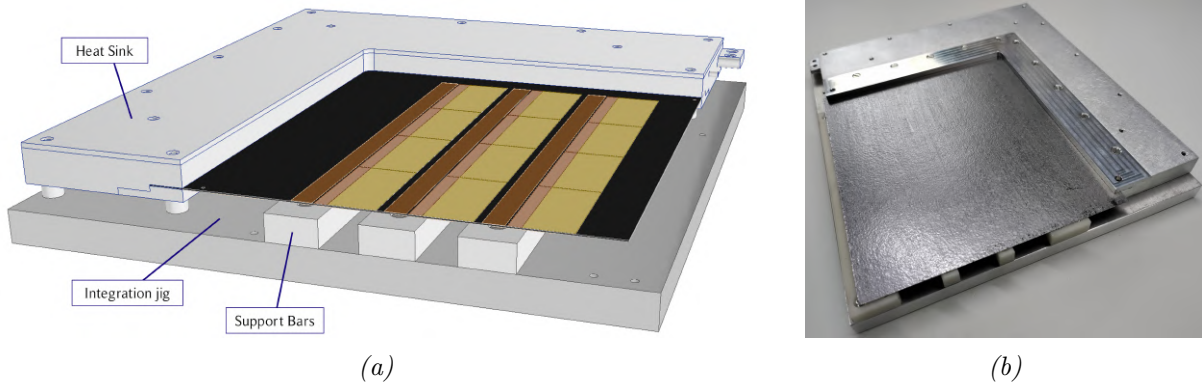


Figure A.4: CAD view of a heat sink mounted onto the integration support jig with support bars placed underneath the carrier to allow for pressing the FPCs onto the double-sided tape (a). Sheet of TPG inside the heat sink, mounted to the integration support jig (b).

## A.4 Optimization of the Gluing Pattern of the Sensors

The pattern of the glue distribution has been optimized on a sheet of unpolished, uncoated TPG using 50  $\mu\text{m}$  silicon dummies. A carrier with hatches is used. The technique takes advantage of the vastly different properties of the materials and their surfaces in the infrared to make the glue distribution visible. Bare TPG is mostly reflective, the hatched surface of TPG has a large emissivity, silicon is very transmissive, and the epoxy again has a large emissivity. Even in a thermalized system, the different materials can be distinguished from each other using infrared photography. Figure 4.3b shows the assembly in visible light.

Six different patterns have been tested, all glued with the same glue (Epo-Tek 301-2) from a single batch in the matter of a few minutes onto a single sheet of TPG. The amount of glue used for every dummy was identical (17  $\mu\text{l}$ , deviations  $\lesssim 10\%$ ). The glue was portioned and distributed with a single-channel micropipette and the amount was cross-checked on a precision scale. The patterns were:

1. Two dots

Two identical dots placed at  $(1/3, 1/2)$  and  $(2/3, 1/2)$ , see also figure A.5.

2. Six dots

Six identical dots placed at  $(1/4, 1/3)$ ,  $(1/2, 1/3)$ ,  $(3/4, 1/3)$ ,  $(1/4, 2/3)$ ,  $(1/2, 2/3)$ , and  $(3/4, 2/3)$ , see also figure A.6.

3. Wide bar

A wide bar placed in the center, see also figure A.7.

4. Bar with four tails

A bar placed in the center with four tails extending to the corners, see also figure A.8.

5. Bar with ten tails

A bar placed in the center with ten tails extending to the long edge and the corners, see also figure A.9.

6. Bar with six tails

A bar placed in the center with six tails extending to the long edge and the corners, see also figure A.10.

The first pattern ('two dots') produces a significant underfill at the corners of the sensor and is not suited. With the second pattern ('six dots'), this is improved, however the gaps in between the dots favor the forming of cavities that could impede the vacuum-compatibility. The third pattern ('wide bar') yields an even distribution over the whole area. However, it is difficult to distribute the glue homogeneously enough by hand and the inhomogeneities remain throughout the curing process. The fourth pattern ('bar with four tails') is relatively simple to distribute, produces however a slight underfill at the long edges. The fifth pattern ('bar with ten tails') is hard to distribute and yields a very inconsistent distribution while also favoring the forming of cavities. The sixth pattern ('bar with six tails') is simple to distribute and yields an even distribution underneath the whole area of the sensor. It has therefore been chosen as the final pattern.

This study was focused on the optimization of the gluing pattern. The amount of glue used was not sufficient for the unpolished surface. This translates to a slight underfill for all options which is present in all cured samples. The amount can be improved and optimized for polished, parylene-coated TPG, using the identified pattern ('bar with six tails'). If necessary, cavities can also be reduced by curing the samples either in vacuum or at high pressures.

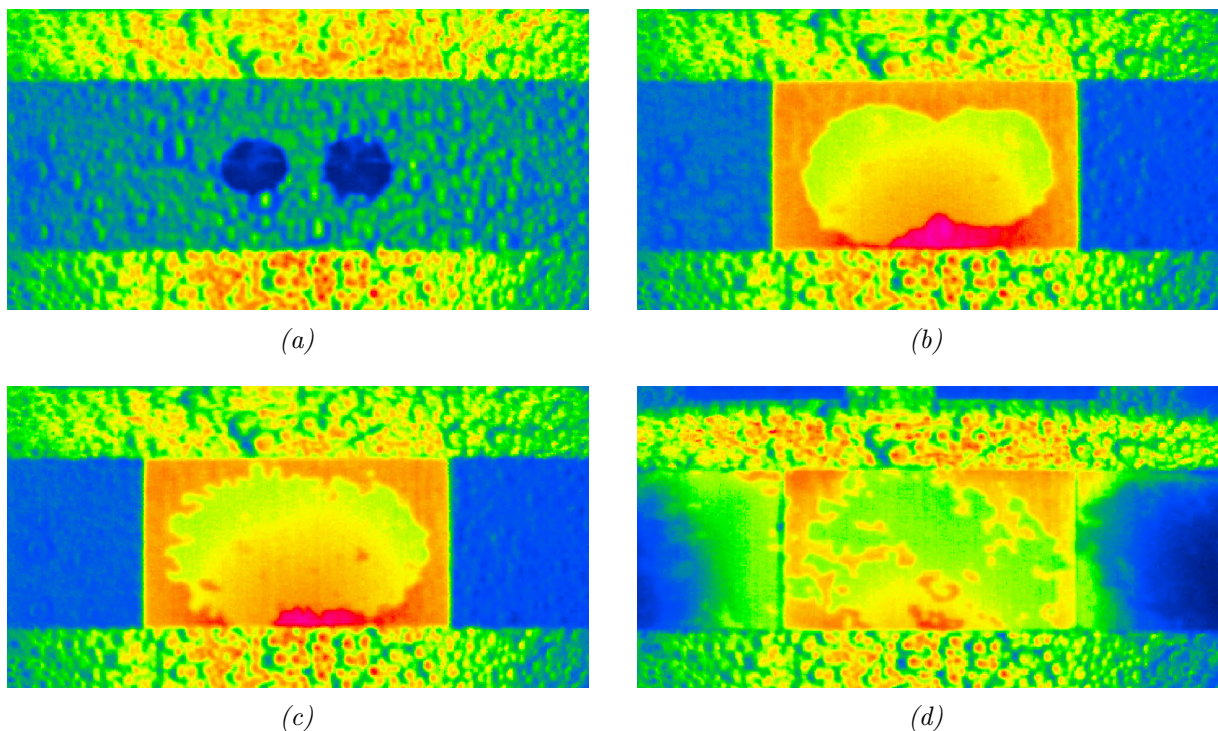


Figure A.5: Infrared photographs of the glue distribution (option 1) in a hatch of an unpolished, uncoated sheet of TPG. The pictures show the glue distribution before placing a  $50\ \mu\text{m}$  silicon dummy (a), 2 seconds (b), 2 minutes (c), and 30 hours after placement (d).

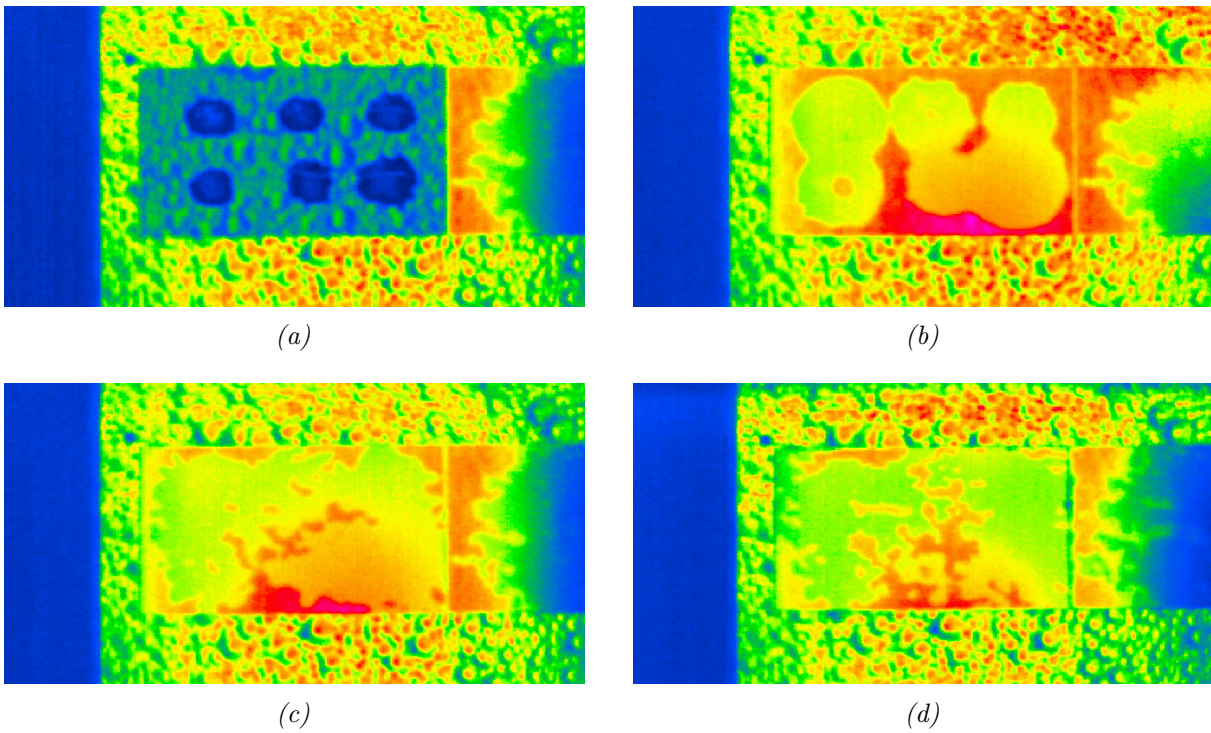


Figure A.6: Infrared photographs of the glue distribution (option 2) in a hatch of an uncoated, unpolished sheet of TPG. The pictures show the glue distribution before placing a  $50\ \mu\text{m}$  silicon dummy (a), 2 seconds (b), 2 minutes (c), and 30 hours after placement (d).

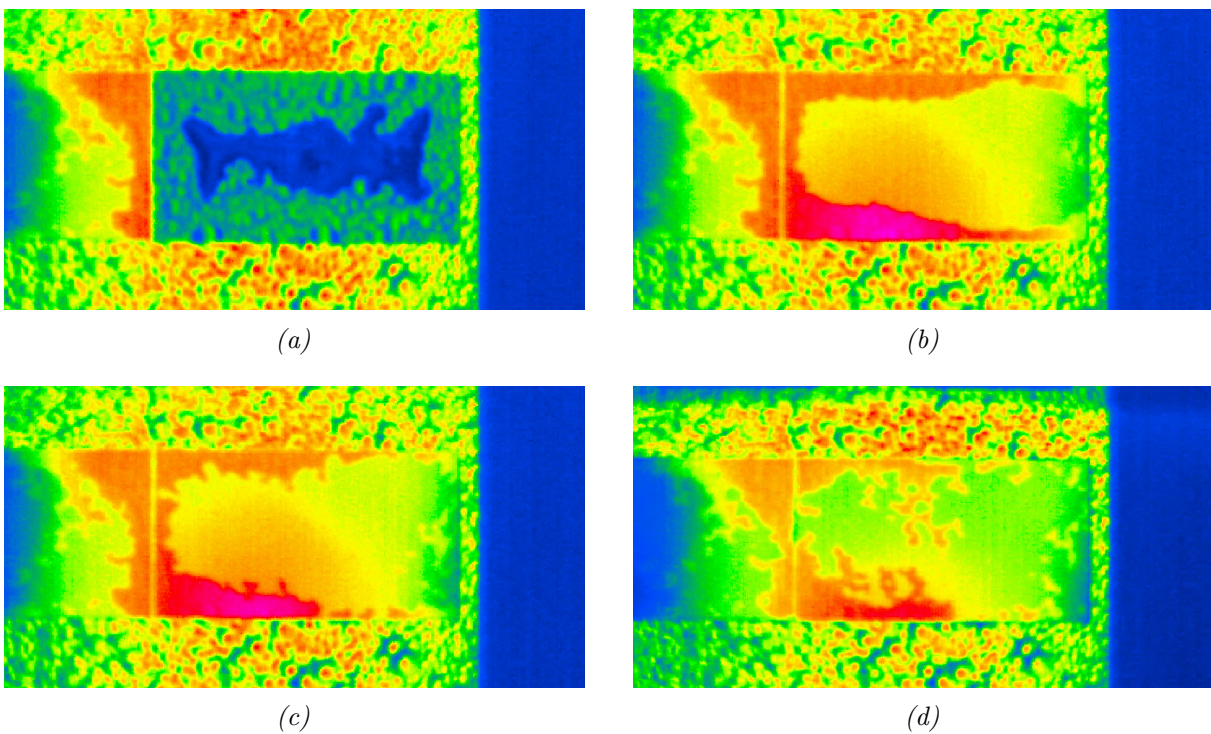


Figure A.7: Infrared photographs of the glue distribution (option 3) in a hatch of an uncoated, unpolished sheet of TPG. The pictures show the glue distribution before placing a  $50\ \mu\text{m}$  silicon dummy (a), 2 seconds (b), 2 minutes (c), and 30 hours after placement (d).

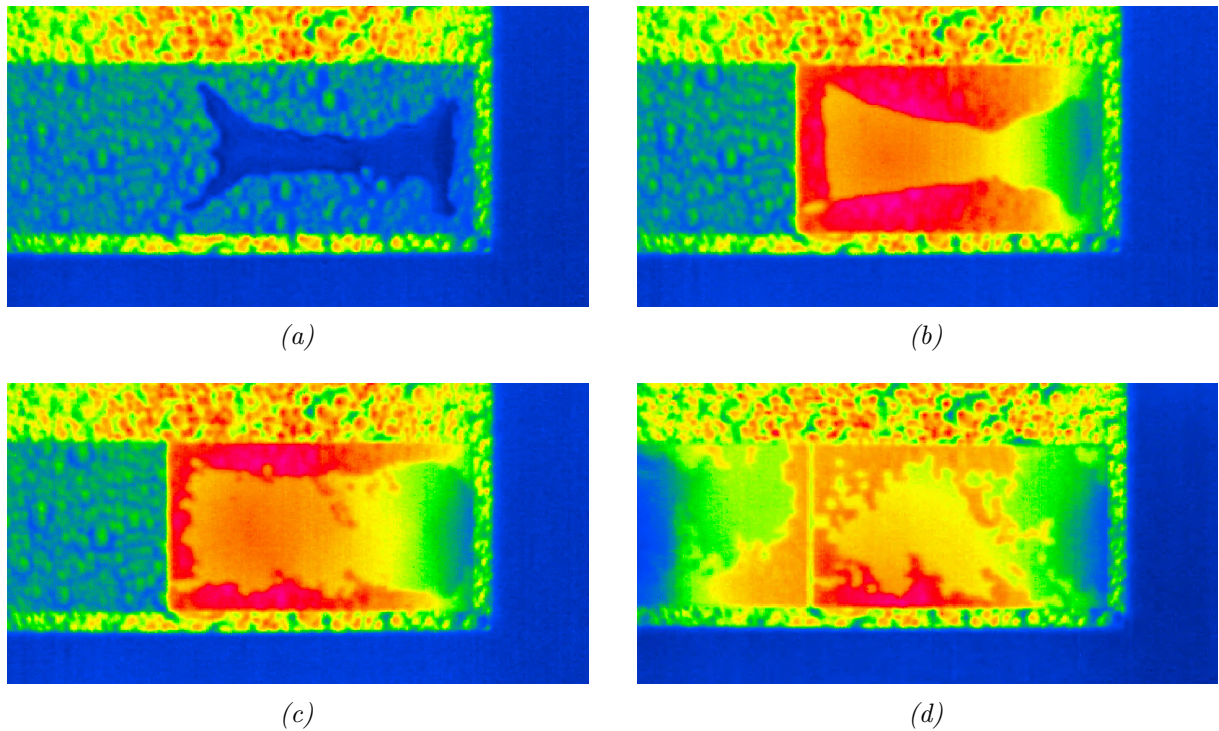


Figure A.8: Infrared photographs of the glue distribution (option 4) in a hatch of an uncoated, unpolished sheet of TPG. The pictures show the glue distribution before placing a  $50\ \mu\text{m}$  silicon dummy (a), 2 seconds (b), 2 minutes (c), and 30 hours after placement (d).

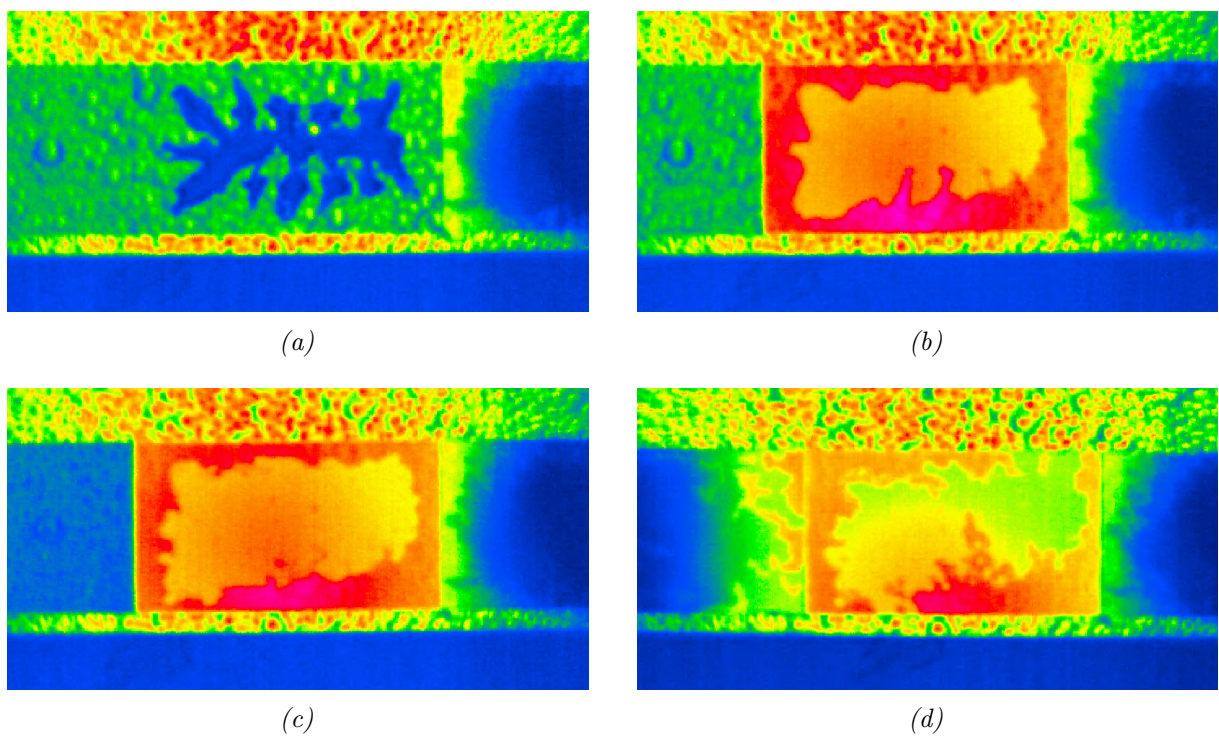


Figure A.9: Infrared photographs of the glue distribution (option 5) in a hatch of an uncoated, unpolished sheet of TPG. The pictures show the glue distribution before placing a  $50\ \mu\text{m}$  silicon dummy (a), 2 seconds (b), 2 minutes (c), and 30 hours after placement (d).

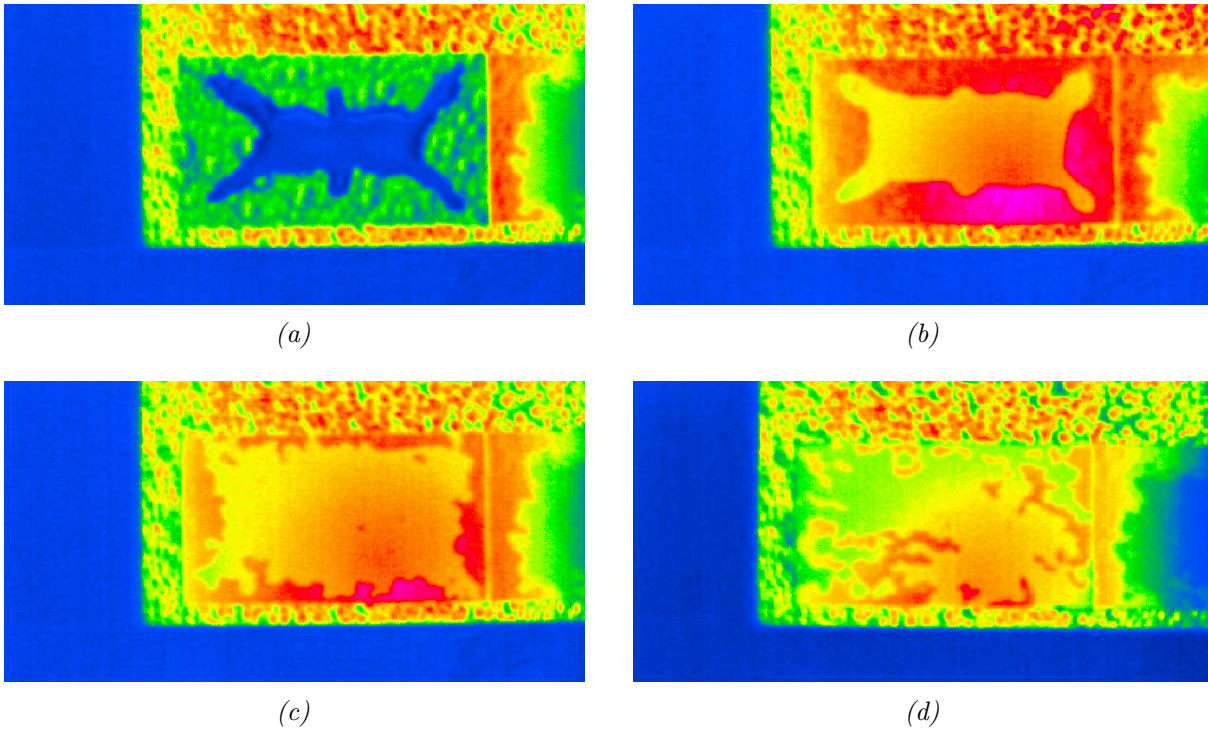


Figure A.10: Infrared photographs of the glue distribution (option 6) in a hatch of an uncoated, unpolished sheet of TPG. The pictures show the glue distribution before placing a  $50\ \mu\text{m}$  silicon dummy (a), 2 seconds (b), 2 minutes (c), and 30 hours after placement (d).

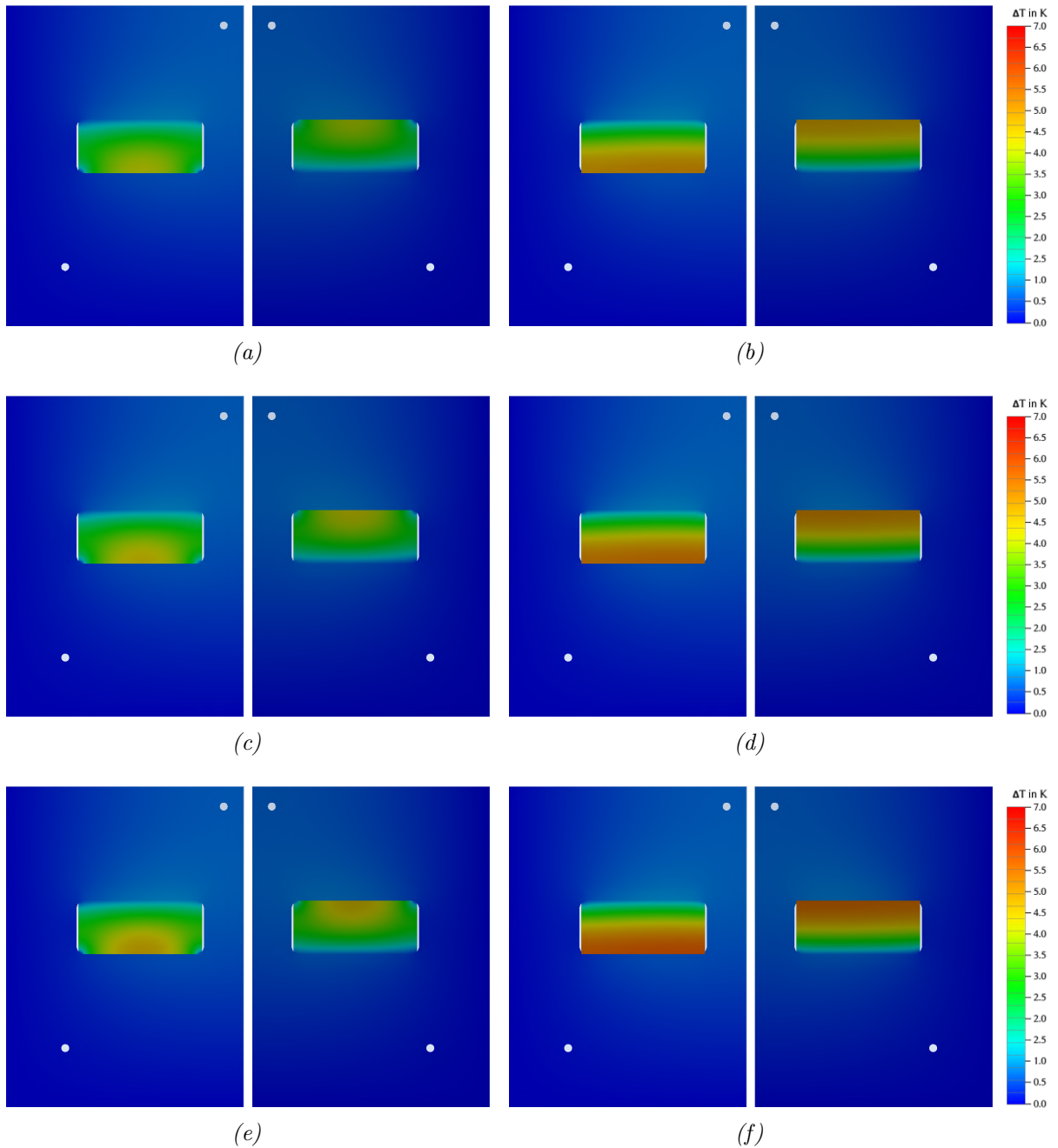
A.5 Thermal Simulations of the Proposed  $\mu$ -Tracker Design

Figure A.11: Temperature distributions on the carrier and sensors of the front- and back-side (left and right, respectively) of the proposed  $\mu$ -tracker design with a  $380\ \mu\text{m}$  thick carrier. Coolant temperature of  $-20^\circ\text{C}$  (sensor corners glued (a) and sensor corners not glued (b)),  $0^\circ\text{C}$  (sensor corners glued (c) and sensor corners not glued (d)), and  $+20^\circ\text{C}$  (sensor corners glued (e) and sensor corners not glued (f)). Simulated with In-CAD Autodesk Inventor Nastran FEA (nonlinear stationary heat transfer).

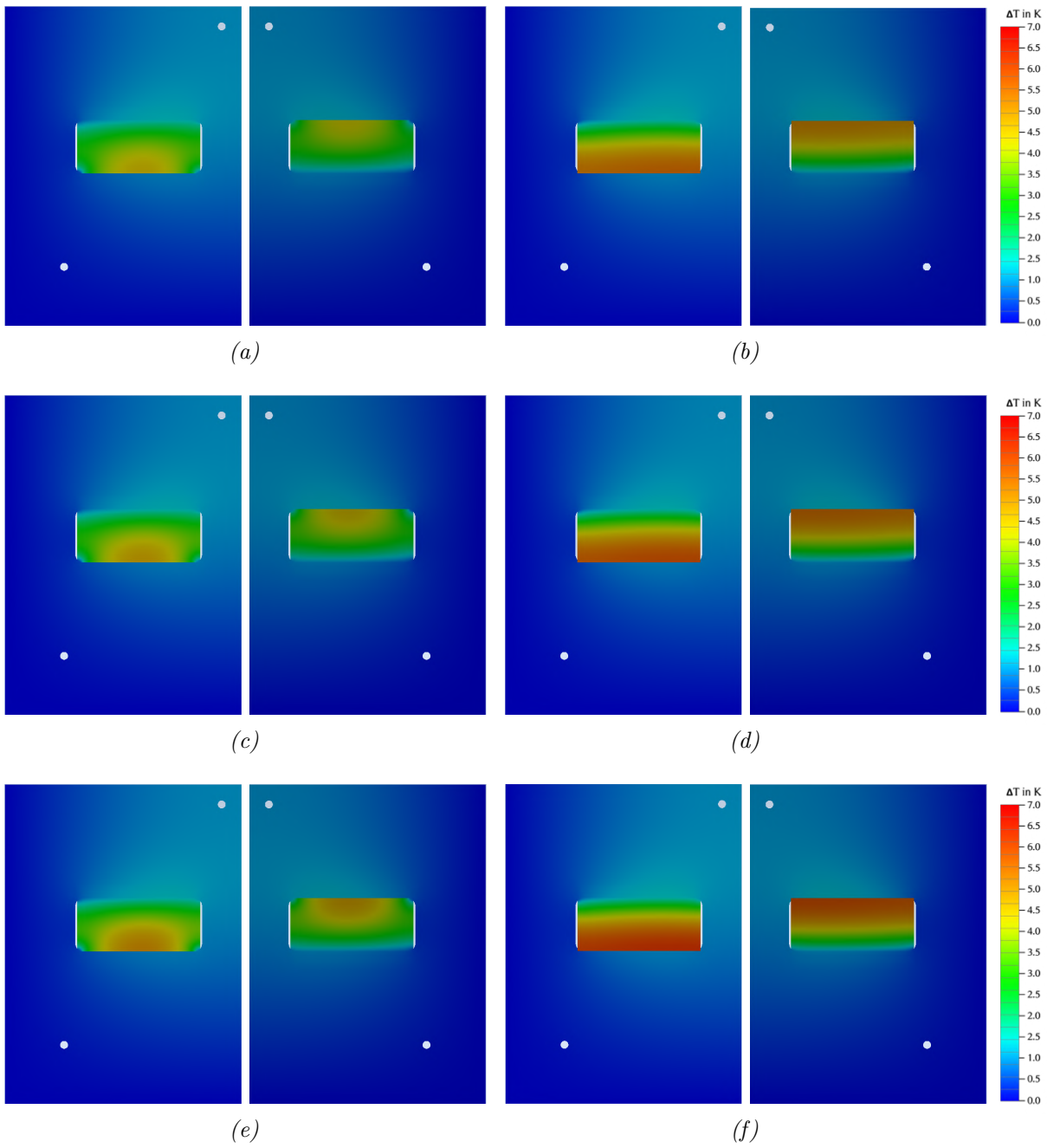


Figure A.12: Temperature distributions on the carrier and sensors of the front- and back-side (left and right, respectively) of the proposed  $\mu$ -tracker design with a  $250\ \mu\text{m}$  thick carrier. Coolant temperature of  $-20^\circ\text{C}$  (sensor corners glued (a) and sensor corners not glued (b)),  $0^\circ\text{C}$  (sensor corners glued (c) and sensor corners not glued (d)), and  $+20^\circ\text{C}$  (sensor corners glued (e) and sensor corners not glued (f)). Simulated with In-CAD Autodesk Inventor Nastran FEA (nonlinear stationary heat transfer).

## A.6 Radiolysis Effects on the Coolant

A generous upper limit for the effects of radiolysis in the coolant is estimated in this chapter. Active cooling is placed only in the periphery and due to the fixed target geometry of CBM, the most exposed coolant volume only sees 20% of the ionizing and non-ionizing dose of the most exposed sensor, see figure A.1a. The dose is scaled up such that the most exposed sensor sees its EOL dose (5 Mrad ionizing and  $7 \times 10^{13}$  n<sub>eq</sub>/cm<sup>2</sup> non-ionizing), which it will accumulate in a CBM year. The anisotropy in the radiation field introduced by the dipole field is taken into account when calculating the so-called dilution factor.

Only a fraction of the total coolant is exposed to radiation. This reduces the total dose on the coolant by the dilution factor, given by the ratio of the exposed to the total volume. The exposed volume can be extracted from the CAD model of the detector and has to be weighted with the relative exposure, see A.1a. The volumes of the connecting pipes and coolant reservoir outside the MVD box have to be estimated, see A.1b. The dilution factor amounts to 0.01. If necessary, it can be reduced even further by increasing the volume of the reservoir. The coolant is shielded by the piping and heat sinks, reducing the total dose even further. This is not taken into account here to conservatively approach the damage. The damage is then determined by:

1. The total dose  
1000 krad (ionizing),  $1.4 \times 10^{13}$  n<sub>eq</sub>/cm<sup>2</sup> (non-ionizing) per CBM year
2. The dilution factor  
0.01
3. Shielding effects  
Not taken into account

Table A.1: Coolant volumes exposed to ionizing radiation with their relative exposures and respective magnitudes. The relative exposure of the most exposed volume is set to 1 (a). Components adding to the total coolant volume and their respective magnitudes (b). The volume of the upstream piping and the chiller reservoir have been estimated, all volumes upstream have been extracted from the CAD models of the components.

Half-station	Relative exposure	Volume in ml
1	Left	1
	Right	0.1
2	Left	0.5
	Right	0.03
3	Left	0.25
	Right	0.01
4	Left	0.15
	Right	0.003

(a)

Component	Volume in ml
Heat sinks	520
Top plates	70
Piping $z > 0$	150
Piping $z < 0$	2000
Chiller	10000

(b)

The damage scales linearly with the dose in this range and is almost completely determined by ionizing radiation due to the lack of internal structure in fluids. The effects of  $10^{12}$  n<sub>eq</sub>/cm<sup>2</sup> of non-ionizing radiation equal approximately those of 1 krad ionizing radiation [85]. The yield of radiolysis is typically characterized by the G-value, which is the number of dissociated molecules per 100 eV of absorbed ionizing radiation. The G-values of Novec 649, DI water and glycol/water are listed in table A.2.

Table A.2: *G*-values, their respective radiolysis yield per krad by weight, and overall radiolysis yield per CBM year of Novec 649, DI water and glycol/water (50/50, by weight). Values taken from [85–87]. The *G*-value of Novec 649 has not been measured but the value given here is a very generous upper limit. The *G*-value of water varies strongly with its purity. For the *G*-value of glycol/water, the value of pure ethylene glycol is taken as the upper limit as water is formed during glycol radiolysis anyway. The actual value for glycol/water is around 15/100 eV [88].

Coolant	G-Value in 1/100 eV	Yield in ppm <sub>wt.</sub> /krad	Yield per CBM Year
Novec 649	25	8.2	83 mg (140 $\mu$ l)
DI Water	3.7	0.07	1 mg (1 $\mu$ l)
Glycol/Water	51	3.3	33 mg (36 $\mu$ l)

The very generous upper limit of the overall radiolysis yield per CBM year is almost negligible and hence radiolysis is not critical for all coolant options. The temperature dependence of the radiolysis yield is not relevant in the small operation window of the MVD. Impurities are, however, driving as they can produce radicals which might corrode the piping and heat sinks in follow-up reactions.

For pure Novec 649, radiolysis is not a problem at MVD doses. Water, however, can complicate radiolysis processes due to follow-up reactions. Hydrolysis, as discussed previously, is a much more serious concern and a leak-tight system is strongly required.

In pure water, most of the oxygen and hydrogen initially produced will recombine (the initial *G*-value is 5.7 [89] and reduces to 3.6 quickly [86]). The presence of other molecules can strongly influence this and a dependence on the oxygen content has been observed [90]. It is known from plentiful experience with water cooling in accelerators and detectors that water radiolysis can be dealt with rather easily by inline rectification and dose rates in the order of 0.1 krad/h are typically not critical [91]. For the CBM MVD, less than 0.01 krad/h (*i. e.* 10 krad/2 months) including dilution are expected. The upgraded ALICE Inner Tracking System *e. g.* uses water as coolant and has similar doses on the coolant of up to 270 krad per layer (EOL dose in 6 – 10 years of operation) [72, 92].

In glycol/water mixtures, radiolysis produces numerous different new chemicals, *s. a.* hydrogen and oxygen, hydrogen peroxide, several aldehydes and acetates with yields depending on the mixture and dose rate [93]. Aluminum is chemically resistant to all of those [94]. The explosion risk of the H<sub>2</sub> and O<sub>2</sub> mixture makes glycol/water unusable as a bi-phase coolant. In mono-phase applications, this can be dealt with by inline rectification. Nonetheless, the high *G*-value of liquid ethylene glycol of 51 [87] and the complicated radiochemistry with a multitude of intermediate reactions and different final products call for a dedicated monitoring system of the coolant's purity for the MVD.

# List of Figures

1.1	Layout of FAIR with the two ring accelerators SIS 18 and SIS 100, and CBM indicated. The sub-objectives of the staged completion are color-coded [2]. . . .	1
1.2	CAD view of the projected day one experimental setup of the CBM detector in the so-called electron setup for SIS 100, including also the HADES detector upstream [5].	2
1.3	Total number of reconstructable Monte Carlo $\pi^+$ produced in 10 000 central Au+Au collisions at 4.9 A GeV (minimum 3 hits in the CBM silicon layers), reconstructable $\pi^+$ using the MVD and STS, and reconstructable $\pi^+$ using only the STS, as a function of the laboratory momentum [7]. . . . .	3
1.4	Render of the current status of the latest MVD CAD model. The beam comes from the left, passes the target exchange device, and hits the target stationed at the center of the front flange. Included is also the vacuum interface and beampipe of the STS. The mounting structure of the MVD is not implemented yet. For a detailed discussion of the model, see also appendix A.2. . . . .	6
2.1	CAD view of the front-side (a) and back-side (b) of an MVD quadrant of geometry <i>c</i> including all the hardware components introduced in this chapter. . . . .	7
2.2	300 $\mu\text{m}$ thick MIMOSIS-1 sensor held with a vacuum pick-up tool. The active pixel matrix is visible in the upper part of the sensor and the passive digital part is visible at the lower part of the sensor [13]. . . . .	8
2.3	Detection efficiency (a) and spatial resolution (b) as a function of the threshold for MIMOSIS-1 AC-pixels for two different doping profiles of the epitaxial layer ('standard' and 'p-stop') before irradiation, after 20%, and after 100% of the EOL ionizing dose. All measurements were taken at +15 $^{\circ}\text{C}$ [10]. . . . .	9
2.4	Measured global mean detection threshold (GMDT, indicated by symbols) and fixed pattern noise (FPN, indicated by vertical bars) as a function of the threshold set on the on-chip DACs for MIMOSIS-1 AC-pixels (a) of two different sensors before irradiation, after 20%, and after 100% of the EOL ionizing dose, respectively, and (b) of a single chip after 20% of the EOL ionizing dose for different temperatures [15].	9
2.5	Power consumption (digital part) of MIMOSIS-1 (simulated, before irradiation, after EOL irradiation) for different occupancies with all data outputs active (a). The area of interest of the occupancy extends to $\sim 1000$ pixels per frame [17–19]. Efficiency of FEAST DC/DC converter (variable input voltage, 1.8 V output, at 18 $^{\circ}\text{C}$ ) for different output loads (b), taken from [16]. . . . .	10
2.6	Picture of two bonding pads on MIMOSIS-1, one before (a), and one after (b) the etching procedure using diluted phosphoric acid as cleaning agent. . . . .	12
2.7	Picture of a sheet of bare, unpolished TPG (a). 3D-scan of the surface of a sheet of bare, unpolished TPG (b). . . . .	14
2.8	Water droplets on polished, uncoated and polished, parylene-coated TPG, demonstrating the hydrophobic nature of the coating (a). Glass plates glued onto polished, parylene-coated TPG using RAL-247 with different amounts of wetting agent (b). Air bubbles are visible that are caused by an insufficient surface wetting of the glue.	17
2.9	Infrared photos of the glue distribution on a polished, uncoated TPG carrier. (a) shows the distribution of the glue before placing the dummy, (b) two seconds and (c) two minutes after placing the dummy, and (d) after curing. . . . .	18

2.10	Infrared photos of the glue distribution on a polished, parylene-coated TPG carrier. (a) shows the distribution of the glue before placing the dummy, (b) two seconds and (c) two minutes after placing the dummy, and (d) after curing. . . . .	19
2.11	Double-sided kapton tape (top cover layer still attached) glued onto a sheet of polished TPG (a). The top cover layer is removed and the gluing can be visually inspected (b). A thin, partly single- / partly double-layer FPC is glued on top. The tape is still visible underneath the single-layer, allowing for an optical QA. . . . .	21
2.12	Double-layer FPC for 4 MIMOSA-26 assembled from two single-layer FPCs. . . . .	24
2.13	CAD view of the heat sink version 3 a (geometry <i>c</i> ), including the screwed clamp fixating the carrier that sits on the balcony, and the NPT in- and outlet fittings (a). Cross-sectional CAD view of the cooling channel of the heat sink version 3 a (geometry <i>c</i> ), including the vacuum-brazed cover plate (b). . . . .	28
2.14	Half-station (geometry <i>c</i> ) assembled from two heat sinks of the latest version 3 a and b. The deviations from perfect flatness are smaller than 0.05 mm and not visible on the planar marble table. . . . .	29
3.1	Assembly of a large top plate with the fittings and the FEAST DC/DC converters, including their cooling fins (a). Assembly of the top plates for a half-detector, including crossbars to strengthen the assembly against shear forces (b). . . . .	31
3.2	Pipe inside a 3D-printed jig to confirm the bend and cut (a). Assembly from two shorted manifolds with 22 threads to confirm the compatibility of semi-rigid version of Loctite Ablestik 45 as the thread sealant with Novec 649 (b). . . . .	34
3.3	CAD view of the current layout of the service feedthroughs on the MVD front flange (a). CAD view of the conceptual idea of the MVD master table mounted to the front flange including a dummy remote positioning system for the detector (b). . . . .	34
4.1	Sketch of the cross-section of a laser vaporization cut indicating the ablation depth, the laser beam shape and diameter, the isolation width, the cut definition ( <i>i. e.</i> the position of the isolation width <i>w. r. t.</i> the line from the input sketch), and the conical shape along the edge of the cut (opening angle $\lesssim 10^\circ$ ) which results from the beam shape and scan field parallax effects ( <i>i. e.</i> the tilt of the laser). The dimensions and angles are not to scale. . . . .	43
4.2	Laser processed TPG with different structures (a): $5 \times 5 \text{ mm}^2$ squares, separated by a bridge of $100 \mu\text{m}$ (cut); circles with diameters of 8, 4, 2 and 1 mm (cut); CBM-MVD lettering (hatch). 3D-scan of the $4 \times 8$ square pattern ( $5 \times 5 \text{ mm}^2$ ) seen in figure 4.2a, taken with a digital microscope (b). The height is indicated by the colors. . . . .	43
4.3	Laser processed TPG: Hatches with MIMOSIS form factor and depth of $50 \mu\text{m}$ . The two fiducial marks for the front- / back-side alignment (diameter: 1 mm) are indicated as well as one of the $\sim 70 \mu\text{m}$ bridge separating the hatches. Details of the dimensions are listed in table 4.2 (a). Silicon dummies with MIMOSIS form factor (thinned to $50 \mu\text{m}$ ) placed in the hatches. . . . .	45
4.4	MIMOSIS-1 sensors (thinned to $60 \mu\text{m}$ ) placed in TPG hatches. . . . .	46
4.5	CAD view of the front- (a) and back-side (b) of the proposed $\mu$ -tracker design. . . . .	47
4.6	Front-side of the mechanical demonstrator of the proposed $\mu$ -tracker inside a heat sink (a), and an enlarged view on the corner of the silicon dummy, which is glued into a tiny hatch in the surface (b). The radius of the curvature is 2 mm, highlighting the precision of the laser vaporization cutter. . . . .	48

4.7	Aluminum carrier for sensor hatching studies: Three MIMOSA-26 sensors, one with $5 \times 5 \text{ mm}^2$ square hatches of different depths and a $7 \times 21 \text{ mm}^2$ hatch (top left). The two adjacent MIMOSA-26 sensors are not hatched. A metalized, thinned dummy with MIMOSIS form factor hatched down completely with a small, delaminated piece (a). 3D-scan of a $5 \times 5 \text{ mm}^2$ square hatch on a sensor with optimized settings, taken with a digital microscope (b). The noticeable global gradient in the height profile results from the natural curvature of the sensor which is caused by internal stress and is still present after gluing. . . . .	51
4.8	A metalized dummy sandwiched between two bare silicon dummies, all placed inside sensor hatches, before (a) and after (b) hatching it down. The CMOS and metalization structures are still visible after the hatch. . . . .	51
4.9	Peeling off a single-layer FPC that was glued with double-sided adhesive tape from an uncoated (a), and a parylene-coated (b), polished sheet of TPG. . . . .	52
A.1	Ionizing dose per primary ion for the first (a), second (b), third (c), and fourth (d) MVD station, placed 8, 12, 16, and 20 cm downstream of the target, respectively (TR geometry). The doses were simulated with FLUKA for Au – Au collisions with 11 A Gev beam energy at full magnetic field for geometry v20d_tr. Taken from [84]. . . . .	63
A.2	Current status of the CAD model of the left half-detector, including four half-stations, two top plates, and piping (a). Current status of the CAD model of the MVD, including the half-detectors and the front flange (b). . . . .	64
A.3	The geometric acceptance of the four MVD stations in TR geometry. The values shown are the smallest distance from the beam axis under which a particle can be detected, the inner and outer radius under which the MVD covers the full azimuth, and the largest distance from the beam axis under which a particle can be detected. Indicated is also the nominal geometric acceptance of CBM. . . . .	65
A.4	CAD view of a heat sink mounted onto the integration support jig with support bars placed underneath the carrier to allow for pressing the FPCs onto the double-sided tape (a. Sheet of TPG inside the heat sink, mounted to the integration support jig (b). . . . .	66
A.5	Infrared photographs of the glue distribution (option 1) in a hatch of an unpolished, uncoated sheet of TPG. The pictures show the glue distribution before placing a $50 \mu\text{m}$ silicon dummy (a), 2 seconds (b), 2 minutes (c), and 30 hours after placement (d). . . . .	67
A.6	Infrared photographs of the glue distribution (option 2) in a hatch of an uncoated, unpolished sheet of TPG. The pictures show the glue distribution before placing a $50 \mu\text{m}$ silicon dummy (a), 2 seconds (b), 2 minutes (c), and 30 hours after placement (d). . . . .	68
A.7	Infrared photographs of the glue distribution (option 3) in a hatch of an uncoated, unpolished sheet of TPG. The pictures show the glue distribution before placing a $50 \mu\text{m}$ silicon dummy (a), 2 seconds (b), 2 minutes (c), and 30 hours after placement (d). . . . .	68
A.8	Infrared photographs of the glue distribution (option 4) in a hatch of an uncoated, unpolished sheet of TPG. The pictures show the glue distribution before placing a $50 \mu\text{m}$ silicon dummy (a), 2 seconds (b), 2 minutes (c), and 30 hours after placement (d). . . . .	69
A.9	Infrared photographs of the glue distribution (option 5) in a hatch of an uncoated, unpolished sheet of TPG. The pictures show the glue distribution before placing a $50 \mu\text{m}$ silicon dummy (a), 2 seconds (b), 2 minutes (c), and 30 hours after placement (d). . . . .	69

A.10	Infrared photographs of the glue distribution (option 6) in a hatch of an uncoated, unpolished sheet of TPG. The pictures show the glue distribution before placing a 50 $\mu\text{m}$ silicon dummy (a), 2 seconds (b), 2 minutes (c), and 30 hours after placement (d). . . . .	70
A.11	Temperature distributions on the carrier and sensors of the front- and back-side (left and right, respectively) of the proposed $\mu$ -tracker design with a 380 $\mu\text{m}$ thick carrier. Coolant temperature of $-20^\circ\text{C}$ (sensor corners glued (a) and sensor corners not glued (b)), $0^\circ\text{C}$ (sensor corners glued (c) and sensor corners not glued (d)), and $+20^\circ\text{C}$ (sensor corners glued (e) and sensor corners not glued (f)). Simulated with In-CAD Autodesk Inventor Nastran FEA (nonlinear stationary heat transfer).	71
A.12	Temperature distributions on the carrier and sensors of the front- and back-side (left and right, respectively) of the proposed $\mu$ -tracker design with a 250 $\mu\text{m}$ thick carrier. Coolant temperature of $-20^\circ\text{C}$ (sensor corners glued (a) and sensor corners not glued (b)), $0^\circ\text{C}$ (sensor corners glued (c) and sensor corners not glued (d)), and $+20^\circ\text{C}$ (sensor corners glued (e) and sensor corners not glued (f)). Simulated with In-CAD Autodesk Inventor Nastran FEA (nonlinear stationary heat transfer).	72

# List of Tables

1.1	Number of sensors per quadrant for the different MVD stations [1]. . . . .	5
2.1	Form factors of the carriers of geometry $b$ and $c$ as stated in the TDR and the updated values found in the context of this thesis. . . . .	14
2.2	Properties of the adhesives selected for the gluing of the sensors [1, 29–34]. . . . .	17
2.3	Properties of the high-viscosity glue and the double-sided tape selected for the gluing of the FPCs [39–43]. . . . .	20
2.4	The different layers, the respective thickness and fill factor, and material budget of the low-mass PRESTO FPC designed for the MIMOSA-26 sensor [1]. . . . .	22
2.5	Properties of a low-mass MVD FPC according to the standard design rules by ILFA [46]. The feature size of 100 $\mu\text{m}$ (single-ended) and 300 $\mu\text{m}$ (differential; two single-ended lines plus additional space to avoid cross-talk) is slightly larger than the minimum realizable with ILFA (75 $\mu\text{m}$ [46]) and the low-mass MIMOSA-26 FPC designed at IKF (80 $\mu\text{m}$ [1]), and might still have to be optimized. The width of the power traces is determined requiring an ohmic resistance of $\sim 100\text{ m}\Omega$ for a 10 cm long trace of 12 $\mu\text{m}$ copper. The width of the GND is double that of the power traces. . . . .	23
2.6	The current understanding of the necessary number of traces on the FPC and their contribution to the total width of the FPC serving two sensors based on the feature size stated in table 2.5. . . . .	24
3.1	Properties of Novec 649, deionized water and ethylene glycol/water (50/50, by weight). Values taken from [60, 67–69]. See table A.2 for the discussion on radiation hardness. . . . .	39
3.2	Proposed parameters of the MVD cooling setup based on the constraints presented in this chapter. . . . .	40
4.1	Parameters of the laser vaporization cutter optimized for cutting up to 500 $\mu\text{m}$ of TPG and hatching 50 $\mu\text{m}$ deep into TPG. . . . .	43
4.2	Dimensions set on the laser vaporization cutter for a set of hatches and the bridges between adjacent hatches guaranteeing the sensor-to-sensor distance, and their actual values as measured with a digital microscope. . . . .	46
4.3	Parameters of the thermal simulations for the proposed low-material budget $\mu$ -tracker designs [23, 79]. The power densities have been estimated based on figure 2.5a. . . . .	49
4.4	The temperature difference between the hottest point on the matrix and the coldest point on the carrier for several configurations and operation temperatures of the proposed $\mu$ -tracker design. The values have been simulated with In-CAD Autodesk Inventor Nastran FEA (nonlinear stationary heat transfer). The most important simulation parameters can be found in table 4.3. . . . .	49

A.1	Coolant volumes exposed to ionizing radiation with their relative exposures and respective magnitudes. The relative exposure of the most exposed volume is set to 1 (a). Components adding to the total coolant volume and their respective magnitudes (b). The volume of the upstream piping and the chiller reservoir have been estimated, all volumes upstream have been extracted from the CAD models of the components. . . . .	73
A.2	G-values, their respective radiolysis yield per krad by weight, and overall radiolysis yield per CBM year of Novec 649, DI water and glycol/water (50/50, by weight). Values taken from [85–87]. The G-value of Novec 649 has not been measured but the value given here is a very generous upper limit. The G-value of water varies strongly with its purity. For the G-value of glycol/water, the value of pure ethylene glycol is taken as the upper limit as water is formed during glycol radiolysis anyway. The actual value for glycol/water is around 15/100 eV [88]. . . . .	74

# Bibliography

- [1] The CBM Collaboration. *Technical Design Report for the CBM Micro Vertex Detector*. Tech. rep. Dec. 2021. URL: [https://edms.cern.ch/ui/file/2738980/LATEST/MVD\\_TDR\\*.pdf](https://edms.cern.ch/ui/file/2738980/LATEST/MVD_TDR*.pdf).
- [2] P. Gasik. *Private Communication*. 2024.
- [3] B. Friman et al. *The CBM Physics Book*. 2011. ISBN: 9783642132926.
- [4] P. Gasik. *TC Status (Slides shown on 4<sup>2</sup><sup>nd</sup> CBM Collaboration Meeting)*. Sept. 2023. URL: [https://indico.gsi.de/event/17147/contributions/74341/attachments/44977/63584/gasik\\_42CM\\_Welcome.pdf](https://indico.gsi.de/event/17147/contributions/74341/attachments/44977/63584/gasik_42CM_Welcome.pdf).
- [5] P. Dahm. *Private Communication*. 2024.
- [6] T. Galatyuk. “Di-electron spectroscopy in HADES and CBM : from p + p and n + p collisions at GSI to Au + Au collisions at FAIR”. PhD thesis. Goethe-University Frankfurt, 2009.
- [7] J. E. Andary. *Private Communication*. 2024.
- [8] N. Wermes. *Pixel Vertex Detectors*. 2006. URL: <https://arxiv.org/abs/physics/0611075v1>.
- [9] L. Collaboration. *LHCb VELO Upgrade Technical Design Report*. Tech. rep. 2013. URL: <https://cds.cern.ch/record/1624070>.
- [10] H. Darwish et al. “Tolerance of the MIMOSIS-1 CMOS Monolithic Active Pixel Sensor to ionizing radiation”. In: JINST 18.06 (June 2023). DOI: 10.1088/1748-0221/18/06/C06013. URL: <https://dx.doi.org/10.1088/1748-0221/18/06/C06013>.
- [11] M. Koziel et al. “Vacuum-compatible, ultra-low material budget Micro-Vertex Detector of the compressed baryonic matter experiment at FAIR”. In: *Nuclear Instruments and Methods in Physics Research Section A: Accelerators, Spectrometers, Detectors and Associated Equipment* (2017). DOI: <https://doi.org/10.1016/j.nima.2016.05.093>. URL: <https://www.sciencedirect.com/science/article/pii/S0168900216304867>.
- [12] J. Baudot et al. “First test results Of MIMOSA-26, a fast CMOS sensor with integrated zero suppression and digitized output”. In: 2009. DOI: 10.1109/NSSMIC.2009.5402399.
- [13] M. Koziel. *Private Communication*. 2023.
- [14] M. Deveaux. “Progress on the radiation tolerance of CMOS Monolithic Active Pixel Sensors”. In: JINST 14.11 (Nov. 2019). DOI: 10.1088/1748-0221/14/11/R11001. URL: <https://dx.doi.org/10.1088/1748-0221/14/11/R11001>.
- [15] B. Arnoldi-Meadows. *MIMOSIS-1: Single Event Effects, Radiation Tolerance, Temperature Effects (Talk given on MIMOSIS-2 PRR)*. 2022.
- [16] CERN. *FEASTMP: Radiation and Magnetic Field Tolerant 10W DC/DC Converter Module (Data Sheet)*. Aug. 2016. URL: [https://espace.cern.ch/project-DCDC-new/Shared%20Documents/FEAST2Mod\\_Datasheet\\_gb2016.pdf](https://espace.cern.ch/project-DCDC-new/Shared%20Documents/FEAST2Mod_Datasheet_gb2016.pdf).
- [17] F. Morel. *Private Communication*. 2023.
- [18] J. Michel. *Private Communication*. 2023.
- [19] B. Arnoldi-Meadows. *Private Communication*. 2023.

- [20] htt. *Vendor*. URL: <https://www.httgroup.eu>.
- [21] Zestron. *Technische Informationen VIGON PE 196A*. July 2023.
- [22] T. Collaboration. *TRB*. URL: <http://trb.gsi.de/>.
- [23] S. Kwan. *FPIX Experience on TPG (Slides shown on CMS Tracker Upgrade Workshop)*. Sept. 2009. URL: [https://espace.cern.ch/CO2/Public%20Documents/Presentations%20and%20publications/Fermilab/090902\\_CML\\_SK\\_FPIXexperienceOnTPG.pdf](https://espace.cern.ch/CO2/Public%20Documents/Presentations%20and%20publications/Fermilab/090902_CML_SK_FPIXexperienceOnTPG.pdf).
- [24] H.-G. Moser. *SCT-IS-EN-0009: SCT End-cap Module Components: Spines*. July 2002. URL: [https://www.mpp.mpg.de/~sct/welcomeaux/spine/spine\\_fdr.pdf](https://www.mpp.mpg.de/~sct/welcomeaux/spine/spine_fdr.pdf).
- [25] F. Matejcek. *DXF Sketches of the MVD Carriers*. Jan. 2024. URL: [https://hessenbox-a10.rz.uni-frankfurt.de/getlink/fiKjGncRfjECR9AX9rqmbX/Carrier\\_DXF](https://hessenbox-a10.rz.uni-frankfurt.de/getlink/fiKjGncRfjECR9AX9rqmbX/Carrier_DXF).
- [26] A. Onnela. *Private Communication*. 2023.
- [27] E. Technology. *Vendor*. URL: <https://www.epotek.com/>.
- [28] T. R. A. Laboratory. *Vendor*. URL: <https://www.ukri.org/who-we-are/stfc/locations/rutherford-appleton-laboratory/>.
- [29] Epoxy Technology. *EPO-TEK 301-2<sup>®</sup> Technical Data Sheet*. Feb. 2021. URL: <https://www.epotek.com/docs/en/Datasheet/301-2.pdf>.
- [30] Kremer Pigmente. *97240 EPO-TEK 301-2 2-Komponenten-Epoxid-Klebstoff*. June 2021. URL: <https://www.kremer-pigmente.com/elements/resources/products/files/97240.pdf>.
- [31] INFN. *SDD Materials : Epoxy resin Epotek 301-1*. Aug. 2004. URL: <http://personalpages.to.infn.it/~tosello/EngMeet/ITSmAt/SDD/Epotek-301-1.html>.
- [32] H. Cease et al. *Measurement of Mechanical Properties of Three Epoxy Adhesives at Cryogenic Temperatures for CCD Construction*. Nov. 2006. URL: <https://inspirehep.net/files/c0150b0aa6d1dd4d276ca920167fc781>.
- [33] Epoxy Technology. *Tech Tip 13: Oberflächen-Vorbereitung*. URL: <https://www.epotek.com/docs/en/Related/Tech%20Tip%2013%20Surface%20Preparation.DE.pdf>.
- [34] Epoxy Technology. *Tech Tip 29: Gamma Sterilization for Medical Devices and its Effect on Epoxies*. URL: <https://www.epotek.com/docs/en/Related/Tech%20Tip%2029%20Gamma%20Sterilization%20for%20Medical%20Devices%20and%20its%20Effect%20on%20Epoxies.pdf>.
- [35] C. Chindam, A. Lakhtakia, and O. O. Awadelkarim. “Surface energy of Parylene C”. In: *Materials Letters* 153 (2015). DOI: <https://doi.org/10.1016/j.matlet.2015.04.009>. URL: <https://www.sciencedirect.com/science/article/pii/S0167577X15005546>.
- [36] E. Technology. *Private Communication*. 2023.
- [37] *Plasma Parylene Systems GmbH*. URL: <https://plasmaparylene.de/>.
- [38] R. Danhauser. *Private Communication*. 2024.
- [39] Loctite. *Technical Data Sheet Loctite Abestik 45*. June 2021. URL: [https://datasheets.tdx.henkel.com/LOCTITE-ABLESTIK-45-en\\_GL.pdf](https://datasheets.tdx.henkel.com/LOCTITE-ABLESTIK-45-en_GL.pdf).
- [40] CMC Klebetechnik. *Datenblatt CMC Typ 70097*. July 2018. URL: <https://shop.cmc.de/en/documents/file/pdf/70097.pdf>.

- [41] R. L. Workman et al. “Review of Particle Physics”. In: *PTEP* (2022). DOI: [10.1093/ptep/ptac097](https://doi.org/10.1093/ptep/ptac097).
- [42] ESA ESTEC. *Development of High Current, High Voltage and High Temperature Cable Suitable for Electric Propulsion (Presentation Slides)*. Nov. 2011.
- [43] American Durafilm. *Physical Properties of Kapton*. URL: [http://mu2e.phy.duke.edu/cw/misc/0404\\_kapton\\_properties.cfm.htm](http://mu2e.phy.duke.edu/cw/misc/0404_kapton_properties.cfm.htm).
- [44] P.Klaus et al. *CBM Progress Report: An ultra-low material budget Cu-based flexible cable for the CBM-MVD*. 2014.
- [45] ILFA. *Vendor*. URL: <https://ilfa.de>.
- [46] ILFA. *ILFA Designregeln für ein- und doppelseitige, flexible Leiterplatten*. URL: <https://ilfa.de/wp-content/uploads/2023/01/ILFA-Designregeln-Flex-DFL-1.pdf>.
- [47] J. M. Qiyang Li. *MVD: Hit Rates, Link Bandwidth and Interaction Rates*. Tech. rep. Mar. 2019. URL: [https://indico.gsi.de/event/8579/contributions/37302/attachments/27053/33844/CBM-TN-19002\\_MVD\\_Rates.pdf](https://indico.gsi.de/event/8579/contributions/37302/attachments/27053/33844/CBM-TN-19002_MVD_Rates.pdf).
- [48] LTU Enterprise. URL: [https://www.ltu.ua/company\\_en/](https://www.ltu.ua/company_en/).
- [49] CMC Klebetechnik. *Datenblatt CMC Typ 70791*. Apr. 2018. URL: <https://shop.cmc.de/en/documents/file/pdf/pdf%20englisch/70791e.pdf>.
- [50] F. Matejcek. *Technical Drawings of the Heat Sinks (Geometry c)*. [https://hessenbox-a10.rz.uni-frankfurt.de/getlink/fi4RHQZquh8aNexDuU45i7/GeoCHS1-v2\\_WHD-drawing-20231017.pdf](https://hessenbox-a10.rz.uni-frankfurt.de/getlink/fi4RHQZquh8aNexDuU45i7/GeoCHS1-v2_WHD-drawing-20231017.pdf) and [https://hessenbox-a10.rz.uni-frankfurt.de/getlink/fi9GnQBASvFLyeCs1m9mz9/GeoCHS2-v2\\_WHD-drawing-20231123.pdf](https://hessenbox-a10.rz.uni-frankfurt.de/getlink/fi9GnQBASvFLyeCs1m9mz9/GeoCHS2-v2_WHD-drawing-20231123.pdf). Nov. 2023.
- [51] testo. *Vendor*. URL: <https://www.testo.com>.
- [52] F. Matejcek. *Using Novec 649 as the coolant for the MVD*. Tech. rep. Sept. 2022. URL: <https://indico.gsi.de/event/14185/contributions/65973/attachments/40954/56689/CBM-TN-22003.pdf>.
- [53] Facturee. *Facturee*. URL: <https://www.facturee.de>.
- [54] P. Klaus et al. *MVD Keep-Out Volumes*. Tech. rep. Mar. 2019. URL: [https://indico.gsi.de/event/8579/contributions/37304/attachments/27060/33851/CBM-TN-19004\\_MVD\\_KeepOutVol.pdf](https://indico.gsi.de/event/8579/contributions/37304/attachments/27060/33851/CBM-TN-19004_MVD_KeepOutVol.pdf).
- [55] P. Klaus. “Development of the Control System for the Vacuum Operation and Validation of the MVD Prototype for the CBM Experiment”. PhD thesis. Goethe-University Frankfurt, 2021. DOI: [10.21248/gups.63325](https://doi.org/10.21248/gups.63325).
- [56] M. Deveaux. *Private Communication*. 2023.
- [57] A. Caratelli et al. *GBT-SCA: The Slow Control Adapter for the GBT System (User Manual)*. 2019. URL: [https://readthedocs.web.cern.ch/ate/files/113213790/181732620/1/161192437000/GBT-SCA-UserManual\\_v8.2.pdf](https://readthedocs.web.cern.ch/ate/files/113213790/181732620/1/161192437000/GBT-SCA-UserManual_v8.2.pdf).
- [58] P. Moreira et al. *GBT Project: GBTx Manual (V0.18, Draft)*. 2021. URL: <https://espace.cern.ch/GBT-Project/GBTX/Manuals/GBTXManual.pdf>.
- [59] 3M. *Vendor*. URL: <https://www.3m.com/>.
- [60] CERN. *3M™ Novec™ 649 Engineered Fluid*. Aug. 2016. URL: <https://multimedia.3m.com/mws/media/5698650/3m-novec-engineered-fluid-649.pdf>.
- [61] P. Gorbounov. *Project: 3M Novec 649 as a Replacement of C6F14 in Liquid Cooling Systems*. Mar. 2015. URL: [https://twiki.cern.ch/twiki/pub/LHCb/C6K/Novec\\_Memo.pdf](https://twiki.cern.ch/twiki/pub/LHCb/C6K/Novec_Memo.pdf).

- [62] 3M. *3M to Exit PFAS Manufacturing by the End of 2025*. <https://news.3m.com/2022-12-20-3M-to-Exit-PFAS-Manufacturing-by-the-End-of-2025> and <https://www.besttechnologyinc.com/wp-content/uploads/3M-Novoc-PFAS-announcement-EMSD.pdf>. Dec. 2022.
- [63] ECHA. *ECHA Publishes PFAS Restriction Proposal*. Feb. 2023. URL: <https://echa.europa.eu/de/-/echa-publishes-pfas-restriction-proposal>.
- [64] I. Elizarov. *Private Communication*. 2023.
- [65] RIVM et al. *Restriction of Per- and Polyfluoroalkyl Substances (PFAS) Under REACH: Questions and Answers*. June 2023. URL: [https://echa.europa.eu/documents/10162/2156610/230405\\_upfas\\_webinar\\_qa\\_ds\\_en.pdf/3f47fdcc-17c5-4b37-b758-720bb7e462f3?t=1687882845025](https://echa.europa.eu/documents/10162/2156610/230405_upfas_webinar_qa_ds_en.pdf/3f47fdcc-17c5-4b37-b758-720bb7e462f3?t=1687882845025).
- [66] F. Lehner. *The Liquid Cooling System of the LHCb Inner Tracker: Design constraints and Considerations*. 2002. URL: <https://s3.cern.ch/inspire-prod-files-7/7175d35b7444e84c664a23c7e2db4f9e>.
- [67] The Engineering ToolBox. *Water - Thermophysical Properties*. 2003. URL: [https://www.engineeringtoolbox.com/water-thermal-properties-d\\_162.html](https://www.engineeringtoolbox.com/water-thermal-properties-d_162.html).
- [68] VDI e. V. *Properties of Mixture Water/Glycol*. 1991. URL: <https://detector-cooling.web.cern.ch/data/Table%208-3-1.htm>.
- [69] The Engineering ToolBox. *Ethylene Glycol Heat-Transfer Fluid Properties*. 2003. URL: [https://www.engineeringtoolbox.com/ethylene-glycol-d\\_146.html](https://www.engineeringtoolbox.com/ethylene-glycol-d_146.html).
- [70] P. Guglielmini. *Technical Note: Corrosion Phenomena in Demineralized Water Cooling Circuits*. 2006. URL: [https://edms.cern.ch/ui/file/718814/1/DemiWater\\_Corrosion\\_Report.pdf](https://edms.cern.ch/ui/file/718814/1/DemiWater_Corrosion_Report.pdf).
- [71] P. Gorbounov et al. *Comparison of Liquid Coolants Suitable for Single-Phase Detector Cooling (V 1.7)*. 2016. URL: [https://twiki.cern.ch/twiki/pub/LHCb/C6K/Coolants\\_review.pdf](https://twiki.cern.ch/twiki/pub/LHCb/C6K/Coolants_review.pdf).
- [72] M. Gómez Marzoa. “Innovative Low-Mass Cooling Systems for the ALICE ITS Upgrade Detector at CERN”. PhD thesis. École Polytechnique Fédérale de Lausanne, 2016. URL: <https://cds.cern.ch/record/2231119/files/CERN-THESIS-2016-160.pdf>.
- [73] K. Agarwal. *Private Communication*. 2023.
- [74] I. Elizarov. *Cooling Supply for the STS Detector (Talk given on 42<sup>nd</sup> CBM Collaboration Meeting)*. 2023. URL: <https://indico.gsi.de/event/17147/contributions/74317/attachments/45005/63626/elizarov-cooling%20supply.pdf>.
- [75] A. Senger. *BIOMAT in CBM Cave (Talk given on 41<sup>st</sup> CBM Collaboration Meeting)*. 2023. URL: [https://indico.gsi.de/event/16428/contributions/70352/attachments/42892/59972/BIOMATatCBMcave\\_2days.pdf](https://indico.gsi.de/event/16428/contributions/70352/attachments/42892/59972/BIOMATatCBMcave_2days.pdf).
- [76] LPKF. *Vendor*. URL: <https://www.lpkf.com/>.
- [77] F. Hebermehl. “Investigation of thermal properties and alternative sensor integration concepts for the CBM-MVD”. MA thesis. Goethe-University Frankfurt, 2023.
- [78] M. Goffe. *Private Communication*. 2023.
- [79] C. J. Glassbrenner and G. A. Slack. “Thermal Conductivity of Silicon and Germanium from 3°K to the Melting Point”. In: *Phys. Rev.* 134 (May 1964). DOI: 10.1103/PhysRev.134.A1058. URL: <https://link.aps.org/doi/10.1103/PhysRev.134.A1058>.

- [80] F. Matejcek. *DXF Sketches of the  $\mu$ -Tracker Carrier*. <https://hessenbox-a10.rz.uni-frankfurt.de/getlink/fiB1kEt4MXG1iM2gJF3vCw/MuTrackerFront.dxf> and <https://hessenbox-a10.rz.uni-frankfurt.de/getlink/fiENL8iuKDZkbGcw2D6VTG/MuTrackerBack.dxf>. Jan. 2024.
- [81] J. Thompson and B. Younglove. "Thermal conductivity of silicon at low temperatures". In: *Journal of Physics and Chemistry of Solids* 20 (Feb. 1961). DOI: [https://doi.org/10.1016/0022-3697\(61\)90146-9](https://doi.org/10.1016/0022-3697(61)90146-9). URL: <https://www.sciencedirect.com/science/article/pii/0022369761901469>.
- [82] M. Minn, Y. Soetanto, and S. Sinha. "Tribological Properties of Ultra-Thin Functionalized Polyethylene Film Chemisorbed on Si with an Intermediate Benzophenone Layer". In: *Tribology Letters* 41 (Jan. 2010). DOI: [10.1007/s11249-010-9703-4](https://doi.org/10.1007/s11249-010-9703-4).
- [83] F & K DELVOTEC Bondtechnik GmbH. *Ultraschall-Dünndrahtbonder M17 (Produkt-Broschüre)*. Nov. 2017.
- [84] A. Senger. *Private Communication*. 2023.
- [85] P. Gorbounov. *Assessment of the radiation damage to the coolant in SciFi tracker (V 1.4)*. 2015. URL: [https://twiki.cern.ch/twiki/pub/LHCb/C6K/Memo\\_on\\_irradiation\\_damage\\_for\\_C6K.pdf](https://twiki.cern.ch/twiki/pub/LHCb/C6K/Memo_on_irradiation_damage_for_C6K.pdf).
- [86] C. J. Hochanadel. "Effects of Cobalt  $\gamma$ -Radiation on Water and Aqueous Solutions". In: *Journal of Physical Chemistry (U.S.)* (May 1952). DOI: [10.1021/j150497a008](https://doi.org/10.1021/j150497a008). URL: <https://www.osti.gov/biblio/4404650>.
- [87] S. A. Barker, J. S. Brimacombe, and E. M. Eades. "Action of Gamma Radiation on Liquid Ethylene Glycol". In: *Radiation Research Society* (June 1964). DOI: [10.2307/3571665](https://doi.org/10.2307/3571665). URL: <http://www.jstor.org/stable/3571665>.
- [88] G. V. Buxton and K. G. Kemsley. "Low Temperature Pulse Radiolysis of Concentrated Aqueous Solutions." In: *Journal of the Chemical Society* (Jan. 1976). DOI: [10.1039/F19767200466](https://doi.org/10.1039/F19767200466). URL: <http://dx.doi.org/10.1039/F19767200466>.
- [89] A. J. Elliot et al. "G-Values for  $\gamma$ -Irradiated Water as a Function of Temperature". In: *Canadian Journal of Chemistry* (May 1990). DOI: [10.1139/v90-111](https://doi.org/10.1139/v90-111). URL: <https://cdnsciencepub.com/doi/pdf/10.1139/v90-111>.
- [90] A. J. Elliot, M. P. Chenier, and D. C. Ouellette. "G-Values for  $\gamma$ -Irradiated Water as a Function of Temperature". In: *Canadian Journal of Chemistry* (Aug. 1990). DOI: [10.1139/v90-111](https://doi.org/10.1139/v90-111). URL: <https://doi.org/10.1139/v90-111>.
- [91] S. Ilie and M. Tavlet. "Qualification of Coolants and Cooling Pipes for Future High-Energy-Particle Detectors". In: *Nuclear Instruments and Methods in Physics Research B* (Dec. 2001). DOI: [10.1016/S0168-583X\(01\)00806-0](https://doi.org/10.1016/S0168-583X(01)00806-0). URL: <https://www.sciencedirect.com/science/article/pii/S0168583X01008060>.
- [92] G.-J. Nooren. *Requirements to the Cooling of the ITS*. 2001. URL: <https://detector-cooling.web.cern.ch/coolingsystems/CoolingSystemWeb/Documents/ALICE.pdf>.
- [93] A. K. Pikaev and L. I. Kartasheva. "Radiolysis of Aqueous Solutions of Ethylene Glycol". In: *International Journal for Radiation Physics and Chemistry* (July 1975). DOI: [10.1016/0020-7055\(75\)90079-0](https://doi.org/10.1016/0020-7055(75)90079-0). URL: <https://www.sciencedirect.com/science/article/pii/0020705575900790>.
- [94] item. *Chemische Beständigkeit von Aluminium im Kontakt mit Wichtigen Agenzien*. 2015. URL: [https://www.kleffinghaus-onlineshop.de/datasheet/DOK\\_DATA\\_Aluminium\\_SDE\\_AIN\\_V1.pdf](https://www.kleffinghaus-onlineshop.de/datasheet/DOK_DATA_Aluminium_SDE_AIN_V1.pdf).



# Erklärung

nach §30 (12) Ordnung für den Bachelor- und den Masterstudiengang Physik

Hiermit erkläre ich, dass ich die Arbeit selbstständig und ohne Benutzung anderer als der angegebenen Quellen und Hilfsmittel verfasst habe. Alle Stellen der Arbeit, die wörtlich oder sinngemäß aus Veröffentlichungen oder aus anderen fremden Texten entnommen wurden, sind von mir als solche kenntlich gemacht worden. Ferner erkläre ich, dass die Arbeit nicht - auch nicht auszugsweise - für eine andere Prüfung verwendet wurde.

Franz Alexej Matejcek, Frankfurt am Main, 15.02.2024